

(2)

**USE OF SHAPE MEMORY ALLOYS
IN THE ROBUST CONTROL
OF SMART STRUCTURES**

AD-A270 827

Final Report



Vittal S. Rao
Thomas J. O'Keefe
Leslie R. Koval

August 1993

U.S. Army Research Office
Grant No. DAAL 03-90-G-0053

University of Missouri-Rolla
Rolla, MO 65401

DTIC
ELECTED
OCT 19 1993
S E D

Approved for Public Release;
Distribution Unlimited

93 10 15 231

93-24686

REPORT DOCUMENTATION PAGE

Form Approved
OMB No. 0704-0188

Public reporting burden for this collection of information is estimated to average 1 hour per response, including the time for reviewing instructions, searching existing data sources, gathering and maintaining the data needed, and completing and reviewing the collection of information. Send comments regarding this burden estimate or any other aspect of this collection of information, including suggestions for reducing this burden, to Washington Headquarters Services, Directorate for Information Operations and Reports, 1215 Jefferson Davis Highway, Suite 1204, Arlington, VA 22202-4302, and to the Office of Management and Budget, Paperwork Reduction Project (0704-0188), Washington, DC 20503.

1. AGENCY USE ONLY (Leave blank)	2. REPORT DATE	3. REPORT TYPE AND DATES COVERED
	August 1993	Final Feb 1990-June 1993
4. TITLE AND SUBTITLE Use of Shape Memory Alloys in the Robust Control of Smart Structures		5. FUNDING NUMBERS
6. AUTHOR(S) Vittal S. Rao, Thomas J. O'Keefe and Leslie R. Koval		DAAL03-90-G-0053
7. PERFORMING ORGANIZATION NAME(S) AND ADDRESS(ES) University of Missouri-Rolla Rolla, MO 65401		8. PERFORMING ORGANIZATION REPORT NUMBER
9. SPONSORING/MONITORING AGENCY NAME(S) AND ADDRESS(ES) U. S. Army Research Office P. O. Box 12211 Research Triangle Park, NC 27709-2211		10. SPONSORING / MONITORING AGENCY REPORT NUMBER ARO 27686.11-E6-SM
11. SUPPLEMENTARY NOTES The view, opinions and/or findings contained in this report are those of the author(s) and should not be construed as an official Department of the Army position, policy, or decision, unless so designated by other documentation.		
12a. DISTRIBUTION/AVAILABILITY STATEMENT Approved for public release; distribution unlimited.		12b. DISTRIBUTION CODE
13. ABSTRACT (Maximum 200 words) <p>This report details an integrated interdisciplinary approach for designing and implementing robust controllers on smart structures. The application of shape memory alloy materials as actuators and sensors in the active control of smart structures has been investigated. A process was developed for the electrodeposition of In-T1 alloys in a composition range where this system exhibits the shape memory effect. Cu-Zn, Au-Ca, and In-Cd alloy films were produced using the electrolytic techniques and their shape memory properties evaluated. To demonstrate some of the capabilities of smart structures and to determine the limitations imposed by hardware realizations, we have designed and fabricated experimental test articles incorporating flexible structures with SMA actuators, strain gauge sensors, signal processing circuits and digital controllers. Structural identification techniques have been employed in determining mathematical models of test articles from experimental data. A modified robust control design methodology was developed to accommodate the limited control force provided by the SMA actuators. The robustness properties of closed loop structural systems were verified experimentally. Adaptive control methods were implemented. Neural network based identification and control algorithms were developed.</p>		
14. SUBJECT TERMS Smart structures, shape memory alloys, electrodeposition process, robust control, control using neural networks.		15. NUMBER OF PAGES 125
		16. PRICE CODE
17. SECURITY CLASSIFICATION OF REPORT UNCLASSIFIED	18. SECURITY CLASSIFICATION OF THIS PAGE UNCLASSIFIED	19. SECURITY CLASSIFICATION OF ABSTRACT UNCLASSIFIED
		20. LIMITATION OF ABSTRACT UL

Foreword

This report is submitted to the Army Research Office in partial fulfillment of data requirements under grant no. DAAL 03-90-G-0053. The support and technical interest of Dr. Gary L. Anderson, the technical monitor of the project, is gratefully acknowledged.

Accesion For	
NTIS	CRA&I <input checked="" type="checkbox"/>
DTIC	TAB <input type="checkbox"/>
Unannounced	<input type="checkbox"/>
Justification	
By	
Distribution /	
Availability Codes	
Dist	Avail and / or Special
A-1	

DTIC QUALITY INSPECTED &

Table of Contents

SECTION	TITLE	PAGE
1.	Introduction	1
2.	Fabrication of Shape Memory Alloys Using Electrodeposition Process	3
2.1.	Shape Memory Effect	4
2.2.	Electrochemical Synthesis of Shape Memory Alloy	6
2.2.1.	Summary	15
2.3.	Investigation of Shape Memory Properties of Electrodeposited Indium Thallium Alloys	16
2.3.1.	The Shape Memory Effect	16
2.3.2.	Pulse Plating	17
2.3.3.	Screening Design Test	18
2.3.4.	Phase Transformation and Shape Recovery	19
2.3.5.	Summary	20
2.4.	Characterization of Phase Transformation Behavior in Electrolytically Produced Indium-Thallium Shape Memory Alloy Films	21
2.4.1.	Experimental Setup	22
2.4.2.	Results and Discussion	23
2.4.3.	Summary	30
3.	Description of Test Articles and Associated Electronic Circuits	31
3.1.	Nitinol Wire Actuation	32
3.2.	Strain Gauge Sensing	35
3.3.	Controller Implementation	35
4.	Structural Modelling Techniques	37
4.1.	The Eigensystem Realization Algorithm	37
4.2.	Observer Method of Calculating the Markov Parameters of the System	38
4.3.	The MDVV Linear System Identification Algorithm	40
4.4.	Swept Sinewave Testing Method	41
4.5.	Experimental Results on the Cantilever Beam Test Article	42
4.6.	Experimental Results on the Three Mass System	44
4.7.	Determination of State Variable Representation from Transfer Function Matrix	46
4.8.	Formulation of Reduced Order State Space Model	47
4.9.	Modelling Results	48
5.	Controller Design Methodologies	51
5.1.	Classical Control Design Methods	51
5.1.1.	Actuator Dynamics	51
5.1.2.	Cantilever Beam	55
5.1.3.	Beam Transfer Function	55
5.1.4.	Three Mass System	58
5.1.5.	Comparison Between Simulation and Experiment	66
5.2.	Design of Robust Regulators with Arbitrary Eigenvalue Assignment	68

5.2.1. Implementation	69
5.2.2. Results	72
5.3. Robust Controllers	74
5.3.1. Nominal LQG/LTR Design Method	75
5.3.2. Modified LQG/LTR Method	77
5.3.3. Results	80
5.4. Adaptive Controllers	84
5.4.1. Direct vs. Indirect Adaptive Control	85
5.4.2. Model-Reference Adaptive Systems	87
5.4.3. Conventional Direct MRAC	88
 6. Identification and Control Using Neural Networks	94
6.1. Neural Network Technique to Generate the Markov Parameters	94
6.2. Identification of State Space Model of a System Using Neural Networks	97
6.3. Accelerated Adaptive Learning Algorithm	102
6.4. Comparison of the Identified Models	103
6.5. Neural Network Based Robust Controller	106
6.6. Examination of Robustness Properties	108
 Summary	110
List of Publications and Technical Reports	112
List of Participating Scientific Personnel	114
References	115

List of Figures

	Page
Figure 2.1. Macroscopic Representation of the Shape Memory Effect	5
Figure 2.2. Mechanistic Steps in Metal Deposition	6
Figure 2.3. Representation of Double Layer	7
Figure 2.4. Relationship Between Copper Content of the Deposit and Pulse Parameters	9
Figure 2.5. Scanning Electron Micrograph of In-Ti alloy Deposit	13
Figure 2.6. Relationship Between Composition and Phase Transition Temperature for In-Ti Alloys	13
Figure 2.7. X-Ray Diffraction Profiles for In-5.1 at% Cd Alloy Film	13
Figure 2.8. The Shape Recovery as a Function of Temperature for Indium Alloys	14
Figure 2.9. Illustration of Shape Memory Effect	17
Figure 2.10. Effect of Peak Current Density on Thallium Content of the Deposits Obtained at 25° C without Agitation	17
Figure 2.11. X-Ray Diffraction Profiles of In-21 at% Tl alloy deposit	19
Figure 2.12. The grain Structures of Indium Thallium Alloys	19
Figure 2.13. Polarization Curves Obtained at Room Temperature Without Agitation	24
Figure 2.14. Polarization Curves Obtained at Room Temperature Without Agitation	24
Figure 2.15. Intensity Profiles of Electrodeposited In-24at%Tl Alloy on Heating	26
Figure 2.16. Austenitic Phase Transformation of In-Tl Alloys on Heating	26
Figure 2.17. The Depth Profiles of the Composition of Electrodeposited In-24at%Tl Alloy	27
Figure 2.18. The Grain Structures of Electrodeposited In-Tl Alloys	27
Figure 2.19. Austenite Phase Transformation of Annealed In-24at%Tl Alloy on Heating	29
Figure 2.20. Relationship Between Thallium Content and Phase Transformation Temperature	29
Figure 2.21. Relationship Between c/a Ratio and Thallium Content of the In-Tl alloy	29
Figure 3.1. Top view of the cantilever beam test article	31
Figure 3.2. 3-Mass System Test Article	32
Figure 3.3. NiTiNOL wire dynamics	33
Figure 3.4. NiTiNOL wire driver circuit diagram	33
Figure 3.5. NiTiNOL Force Characteristics	34
Figure 3.6. Sensor circuit diagram	35
Figure 3.7. Block diagram representation of the test article	36
Figure 3.8. Block Diagram of Experimental Setup	36
Figure 4.1. Comparison of the calculated Markov parameters	42
Figure 4.2. Comparison of the frequency responses	44
Figure 4.3. Measured Transfer Functions (Dashed) and Fitted Curves (Solid)	45
Figure 4.4. Comparison of Frequency Response	49
Figure 4.5. Comparison of Frequency Responses	50
Figure 5.1. Typical Heating-Cooling Cycle of Nitinol Wire	52
Figure 5.2. Time Constants of 3%-Strained Nitinol Wire (10 mils)	53
Figure 5.3. Force Curve of 42" Wire	53
Figure 5.4. Experimental Setup	57
Figure 5.5. Block Diagram of Cantilever Beam with Actuator	57
Figure 5.6. Theoretical Bode Plot	57
Figure 5.7. Experimental Bode Plot	57

Figure 5.8	Open-Loop Simulation with Inactive Wires	59
Figure 5.9	Simulation of On-Off Controller	59
Figure 5.10	Simulation of P-Controller	60
Figure 5.11	Simulation of PI-Controller	60
Figure 5.12	Simulation of LQG/LTR Controller	60
Figure 5.13	Experimental Open-Loop Response	60
Figure 5.14	Experimental Response with On-Off Controller	60
Figure 5.15	Experimental Response with P-Controller	60
Figure 5.16	Experimental Response with PI-Controller	61
Figure 5.17	Experimental Response with LQG/LTR	61
Figure 5.18	Block Diagram of Three-Mass System Experimental Set-up	61
Figure 5.19	Experimental Frequency Response of 3-Mass System	61
Figure 5.20	Beam Elements with Three Strain Gages	63
Figure 5.21	Experimental Step Response of Sensor No. 1.	66
Figure 5.22	Experimental Step Response of Sensor No. 2.	66
Figure 5.23	Simulated Step Response of 3-Mass System	67
Figure 5.24	Controller Step Responses	72
Figure 5.25	Open-Loop Time Response	73
Figure 5.26	Time Response with Eigenvalue Assignment Controller	73
Figure 5.27	Open-Loop Time Response (Robustness Test)	74
Figure 5.28	Time Response with Eigenvalue Assignment Controller (Robustness Test)	74
Figure 5.29	Controller and Plant Block Diagram	75
Figure 5.30	Comparison of Loop Transfer Recovery	77
Figure 5.31	Comparison of Control Effort	77
Figure 5.32	Basic LQG/LTR System Configuration	78
Figure 5.33	Block Diagram of Modified LQG/LTR Structure	79
Figure 5.34	System Performance with the Modified Structure LQG/LTR Controller	80
Figure 5.35	Comparison of Controller Effort for Three Mass Structure	81
Figure 5.36	Initial Condition Responses for Three Mass System	82
Figure 5.37	Controller Responses with Added Noise for the Three Mass System	83
Figure 5.38	Controller Responses with Added Mass for the Three Mass Structure	84
Figure 5.39	Direct Model-Reference Adaptive Control Structure	86
Figure 5.40	Indirect Model-Reference Adaptive Control Structure	86
Figure 5.41	Self-Tuning Regulator Structure	88
Figure 5.42	Direct MRAC Regulator for Smart Structure	89
Figure 5.43	Open vs. Closed-Loop Response (Direct MRAC)	89
Figure 5.44	Evolution of Control Vector, (Direct MRAC)	90
Figure 5.45	Indirect MRAS Regulator for Smart Structure	92
Figure 5.46	Open vs. Closed-Loop Response (Indirect MRAC)	93
Figure 5.47	Evolution of Control Vector, (Indirect MRAC)	93
Figure 6.1.	Neural network architecture for determining the Markov parameters	95
Figure 6.2.	Architecture for Linear System Identification	98
Figure 6.3.	Accelerated Adaptive Learning Algorithm	103
Figure 6.4.	Comparison of performance of various learning rate algorithm	104
Figure 6.5.	Comparison of the frequency responses	106
Figure 6.6.	Neural network training scheme to copy the LQG/LTR controller	106

Figure 6.7.	General network architecture used to copy the LQG/LTR controller	107
Figure 6.8.	Closed loop performance of the controllers for nominal tip mass	108
Figure 6.9.	Closed loop performance of the controllers for increased tip mass	109
Figure 6.10.	Closed loop performance with sampling time increased from 0.02 sec to 0.1 sec	109

List of Tables

Table	Title	Page
Table 2.1.	Shape Memory Alloys	4
Table 2.2.	Phase Structures of SMAs	10
Table 2.3.	X-Ray Diffraction Data of Brass	11
Table 2.4.	X-Ray Diffraction Data for Au-Cd	12
Table 2.5.	Statistical Design Results for Pulse Plating of Indium-Thallium Alloy	18
Table 2.6.	Summary of Factor Effect Intervals at 95% Confidence Limit	18
Table 2.7.	Relationship Between Composition and Phase Structure of Deposited Alloys	25
Table 4.8.	3-Mass System Modal Frequencies	44
Table 5.1.	Effective Force of NiTiNOL Wire (54 inch)	54
Table 5.2.	Comparison of Natural Frequency (Hz)	55
Table 5.3.	Summary of 10% Settling Time	58
Table 5.4.	MSC/NASTRAN Output for Three-Mass System	62
Table 5.5.	Regulator Pole Locations	68
Table 5.6.	Desired z-Plane Locations for Closed-loop Poles	70
Table 5.7.	Regulator Feedback Matrices	70
Table 5.8.	Observer Poles	71

1. Introduction

The main objective of this project is to investigate the application of shape memory alloys in the robust control of smart structures. This objective was accomplished by developing:

- (i) new shape memory alloys using electrodeposition process,
- (ii) design and implementation of robust controllers for smart structures,
- (iii) development of adaptive control techniques, and
- (iv) experimental verification of dynamic responses of smart structures.

This final report summarizes the total effort on this project, including the development of new shape memory alloys, design, simulation studies, and implementation of robust and adaptive controller on smart structures.

Major Accomplishments

- (1) The shape memory alloy indium-thallium (In-T1) is produced by electrodeposition techniques. The effect of pulse plating parameters on the compositions of the In-T1 alloy was investigated. The relationship between composition and phase structure of the alloys deposited was investigated with regard to the shape memory effect. Not only did the deposited alloys exhibit the shape memory effect, but the composition-phase relationship was shown to deviate from that reported in alloys in an equilibrium condition. Since the stiffness of the In-T1 alloy is low and thallium is quite toxic, the indium-cadmium (In-Cd), copper-zinc (Cu-Zn) shape memory alloys were produced using the electrodeposition process.
- (2) Cu-Zn, Au-Cd, In-T1 and In-Cd alloy films were produced using electrolytic techniques and their shape memory properties were evaluated. Cyanide solutions were used for the Cu-Zn and Au-Cd deposits, but sulfate solutions were preferred for the indium alloys. The use of pulsed current was beneficial in giving dense and uniform deposits. The Cu-Zn and Au-Cd alloys did exhibit a degree of brittle behavior in the as-deposited condition. Simple bending tests were conducted and shape memory effects were confirmed on the Cu-Zn and indium alloys.

- (3) To demonstrate the capabilities of smart structures, a simple cantilever beam and a 3-mass system (test articles) were designed and fabricated by incorporating active sensors and actuators. The electronic circuits for signal processing and drivers, and data acquisition systems have been designed, fabricated and mounted on the test articles. The shape memory alloy, Nitinol, was used for actuator purposes.
- (4) The mathematical models for structural systems was developed by using finite element models and structural identification techniques. The results of structural identification were utilized in validating the finite element models. The structural identification method, Eigensystem Realization Algorithm (ERA), was adopted for determining mathematical models for test articles.
- (5) To minimize the effects of uncertainties on the closed-loop system performance of smart structures, robust controllers were designed and implemented on test articles. A modified robust control methodology was developed to accommodate the limited control force provided by shape memory actuators. The robustness properties of controllers have been verified experimentally.
- (6) We have also developed techniques for identification and control using artificial neural networks. We have developed a multi-layer neural network architecture for implementing structural identification method (ERA) and experimentally implemented on test articles. We have introduced adaptive neuron activation function and an accelerated adaptive learning rate algorithm for reducing the training time of neural networks. The robust controller was implemented on a simple cantilever beam using a neural network.
- (7) The application of adaptive control algorithm for vibration suppression of smart structures was investigated in this project. The conventional model reference adaptive control algorithms were successfully implemented on the structural test articles.
- (8) We have established excellent interdisciplinary laboratory facilities for conducting research in smart structures and neural networks.
- (9) Based on the results accomplished in this project, we have submitted a proposal to the National Science Foundation for the development of curriculum in the smart structures area. The NSF has approved this project for funding.

2. Fabrication of Shape Memory Alloys Using Electrodeposition Process

As the use of shape memory alloys (SMAs) grows, there is an increasing interest in developing new synthesis techniques for their production. Conventionally, shape memory alloys are produced by melting, casting and shaping followed by a heat treatment cycle to give the desired properties [1]. Powder metallurgy [2,3] is also a popular processing method because finer grained metals that exhibit reproducible memory characteristics can be produced. Sputtering [4] has been investigated to prepare shape memory films and although the technique is still at the developmental stage, the initial results appear quite promising. Rapid solidification techniques, including melt spinning [5,6,7], are also gaining in popularity for the manufacture of shape memory ribbons or wires.

In view of this trend, studies were undertaken to assess the use of electrolytic methods for making alloys which exhibit the shape memory effect. It is well documented that the phase-composition-temperature relationship for alloys made electrolytically can vary substantially from similar alloys made thermally [8]. Relatively stable, but non-equilibrium structures are common; a condition probably caused by the internal stress level inherent to thin film deposition processes. If a similar phenomenon occurred with electrodeposited SMA'S, then advantageous changes in properties might also result in these films and transformation behavior altered by varying the operating parameters used during processing.

Electrodeposition offers several unique features in that alloys can be deposited as thin films, *in situ*, at ambient temperature. An additional advantage is relatively low capital and operating cost, and high volume manufacture with relatively good reproducibility and control. One major limitation is that a number of important metals, such as aluminum and titanium, can not be electrodeposited from aqueous electrolytes.

The primary objective of this research was to investigate the feasibility of using electrolytic techniques for preparing shape memory alloys. The Cu-Zn, Au-Cd, In-Tl and In-Cd systems were chosen to test the concept since they can be electrodeposited from aqueous solutions. The study focused on the electrolytic production and characterization of the alloys, with emphasis on the composition and transformation temperature relationships.

2.1 Shape Memory Effect

The shape memory effect occurs if the alloy has the ability to exist in the martensitic crystal form at one temperature but will transform to the parent phase at an elevated temperature. This phenomenon is found in many alloy systems and a listing of the more common systems is given in Table 2.1 [9].

Table 2.1 Shape Memory Alloys

Alloy	Remarks (austenite/martensite)
<i>Pseudoelastic(SIM)</i>	
Cu-Zn	bcc/orthorhombic(3R)
Cu-Zn-X	bcc/orthorhombic(3R)
Cu-Zn-Sn	bcc/orthorhombic
Cu-Al-Ni	bcc/orthorhombic(2H)
Cu-Al-Mn	bcc/orthorhombic(2H)
Ag-Cd	bcc/orthorhombic(2H)
Au-Cd	bcc/orthorhombic(2H)
CuAuZn	bcc/orthorhombic(3R)
Fe ₃ Be	fcc/tetragonal
Fe ₃ Pt	fcc/tetragonal
In-Ti	fcc/tetragonal
Ni-Ti	bcc/orthorhombic
Au-Cu-Zn	bcc/2H + 18R
Cu-Sn	bcc/orthorhombic(2H)
<i>shape memory effect</i>	
In-Cd	fcc/tetragonal
Ti-Nb	fcc/bcc
304 stainless steel	bcc/hcp
Ni-Al	bcc/CuAl type
Cu-Zn(-X)	
Ag-Cd	bcc/orthorhombic
Fe-Ni	
Ni-Ti	
Cu-Al(-Ni)	
Au-Cd	
In	

The stability of the alloy phases of various compositions in shape memory systems with changes in temperature has been studied for a number of alloys, and is usually indicated by the temperature at which the martensitic transformation occurs. When an external stress is introduced into the specimen, the situation changes. In a homogeneous system, the relation between M_s and the composition is modified to account for the effect of the external factor. Thus for example, the stability of the parent phase (austenite) and the products (martensite) does not only depend on the

changes in the temperature and the composition but is strongly influenced by both the shear and the volume stresses.

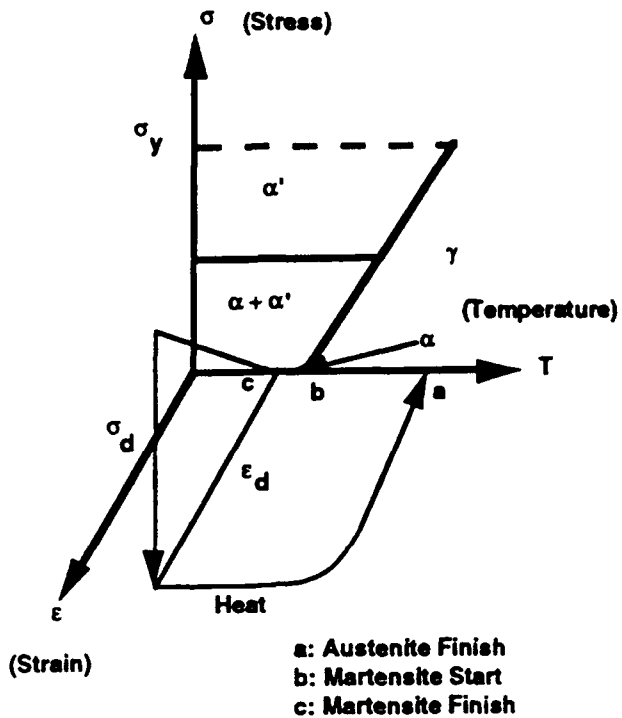


Fig. 2.1 Macroscopic representation of the shape memory effect

In Fig. 2.1, this effect is accounted for in a stress-strain-temperature field and the stability of thermal martensite (α), stress induced martensite (SIM, α'), and high temperature austenitic phase (γ). The relationship between stress and temperature can be expressed by the Clausius-Claperon type of equation applied to SIM [10].

$$\frac{d\sigma_d}{dT} = \Delta H / \epsilon T_0 V_m$$

where, σ_d is the stress for SIM formation.

ΔH is enthalpy of the SIM formation.

T_0 is the equilibrium temperature for austenite and SIM.

ϵ is the strain attained at complete martensite transformation.

V_m is the molar volume.

Fig. 2.1 also shows that the stress for α and α' formation decreases with decreasing temperature above M_s (martensite start) due to an increase in instability of the parent γ phase, becoming zero at M_s . On reaching M_s , further cooling causes more martensite to form spontaneously and continues

until M_f (martensite finish) is reached where the specimen completely transforms to martensite. If an external stress σ_d (less than the yield stress) is applied, the strain on the specimen is increased to ϵ_d , the specimen retains the same dimensions even upon removal of the stress. On heating, the reverse martensite transformation starts and the fraction of the martensite decreases until A_f (austenite finish) is reached where a fully austenitic phase is attained with the result that the specimen recovers its initial predeformed shape.

The total strain may or may not be completely recovered. If the specimen is strained too far, the irreversible deformation introduced will not be recovered at any temperature. This irreversible portion of the strain is responsible for the partial shape recovery behavior observed in many systems.

2.2 Electrochemical Synthesis of Shape Memory Alloy

Electrodeposition Process

Metal electrodeposition involves an electrochemical reaction which is the reductive discharge of ions at the electrode surface, simply illustrated by the half cell reaction $M^{+n} + ne^- \rightarrow M$. The mechanistic sequence for this reaction is usually described by identifying the regions in which the ion undergoes the changes preceding incorporation into the crystallite lattice.

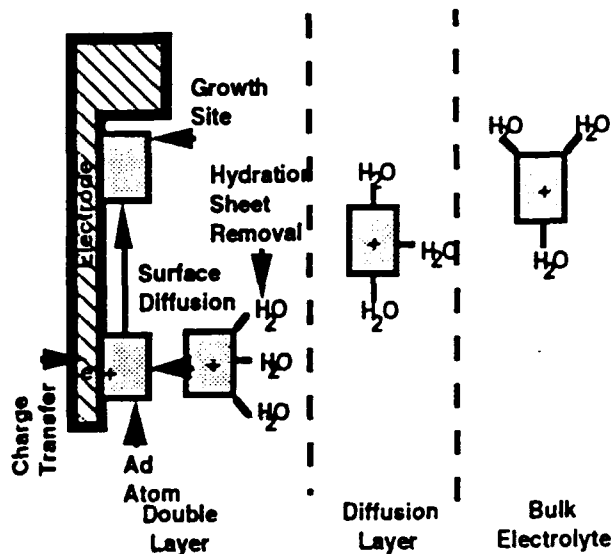


Fig. 2.2 Mechanistic steps in metal deposition

As shown in Fig. 2.2, a hydrated ion arrives at the diffusion layer from the bulk under the influence of the imposed electrical field as well as by convection. The ion passes through a stagnant region called the diffusion layer δ and the driving force is the chemical gradient. Also, the movement of electrolyte is quite limited in adjacent layers due to viscosity forces. If the process is mass transfer controlled the local concentration changes of the reacting species due to the relatively slow diffusion rate dominate in this region. The thickness of the layer can be estimated experimentally and relates to the maximum current allowed for the electrolysis called the "limiting current". The thickness of the layer reflects the interaction of the dynamic forces due to the electrolyte movement or flow in the bulk phase and the forces of viscosity damping the movement near the electrode surface. In practical systems, the diffusion layer thickness is about 0.5 mm. In systems with fast flow or intensive agitation, the value could be an order of magnitude smaller. Electrolytic deposition of metals is usually performed well below the limiting current of the deposition reaction. If metals are electrodeposited near the limiting current a nodular, impure, porous and even powdery deposit may be produced.

A multitude of similar occurrences takes place over the entire area of the electrode, thus causing a very dynamic situation of ion movement. Since electrical neutrality must be maintained, the anions and their distribution must also be considered. The current thinking is that very distinct zones exist at the electrode interface, which are a function of the high field strength, hydration effects and ion charge distribution. In simple terms the redistribution of electrical charge at the phase boundary may be represented as two parallel sheets of charge of opposite sign. The region where this is observed is called the "double layer", and a schematic representation is given in Fig. 2.3.

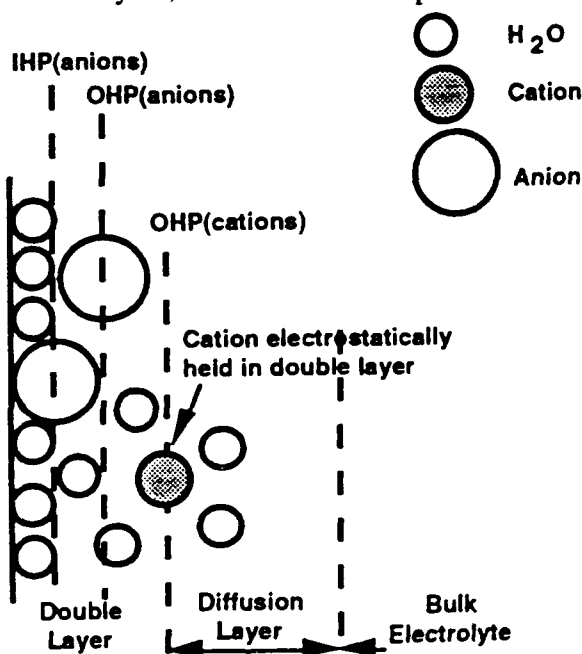


Fig. 2.3 Representation of double layer

The nature of the layers next to the electrode can have a profound effect on the electrodeposition of metals. The thickness of the layer depends on the level of agitation or stirring, other ions present in the electrolyte, temperature, and other factors. The electric field strength of the double layer is found to be on the order of 10^7 V/cm. It is this strong field acting upon molecules and ions during the electrochemical reactions which so greatly affects the reaction rates, and the probability of processes occurring at electrode interface. In sum, it is these non-equilibrium characteristics make the electrochemical reactions strong candidates to produce deposits with unique or unusual properties.

Electrolytic Synthesis of Alloy Films

Cu-Zn alloys

Brass alloy films were prepared using two electrolytic techniques, pulse electroplating and spontaneous cementation from cyanide solutions.

The composition of the electrolyte for pulse plating was 96 g/l of copper cyanide, 10 g/l of zinc cyanide, 150 g/l of sodium cyanide and 44 g/l of sodium hydroxide. Bath temperature was held at 45° C for pulse plating. In pulse plating, rotating stainless steel disc electrode was used as a cathode and brass for anode. The parameters such as power on and off time and peak current density were varied as was the metallic ionic concentration in the solution to obtain the desired alloy compositions. Previous studies [11-14] have shown that when metals and alloys are deposited using pulsed current, the mechanical properties were often better than those of conventionally plated alloys. Of more significance in this study was the phase stability of the deposits for different compositions and structures. Fig. 2.4 simply shows the wide variation of the compositions obtained by changing the operating parameters.

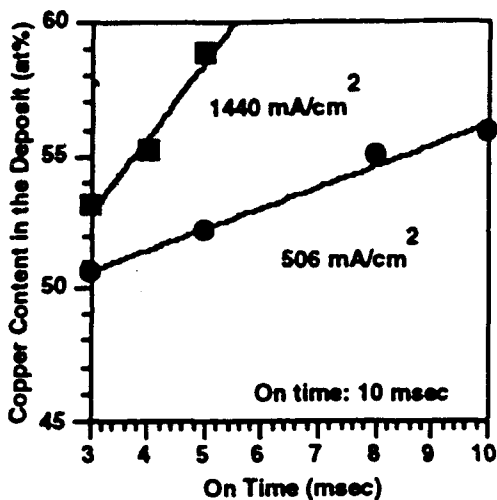
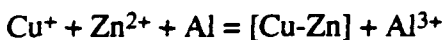


Fig. 2.4 Relationship between copper content of the deposit and pulse parameters

Cemented brass films were produced by contacting an aluminum sheet with a solution containing copper and zinc ions. The brass deposit was thought to be the result of the displacement reaction to produce a solid solution alloy [Cu-Zn]:



where [Cu-Zn] is a solid solution.

The composition of the deposits and phases formed were varied by adjusting the concentration of the electrolyte and/or by altering the temperature of the electrolyte. The film thickness produced varied from about 20 to 40 μm depending upon the plating time, concentration and temperature of the electrolyte.

Au-Cd alloys

The gold-cadmium film used in the low temperature study was obtained using standard DC plating technique. The formulation of the cyanide solution ($\text{CdO}:2.8 \text{ g/l}$, $\text{KOH}:5 \text{ g/l}$, $\text{KCN}:25 \text{ g/l}$ and $\text{KAu(CN)}_2:0.4 \text{ g/l}$) and the choice of plating conditions were based on analyses of some deposits made during screening tests in which the electrochemical parameters were varied. The electrolyte consists of KOH . Depositions were made at different temperatures using a stationary stainless steel cathode.

Indium alloys

A sulfate solution containing 40.6 g/l of indium sulfate, 2.2 g/l of thallium sulfate, and 28 ml/l of sulfuric acid were used to produce indium-thallium and 52 g/l of indium sulfate, 2 g/l of cadmium sulfate and 10 g/l of sodium sulfate was used for indium-cadmium alloy films. Platinum foil was used as an anode and the cathode substrate was a glassy carbon plate. In-Tl alloy films were electrodeposited using pulsed current generated by a Dynatronix Model DPR 20-1-3 rectifier. To obtain different compositions, various pulse parameters such as peak current density (50-100 mA/cm²), on and off time (10-54 msec) were used. The bath temperature was varied from ambient to 45° C. In-Cd alloys were produced by DC plating at various current densities. The average thickness of the deposits was about 50 μm.

Phase Transitions and Shape Recovery

Phase transformations were investigated as a function of temperature using a Scintag 2000 X-ray diffractometer with low temperature chamber or high temperature furnace attachment. Phase structures of equilibrium alloys are listed in Table 2.2 [15-18].

Table 2.2 Phase Structures of SMAs

Alloy	Phase	
	Austenite	Martensite
Cu-Zn	β (CsCl)	FCC, 9R(monoclinic) 3R(FCT)
Au-Cd	β(CsCl)	β'(Orthorhombic), β''(Trigonal)
In-Tl	FCC	FCT
In-Cd	FCC	FCT

Cu-Zn alloys

Since most of the brass deposits were brittle, characterization studies were limited to specimens that showed sufficient ductility to assure adequate bending. One example of X-ray results for electrolytic brass containing 45at%Zn is shown in Table 2.3.

Table 2.3 X-Ray Diffraction Data of Brass

d Spacing(Å)			Phase
25°C	-196°C Calc.	α,β	
2.27			Martensite
2.15	2.14	2.15	α
2.10	2.09	2.09	β
2.03			Martensite
1.86	1.85	1.86	α
1.48	1.48	1.48	β
	1.32		α
1.21	1.21	1.21	β
	1.12		α
	1.07		α
1.05	1.05	1.05	β

From the equilibrium diagram for the composition of the alloy investigated, α (FCC) and β (BCC) phases [19] would be expected. Comparing the results made at liquid nitrogen temperature, the room temperature phases shows additional lines at $d = 2.27, 2.03$ and 1.76 \AA . It was difficult to specifically identify the room temperature phases because of the small number of peaks present. However, the alloy obviously has undergone a reversible phase transformation during cooling-heating cycle.

In this work, the electrolytic brasses were found to show structural and color transitions when the specimens were cycled between the test temperatures. At room temperature, the color of the films were copper-red, but turned to a clear yellow color in the liquid nitrogen as the specimen apparently transformed from one phase to another. All the X-ray patterns made for the electrolytic alloys were accounted for using the lines corresponding to both stress induced martensite and thermally formed martensite [20,21] and these results suggested that the martensitic phases were able to be stabilized at more elevated temperatures by the deposition process.

The structural phase transition and the color changes noted for the electrolytic films are comparable to the martensite 3R to 9R martensite or a 3R to β phase transition sequence in Cu-Zn alloys observed by Wayman [19,20] and in Cu-Al-Ni [22]. The change in color and the corresponding phase change for the electrolytic alloys appeared to be consistent with these literature results, but the color changes occurred in a directly opposite direction. The β phase (yellow color) that was observed in thermally prepared alloys at room temperature was present when the electrodeposited specimens were immersed in liquid nitrogen. When warmed to room

Table 2.4 X-ray diffraction data for Au-Cd

d Spacing (Å)	Phase
25°C	-196°C
3.32	β
3.30	β"
2.66	β"
2.60	β'
2.40	β'
2.38	β"
2.354	β"
2.348	β"
2.34	β"
2.23	β"
1.94	β"
1.66	β
1.65	β"
1.45	β"
1.40	β"
1.35	β"
1.23	β"
1.18	β
1.16	β"

The Au-Cd alloy films were generally found to be too brittle to allow detailed studies involving mechanical working. However, some simple bending and heating tests were done on some of the more ductile samples to study the shape memory effect. The film consisting of 50at%Cd occasionally showed a slight shape recovery when deformed in liquid nitrogen and subsequently heated to room temperature.

Indium alloys

A surface morphology of an electrodeposited In-Tl alloy obtained by scanning electron microscope is shown in Fig. 2.5. The surface of the deposit is dense and reasonably uniform showing various crystallite sizes from few μm to 20 μm .



Fig. 2.5 Scanning electron micrograph of In-Tl alloy deposit

Indium alloys with thallium content of 18-21at% and cadmium content of 4-5at% are known to undergo FCC (face centered cubic)-FCT (face centered tetragonal) phase transformation above room temperature and show shape memory effect. Phase structures of electrodeposited indium alloys were investigated using high temperature X-ray diffraction. The relationship between phase transformation and composition of electrodeposited In-Tl alloys, given in Fig. 2.6 [23,24], shows a large deviation from equilibrium alloys of similar composition. In fact, the phase transformation temperatures of the electrodeposited alloys are higher than those of thermally made equilibrium ones. However, the result from In-Cd alloy, given in Fig. 2.7, show the opposite trend.

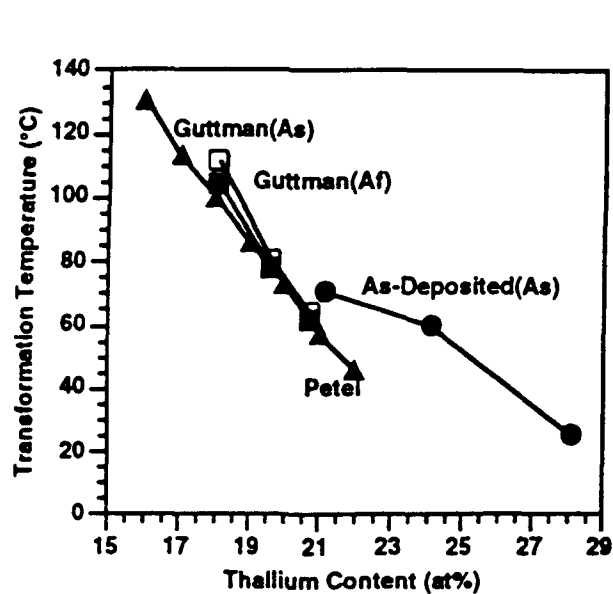


Fig. 2.6 Relationship between composition and phase transition temperature for In-Tl alloys [23,24]

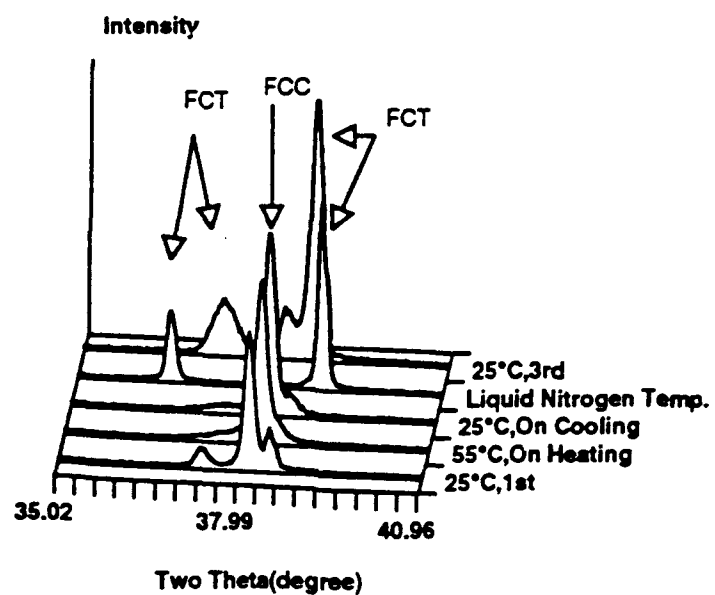


Fig. 2.7 X-ray diffraction profiles for In-5.1at% Cd alloy film

The as-deposited alloy has austenite (FCC) and martensite (FCT) mixture at room temperature. As the alloy is heated, transformation occurs and completed at 55° C. After the cooling to room temperature again, it has almost austenite. On further cooling, martensite transformation takes place and completed somewhere below zero degree in Celsius. When the deposit is warmed up to room temperature for the 3rd time, it has now austenite and martensite mixture. In fact, the transformation temperature of electrodeposited In-Cd alloy is sub-zero.

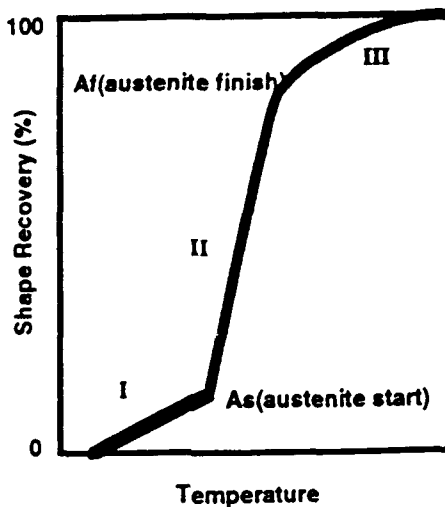


Fig. 2.8 The shape recovery as a function of temperature for indium alloys

It was reported by Nittono [25] that In-T1 and In-Cd alloys had a perfect shape memory effect. The schematic shape recovery curve of an indium alloy is shown in Fig. 2.8. The shape recovery can be divided into three stages. In early stage(I), there is a linear recovery, but small in quantity, region associated with reorientation with increasing temperature. A remarkable shape change occurs in the second stage(II) due to the phase transformation. In the final stage(III), the recovery is not appreciated showing that the shape recovery has finished. Some qualitative tests were made to see if the electrodeposited alloys exhibits the shape memory effect. An electrodeposited alloy was cut into a narrow strip and bent into a ring shape at room temperature. It was hard to distinguish the recovery regions as described above for equilibrium alloys. However, when the sheet was heated, movement toward its original shape was observed showing at least partial recovery and the shape memory effect.

2.2.1 Summary

The results show that Cu-Zn films prepared electrolytically and in the compositional range (45-52at%Zn) appear to be martensitic at room temperature. The transformation from martensite to austenite takes place when the crystal phase is distorted by cooling and this transformation is found to be thermally reversible. Au-Cd alloy showed what appeared to be reversible X-ray patterns but the shape response was apparently irreversible. The transformation temperatures of electrodeposited indium alloys show a large deviation from those of equilibrium ones, showing higher transformation temperature for In-T1 and lower for In-Cd. Alloy film prepared electrolytically also exhibit some useful shape recovery.

Possible reasons for the electrochemically synthesized shape memory alloys having unusual properties are due to small grain size of the deposit or internal stress developed during the process by adsorption of foreign species, building up of defects during electrocrystallization, or inclusion of gaseous phases evolved during electrolysis. Despite the apparent limitation on a clear picture of the phase transformation at this stage, once the roles of the factors affecting the properties of the film are elucidated, the electrolysis can be a cheap and relatively easy way to produce the shape memory alloy films with intentionally modified shape memory properties.

2.3 Investigation of Shape Memory Properties of Electrodeposited Indium-Thallium Alloys

Materials which exhibit the shape memory effect are finding increased usage as both sensors and actuators in smart or adaptive structures [26,28,30]. The essential requirement for metal alloys to be classified as shape memory alloys is a martensitic transformation upon cooling, with the appropriate phase change. Advantage is then taken of the dimensional change which accompanies the alteration in structure with temperature to perform some corrective action in a structure. Recently, studies in our laboratories have demonstrated that it is possible to produce alloys which exhibit the shape memory effect using electrodeposition techniques. This unique processing method offers a number of potentially attractive features, which in time might be incorporated into advanced responsive control systems. The alloys can be deposited in place, at ambient temperature, in thin films or layers, and in a variety of structures and compositions.

In this research, the objective was to produce alloys electrolytically which had compositions in a range where the shape memory effect was known to occur. The indium-thallium system was chosen to show the feasibility of the concept and research was focused on the product of these alloys in a composition range of 15 to 38 at% Tl. It was determined that homogeneous, dense alloy films could be electrodeposited using pulsed current from a sulfate electrolyte and the effect of pulse parameters on the composition and morphology was investigated. The phases existing in the electrodeposited alloys above room temperature were determined by high temperature X-ray diffraction techniques.

2.3.1 The Shape Memory Effect

The mechanism responsible for the shape memory effect involves the presence of a martensitic phase transformation during temperature change. The temperature at which the martensitic transformation starts on cooling is called the Ms temperature and the temperature at which the martensitic transformation stops is called Mf. For the reverse transformation, these temperatures for conversion back to the parent phase are called As and Af, respectively. The shape memory effect can be explained by the stress-strain-temperature relationship of the alloy, shown in Figure 2.9. The alloy is cooled below its Mf temperature (a to b). Then, the alloy is deformed in the martensitic state (b to c) and unloaded (c to d). There is a permanent strain present but it is not restored when the load is removed. However, when the alloy is heated, martensite is converted to the parent austenite phase and the material is restored in its original shape. In the case of the In-Tl

system, the martensite phase is a FCT (fact centered tetragonal) and the parent phase is FCC (face centered cubic).

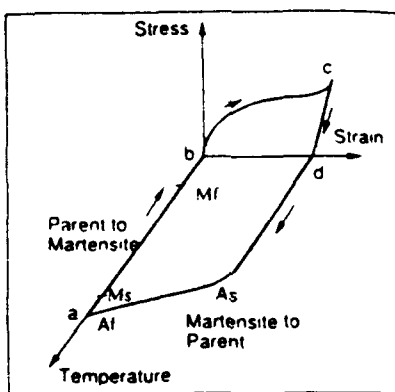


Fig. 2.9 Illustration of the shape memory effect

2.3.2 Pulse Plating

Indium-thallium alloys were electrodeposited from the electrolyte containing 40.6 g/l of indium sulfate, 2.2 g/l of thallium sulfate, and 28 ml/l of sulfuric acid with the peak current densities from 6.7 mA/cm^2 to 67 mA/cm^2 . Platinum foil was used as an anode and the cathode was a glassy carbon plate. The effect of peak current density on the composition of the alloy deposit is shown in Figure 2.10. The alloy deposits obtained at low current densities in the range of 6.7 to 10 mA/cm^2 show high thallium content of 30-40 at% and an increase in current density decreased the thallium content in the deposit.

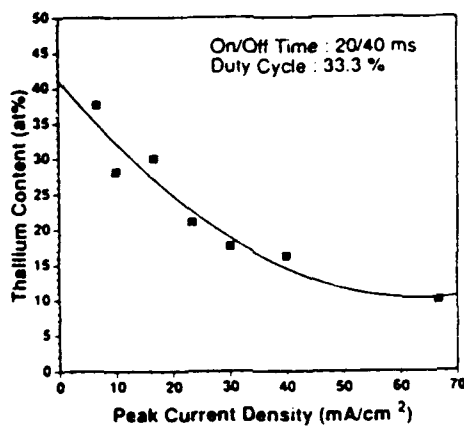


Fig. 2.10 Effect of peak current density on thallium content of the deposits obtained at 25°C without agitation

As the current density increases, the effect on composition seems to diminish. In the current density region used in this study, thallium is deposited at its limiting current value. Therefore, any increase in current density actually leads to an increase in the rate of indium deposition. At the high current density region from 50 to 70 mA/cm², the thallium content approaches the limiting value, 5.3 at%, which was the concentration of thallium in the electrolyte. The composition of the alloy does not seem to be dependent on the other pulse parameters such as duty cycle and off time.

2.3.3 Screening Design Test

A Plackett-Burman statistical design test [29] was performed to investigate the effect of selected controllable process variables on the composition of the deposit. This design is based on a simplified first order empirical model, but will also yield information indicating overall curvature, or deviation from the linear model and gives an indication of the presence of interaction effects among variables. An eight-run screening design was chosen, and the experimental procedure employed follows basically that described in the literature [32].

Pulse plating parameters used in this test were on time, off time, peak current density, and temperature. The factor levels and the calculation of factor effects are shown in Table 2.5. The screening test, as given in Table 2.6, shows that the peak current density is the only significant factor in changing the composition of the alloys, with the results indicating that an increase in peak current density causes a decrease in thallium content.

Table 2.5 Statistical design results for pulse plating of Indium-Thallium alloy.

Run Order	Response (T at%)	X1	X2	X3	X4	X5	X6	X7
1	24.27	20	20	20	25	+	+	+
2	21.63	40	40	40	45	+	-	-
3	35.25	20	40	20	45	-	+	-
4	19.29	40	40	20	25	-	-	-
5	16.41	20	20	40	45	-	-	-
6	15.25	40	20	40	25	-	+	-
7	14.44	20	40	40	25	+	-	-
8	16.20	40	40	40	45	+	-	-
Σ	162.74	72	37	85	15	62	30	89
Σ		89	37	77	56	100	44	73
Difference	-18.00	7.62	-3.38	14.16	24	9.66	19.20	13.92
Factor Effect	2.034	-4.50	1.91	9.54	4.06	-2.42	4.80	3.46

* indicates high value of factor variable levels.
- indicates low value of factor variable levels.
X1(on time), X2(off time), X3 peak current density(mA/cm²)
X4(temperature) C, and X5,X6,X7 dummy
Center point response 16.17, 16.71 and 14.91
Average 15.93 Standard Deviation(s) 0.86
Factor effect of X1 = $\frac{1}{2}(\text{response at high } X_1) - (\text{response at low } X_1)$
number of factorial runs/2

Table 2.6 Summary of factor effect intervals at 95% confidence limit

Variable	Factor Effect Interval
X ₁ (on time)	-4.50 ± 5.23*
X ₂ (off time)	1.91 ± 5.23
X ₃ (peak cd)	-9.54 ± 5.23
X ₄ (Temp.)	4.06 ± 5.23
X ₅ (dummy)	-2.42 ± 5.23
X ₆ (dummy)	4.80 ± 5.23
X ₇ (dummy)	3.46 ± 5.23

* The number '5.23' denotes factor effects which are statistically significant at 95% confidence level

Confidence interval = factor effect ± 18/VN/4

at 95% confidence limit $t = 4.303$ where t is the students t variable N is the number of design point runs(8) s is the standard deviation(0.86)

2.3.4 Phase Transformation and Shape Recovery

In-Tl alloys in a certain composition range have a FCC structure as a parent phase and undergo a martensitic transformation to a FCT structure on cooling [31]. Figure 2.11 shows the X-ray diffraction profiles of 21 at% Tl alloy deposit. The figure indicates that the electrodeposited alloy undergoes the phase transformation with change in temperature. According to the experimental results on thermally prepared equilibrium alloys [27], the transformation temperature (A_s) of a 21 at% Tl is around 60° C and the alloy transforms completely by 63-65° C. Since the electrodeposited alloy shows a mixture of FCC and FCT phases in 140° C, it seems the transformation was not complete, even when the temperature was well in excess of that expected for thermally prepared alloys. Figure 2.12 shows the grain structures of both thermally prepared alloys and electrodeposited alloys of a similar composition. The electrodeposited alloys has small grains, a few μm s in diameter and somewhat varied in grain size while the thermally prepared sample has much larger grains approximately hundreds of μm s in size. Some qualitative tests were made to see if the electrodeposited alloys exhibit the shape memory effect. An electrodeposited alloy was cut into a narrow strip and bent at room temperature. When the sheet was heated, movement toward its original flat shape was observed showing at least a partial recovery and the shape memory effect. The deformation-recovery test was repeated several times and recovery was reproduced in every instance.

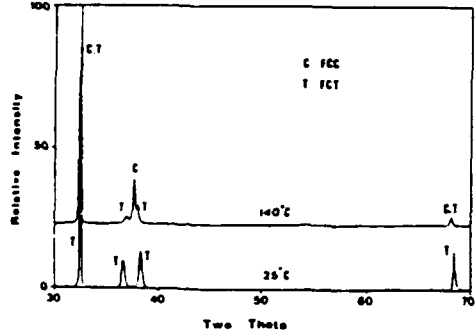


Fig. 2.11 X-ray diffraction profiles of In-21 at% Tl alloy deposit



Fig. 2.12 The grain structures of Indium-Thallium alloys
 (a) Thermal, 22 at% Tl
 (b) Electrodeposited, 21 at% Tl

2.3.5 Summary

Indium-thallium alloys can be successfully deposited from a sulfate electrolyte using pulsed current. An increase in peak current density causes a decrease in thallium content in the deposit. The results from the screening test show that the peak current density is the only significant factor which affects the composition of electrodeposited alloys. The electrodeposited alloy shows a martensite to parent phase transformation, FCT to FC upon heating. The temperature interval for the transformation of the electrodeposited alloys is much wider than those of the thermally prepared alloys but the electrodeposited alloy does not show the shape recovery. The ability to produce these new types of shape memory materials by electrolysis appears to offer some exciting possibilities for incorporation into adaptive structures. However, considerably more research is required to more clearly define and characterize these materials in order to optimize their potential applications in actual control systems. Future plans call for optimizing the properties of the In-Tl electrodeposited alloys and investigate their use as possible sensors in the active control of a simple cantilever beam.

2.4 Characterization of Phase Transformation Behavior in Electrolytically Produced Indium-Thallium Shape Memory Alloy Films

Alloys in the composition range of 15-30 at% thallium are known to have a face centered cubic(FCC) structure as a parent phase which undergo a martensitic transformation to a face centered tetragonal(FCT) structure on cooling, accompanied by a very small heat of transformation and volume difference [33]. Bowles, Barrett and Guttman [34,35] proposed the transformation occurs by a double shear process which is first on the (101) in the [101] direction followed by a second shear on (011)[011]. Since they reported the FCC/FCT transformation in In-Tl alloys, the transformation behavior of the alloy has been extensively studied [36-40]. The superelastic phenomenon associated with the stress-induced transformation and rubberlike behavior due to reorientation of martensite plates of In-Tl alloys have been reported by Burkart [41] and Miura [42]. Nagasawa [43] and Nittono [44] have shown experimentally that the alloy exhibits a shape memory effect(SME) by which an alloy, apparently plastically deformed, reverts to its original shape upon heating to high temperature.

Since Ölander [45] reported the shape memory-related phenomenon in Au-Cd alloys, many alloy systems [46-50] such as Ni-Ti and Cu-Al-Ni, showing the shape memory effect(SME), were developed and characterized [51-54]. Recently, attention has been toward developing commercial applications for shape memory alloys(SMA) such as tube fitting, electrical connectors, sensors and actuators in macro and micro scale systems and for smart structures. [55-60]. The result is that many new fabrication methods such as sputtering and rapid solidification are being attempted in addition to the conventional melting processes in an attempts to enhance the properties and Performance of the SMA's [61-64].

The electrodeposition technique offers a number of attractive features, in that alloys can be directly deposited, *in situ*, at ambient temperature and in the form of thin films. The phase structures and composition of alloys produced by electrodeposition are often substantially different from the alloys produced by a conventional melting processes. The non-equilibrium condition is often quite stable and provides some interesting property differences from those normally encountered with alloys of similar composition in an equilibrium state. In other words, the characteristics and behavior of electrodeposited shape memory alloys might be expected to deviate substantially from those of thermally prepared equilibrium alloys. Previous research showed that homogeneous, dense In-n alloy films could be electrodeposited using pulsed current from a sulfate electrolyte and the alloys showed the shape memory effects [65]. The study also focused on the relationship between phase structures and composition of electrodeposited alloys and the transformation behavior with

temperature. The phases of the electrodeposited alloys above room temperature were determined by high temperature X-ray diffraction techniques, and compared with those of thermally prepared alloys of similar compositions.

2.4.1 Experimental Studies

Production of In-Tl Alloys

Thermal methods were used to make conventional alloys to compare with those made electrolytically. Preweighed granules of indium(99.999%) and thallium(99.99%) were melted together under an argon atmosphere using a high frequency induction furnace. To ensure uniformity, the alloy was stirred vigorously prior to rapid quenching in a graphite mold. Resultant ingots, for which no appreciable change in weight was detected after alloying, were cold rolled and homogenized at 120° C for 48 hours in a tube furnace under an argon atmosphere. Two alloys, In - 22 and 27 at% Tl were prepared in this manner for further study.

The electrolyte was prepared by dissolving 40.59 g/l of indium sulfate and 2.22 g/l of thallium sulfate in a sulfuric acid solution containing 28 ml/l of sulfuric acid. Platinum foil was used as an anode and the cathode substrate was a glassy carbon plate. For the polarization measurements, a saturated calomel electrode was used as a reference.

In-Tl alloy films were electrodeposited using pulsed current generated by a Dynatronix Model DPR 20-1-3 rectifier. To obtain different compositions, various pulse parameters were used such as peak current density, pulse frequency- and duty cycle were changed. The bath temperature was varied from ambient to 45° C and no agitation was applied. The average thickness of the deposits was about 50 µm. Alloy deposits with thallium contents of 15, 20, 21, 24, 28, and 37.6 at% were used for this research. Some of the electrodeposits were also annealed at 140° C for 72 hours in a tube furnace under an argon atmosphere to determine if any phase changes occurred on heating.

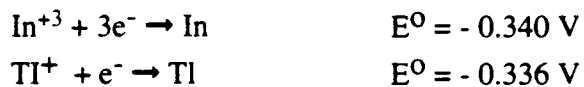
Characterization of In-Tl Alloys

The surface morphology of the electrodeposits was studied using scanning electron microscopy. Chemical compositions of all the samples used in this study were obtained from energy dispersive X-ray spectrometer measurements. Auger electron spectroscopy was employed to check the uniformity and composition of the electrodeposits.

X-ray diffraction profiles of both thermally prepared and electrodeposited alloys were generated at room temperature and 140° C. The X-ray diffractometer used in this study was a Scintag XDS-2000 equipped with a high temperature furnace. The target metal was copper and the data were obtained in the 2θ range of 30° to 70°. To find the phase transition temperature, the furnace temperature was raised in 5-10° C increments and held for about 5 minutes at each temperature prior to generating X-ray data. To prepare the alloys for metallography, the deposits were electropolished at room temperature using a solution containing 75 ml carbitol, 5ml concentrated nitric acid and 2ml concentrated hydrochloric acid and a voltage in the range of 30 to 50V [34]. The surface then was studied using a Jeol JCM-35CF scanning electron microscope.

2.4.2 Results and Discussion

Polarization behavior In a simple acidic electrolyte, thallium and indium are reported to have about the same standard electrode potentials [66].



Due to their similar electrode potentials, codeposition of In-Tl from electrolytes containing simple ions should be possible. Fig. 2.13 and Fig. 2.14 show the forward scans of cyclic voltammograms for sulfate electrolyte systems obtained at room temperature. The curves indicate both metals deposit with a significant cathodic overpotential on a carbon electrode, and the degree of polarization is higher with indium. As a result, thallium metal(Fig. 2.13 (c)) deposits preferentially and reaches a limiting plateau of 0.8 mA/cm² before indium deposition occurs for the concentrations used. When the thallium current is in the limiting region, there was a small amount of hydrogen gas evolved on the cathode. After the potential exceeds - 1.30 V, hydrogen starts to evolve extensively and the thallium current starts to increase. In the case of indium alone, as shown in Fig. 2.13 (b), indium metal begins to be deposited when the curve for thallium is already in the limiting region. As soon as the indium deposits, hydrogen also evolves on the cathode. The polarization curve for indium alone actually represents the curve for indium and hydrogen.

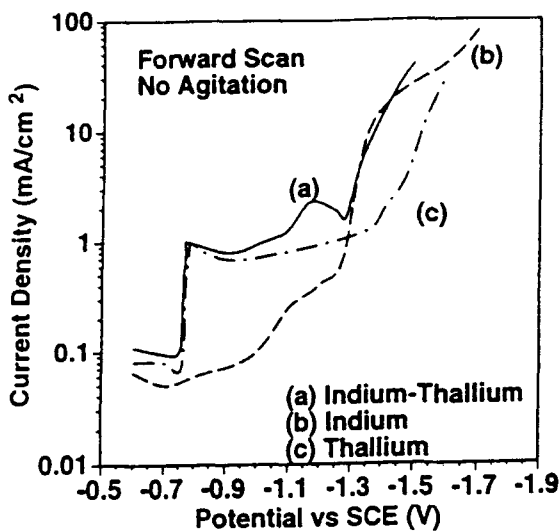


Fig. 2.13

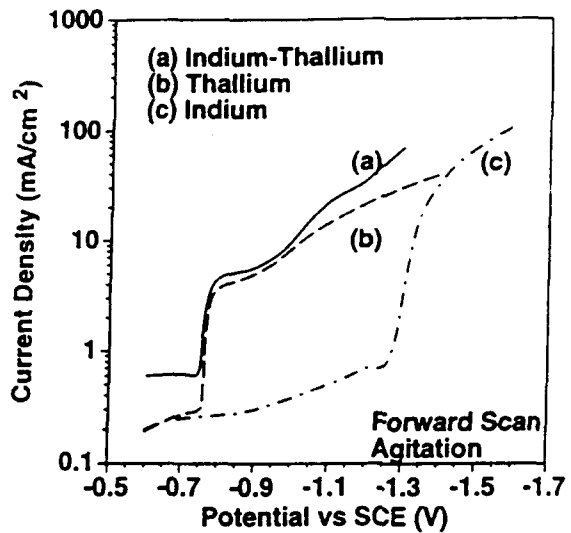


Fig. 2.14

The polarization curve for an alloy is not necessarily the summation of the individual curves for each metal [67]. In this case, however, it seems that the alloy curve does approximately represent the sum of the polarization curves for the two metals. The polarization curves using an agitated electrolyte are shown in Fig. 2.14. It is clear that the deposition of thallium is under diffusion control at potentials above - 0.8 V vs SCE since the limiting current density plateau shows an increase when the electrolyte is agitated. The relationship between the potential and current density of the indium-thallium system shows that the process is largely controlled by diffusion of thallium making it more sensitive to electrolyte agitation than indium. When the system was mechanically agitated in some preliminary experiments, the thallium content in the deposit was dramatically increased. In fact, the deposit became thallium rich and was very dendritic, and subsequent alloy deposits were made without agitation.

When standard DC was used, it was also difficult to get a uniform and smooth alloy deposit. The deposits were dendritic probably because the thallium was being deposited at its limiting current. In this study, therefore, pulsed current was chosen to electrodeposit the In-Tl alloys. In order to find the optimum plating condition to produce a fine deposit, preliminary experiments and screening design tests were performed as described previously [65]. As a result, uniform, dense alloy deposits with the desired thallium content could be produced using a peak current density of 10 to 40 mA/cm² with 10 msec as the on time and duty cycle of about 30% at room temperature.

Structure of as-deposited alloys

In-Tl alloys in a certain composition range have a face centered cubic(FCC) structure as a parent phase and undergo a martensitic transformation to a face centered tetragonal structure(FCT) on cooling [36-37]. In this study, phase structures of electrodeposited alloys having a composition of 15, 20, 21, 24, 28, and 38 at%Tl were investigated using high temperature X-ray diffraction. The results are shown in Table 1. According to the equilibrium phase diagram [68] and the experimental results on thermal alloys [39-40], a 28%Tl alloy has only the FCC structure from ambient temperature to the melting point. However, the electrodeposited 28%Tl alloy shows a mixture of FCC and FCT phases at room temperature. It seems the martensite-austenite transformation was not complete for the 21, 24, and 28%Tl alloys even when the temperature was taken as high as 1400C, since some FCT phase was detected by X-rays. The 20%Tl does not undergo a phase transformation at all, remaining FCT throughout.

Alloys having thallium contents of 22 and 27 at% were thermally prepared to compare the results of X-ray data with electrodeposited alloys of similar compositions. The results are also shown in Table 2.7. The thermal alloy of 22 at%Tl shows FCT at room temperature and completely transforms to the FCC phase by 55° C. The 27%Tl alloy was also FCC at all temperatures studied. This behavior is in good agreement with the equilibrium phase diagram and other reports in the literature.

Table 2.7. Relationship Between Composition and Phase Structure of Deposited Alloys

TI Content (at%)	Phase Structure	
	25° C(Equil.)	140° C(Equil.)
15.0	all FCT(all FCT)	all FCT(all FCT)
20.0	all FCT(all FCT)	all FCT(all FCC)
21.0	all FCT(all FCT)	63% FCC(all FCC)
22.0(T)	(all FCT)	(all FCC at 55° C)
24.0	all FCT(all FCC)	60% FCC(all FCC)
27.0(T)	(all FCC)	(all FCC)
28.0	24% FCC(all FCC)	94% FCC(all FCC)
38.0	all FCC(all FCC)	all FCC(all FCC)

(T): stands for thermally prepared.

Equilibrium structures are indicated in parentheses.

The relationship between phase and composition of electrodeposited In-Tl alloys shows a large deviation from equilibrium alloys of similar composition. The typical example of X-ray diffraction profiles of electrodeposited alloy obtained at ambient temperature and 140° C are shown in Fig. 2.15. The sample was cooled to ambient temperature after the x-ray work at 140° C and the procedure was repeated. The FCT to FCC+FCT phase transformation with temperature increase was nearly identical to the original test, indicating that the change was reversible. Thus, even though the film was transformed into the high temperature FCC structure, it reverted to its original non-equilibrium condition upon cooling.

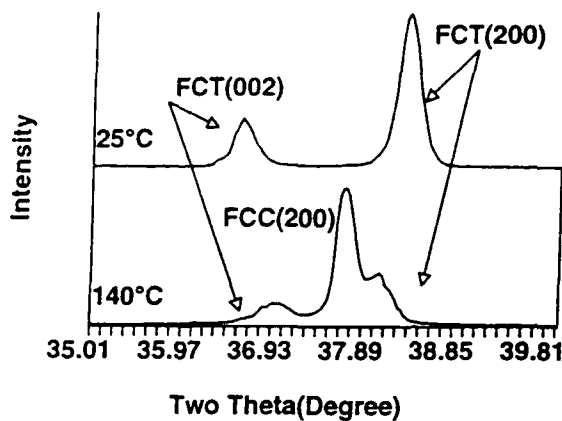


Fig. 2.15

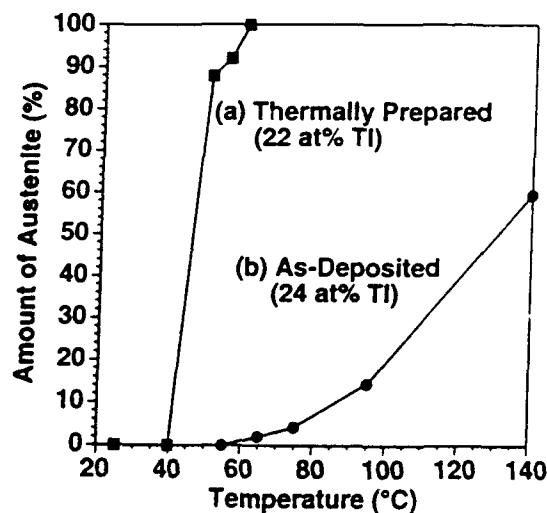


Fig. 2.16

Usually, a temperature interval for a complete phase transformation of an In-Tl alloy is less than 10° C [40]. Fig. 2.16(a) shows the phase transformation of a thermally prepared 22%Tl alloy in which the transformation starts at around 50° C and is nearly complete at 55° C. Fig. 2.16(b) shows the change in structure of a electrodeposited 24%Tl alloy deposit upon heating. The amount of austenite in the deposit was calculated from the intensities of X-ray diffraction data such as Fig. 2.15. The alloy is FCT at room temperature and some FCC begins to appear at about 60° C. Even at 140° C, there are some martensite phase remaining in the alloy. It seems that the transformation is not complete even over this wide temperature interval. The same transformation behavior was shown in a 21 %Tl alloy.

The results for the thermal alloy eliminate the possibility that the sluggishness in transformation exhibited by the electrodeposited alloys might be due to the phase stability [41] caused by the experimental procedure or the method of obtaining the data. The X-ray data were obtained at several temperatures and the sample had to be held for several minutes at each

temperature during the determination. Another possible reason for the slowness in the transformation kinetics would be non-uniformity in the composition of the deposit, because the transformation temperature is quite sensitive to the composition. Therefore, if the alloy has a non-uniform composition, the transformation of low TI content alloys starts when the transformation of high 71 content alloys is already complete. Fig. 2.17 shows the compositional variation obtained by AES throughout the deposit. The composition of the electrodeposited alloy is fairly uniform thus indicating that compositional variations are not the reason for the observed effects. The transformation temperature (As; austenite start) of a 24 %TI alloy is supposed to be around 0°C, however, the As temperature of the electrodeposited alloy deposit shown in Fig. 2.16 is about 60°C, which is much higher than for thermal alloys of the same composition. There have been many reports on the decrease in Ms (martensite start) temperature due to grain refinement [69-71]. Thus, this increase in As temperature may result from the fine grain structure of the electrodeposited alloy. Fine grained materials with more grain boundary barriers per unit volume tend to inhibit the transformation [69], therefore, an increase in temperature is needed to initiate the transformation. The micrographs of the alloy deposit shown in Fig. 2.18 indicate a fine grain structure with sizes ranging from several μm to several tens of μm . The composition across the grains was fairly uniform, as determined by EDS analysis, so grain boundary segregation does not, appear to be a problem.

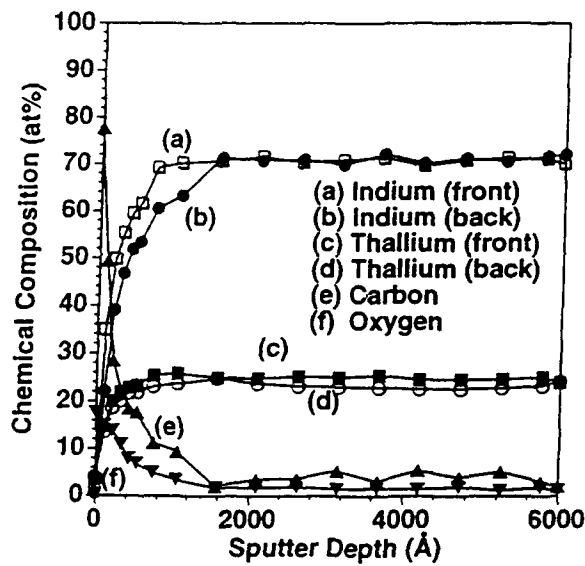


Fig. 2.17

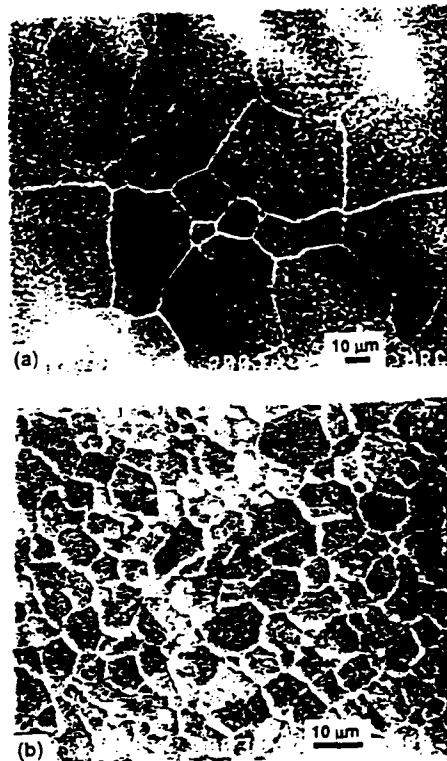


Fig. 2.18

Effect of Heat Treatment

After X-ray analysis in the as-deposited condition, selected samples of electrodeposited alloys were annealed in a tube furnace at 140° C for 72 hours. The effect of annealing on the phase transformation temperature is given in Table 2.8.

Table 2.8. Relationship Between Composition and Phase Structure of Annealed Alloys

Ti Content (at%)	Phase Structure	
	25° C(Equil.)	140° C(Equil.)
15.0	all FCT(all FCT)	all FCT(all FCT)
20.0	all FCT(all FCT)	all FCT(all FCC)
21.0	all FCT(all FCT)	20% FCC(all FCC)
24.0	all FCT(all FCC)	53% FCC(all FCC)
28.0	all FCC(all FCC)	all FCC(all FCC)
38.0	all FCC(all FCC)	all FCC(all FCC)

Equilibrium structures are indicated in parentheses.

In essence, annealing did not dramatically affect the transformation behavior of the electrodeposited alloys. One change occurring after heat treatment is that the percentages of the FCC phase for the 21% and 24%Ti alloys at high temperature are even lower than the as-deposited alloys. This result is not normally expected because if any change occurs the heat treatment would be expected to shift the alloys toward the FCC equilibrium condition. The transformation kinetics remain sluggish after heat treatment as indicated in Fig. 2.19. The data show that the heat treatment cycle used in this study is not enough to shift the electrodeposited alloys from a non-equilibrium to an equilibrium state. Possibly a slightly higher temperature and longer time or some cold working prior to heat treatment may be necessary.

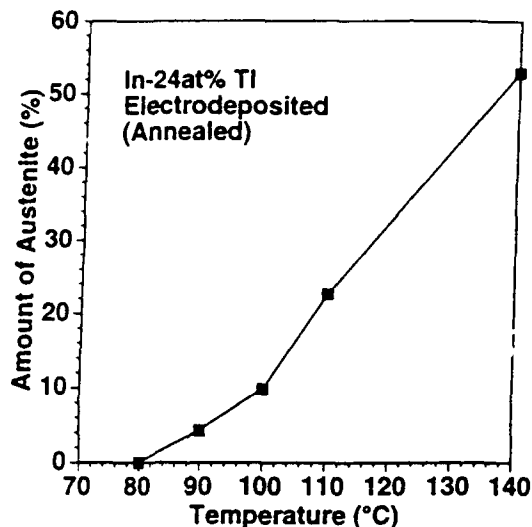


Fig. 2.19

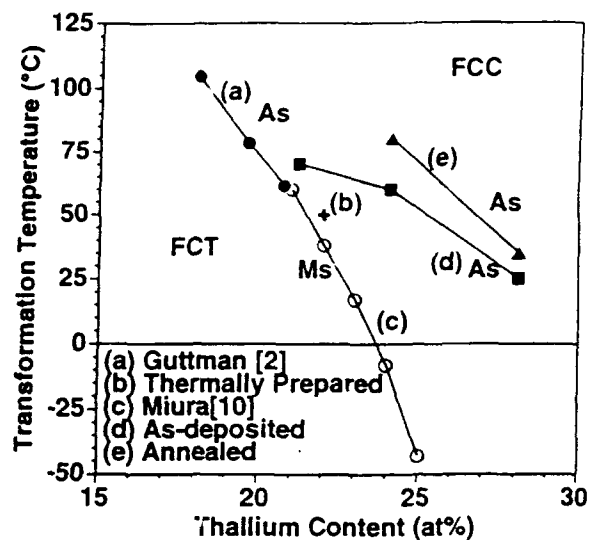


Fig. 2.20

Fig. 2.20 shows the difference in transformation temperature between thermal alloys [34,42] and electrodeposited alloys with the transformation temperature being higher for alloys produced by electrodeposition. The relationship between the thallium content and the c/a ratios of FCT phases is given in Fig. 2.21. The c/a ratio of electrodeposited alloys at 25° C is a bit higher than those of thermally prepared alloys and the ratio decreases as the temperature increases, indicating the alloy is transforming from tetragonal to cubic. This higher degree of tetragonality in the electrodeposited alloys might partially explain the higher transformation temperature. Also there is no major difference in c/a ratio between as-deposited alloys and annealed alloys.

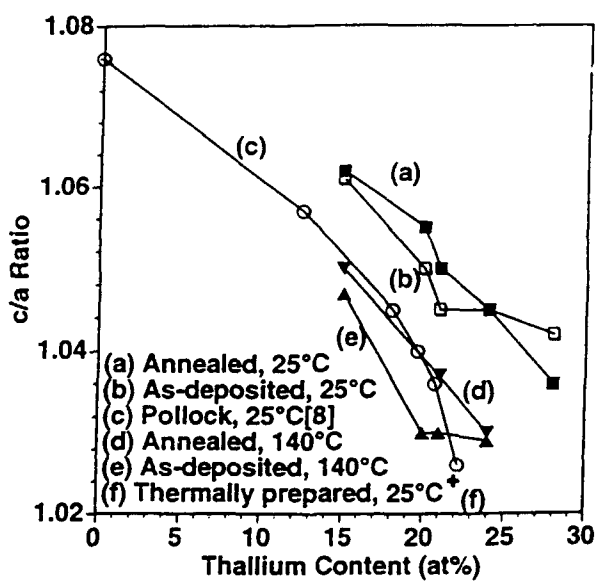


Fig. 2.21

Also, the internal stress level of the electrodeposited alloys may be relatively high due to the nature of the electrocrystallization process, absorption of impurities or organic matter, solubility of hydrogen or similar defects generated during electrolysis. Such stress levels could be responsible for the transformation behavior of the electrodeposited alloys and deviation from equilibrium noted in the results.

Shape Recovery in Electrodeposited In-Tl Alloys

Some qualitative tests were made to see if the electrodeposited alloys exhibits the shape memory effect. An electrodeposited alloy was cut into a narrow strip and bent into a ring shape at room temperature. When the sheet was heated, movement toward its original shape was observed showing at least a partial recovery and the shape memory effect. The shape recovery was confirmed for the 21, 24, and 28%Tl alloys. The deformation-recovery test was repeated several times and recovery was reproduced in every instance. Additional, more quantitative evaluations will be necessary to more completely characterize the electrodeposited alloys.

2.4.3 Summary

The shape memory alloys deposited electrolytically exhibit a substantially different composition-phase relationship than indicated by alloys in an equilibrium condition. The electrodeposited alloys having thallium contents between 21-28 at% show a martensite to parent phase transformation, FCT to FCC upon heating. The transformation temperatures of the electrodeposited alloys are much higher than those of the thermally prepared alloys. The temperature interval for the transformation of the electrodeposited alloys is much greater than those of the thermally prepared alloys. The electrodeposited alloys having FCT phases at 25° C show higher c/a ratios compared with the thermally prepared alloys. The deformed 21-28 at%Tl electrodeposited alloys at 25° C show a recovery to their original shape upon heating, a response indicating that it is possible to produce shape memory alloys by electrolysis.

3. Description of Test Articles and Associated Electronic Circuits

To demonstrate some of the capabilities of smart structures and to determine the limitations imposed by hardware realization, we have designed and fabricated experimental test articles incorporating flexible structures with shape memory actuators, strain gauge sensors, signal processing circuits and digital controllers. Two flexible mechanical systems were designed and fabricated in our laboratory. The first was an aluminum cantilever beam for which the free-vibration damping of the fundamental mode was enhanced. This system is a single-input, single-output system with one actuator and sensor. The second system studied was a three-mass system with its three natural frequencies below 3.2 hz. This system constitutes a multi-input, multi-output system with two actuators and two sensors. The electronic circuits for signal processing, SMA drivers and data acquisition systems have been designed and fabricated and mounted on the test articles. A brief description of the test articles and associated electronic circuits is presented in this section.

The single-input single-output test article used was a cantilever beam made of aluminium with shape memory actuators and strain gauge sensors. The sensing system consisted of four strain gauges placed at the fixed end of the cantilever beam and connected in a full bridge configuration. Actuation of the structure is accomplished with a set of NiTiNOL wires with driver circuits to provide heating. A tip mass was added to the beam to lower the frequency of the first natural mode to within the bandwidth of the shape memory actuators. The top view of the test article is below:

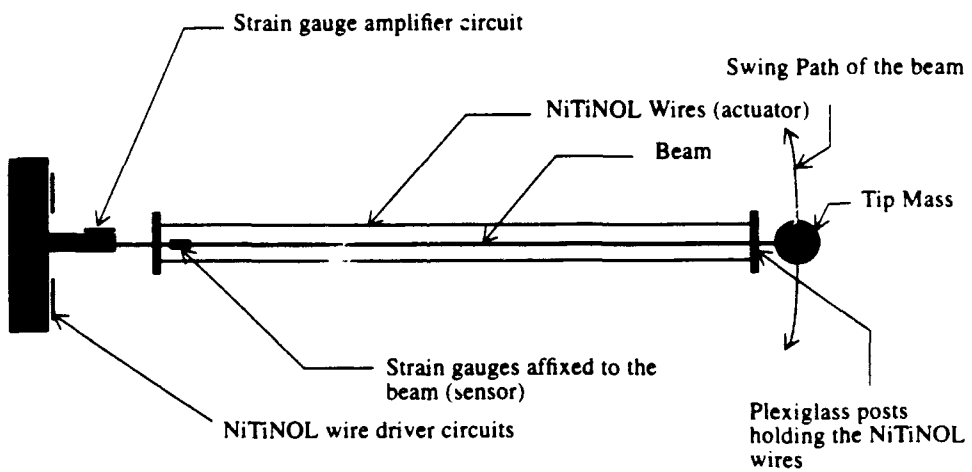


Figure 3.1. Top view of the cantilever beam test article

Another flexible structure was designed for use as a multi-input/multi-output system. It consists of three steel masses suspended vertically by thin aluminum struts. The masses were chosen such that the structure would have multiple natural frequencies within the limited bandwidth of the NiTiNOL wire actuators. This test article is depicted in Fig. 3.2.

Two sets of full bridge strain gauges are bonded to the struts at the locations indicated in Fig. 3.2. The signal conditioning electronics for each bridge are mounted on the closest mass and as close to the bridge as possible to minimize measurement noise. Actuation of the structure is accomplished with two sets of NiTiNOL wires with drivers to provide heating. One set of wires, arranged vertically along each strut, applies a moment at the bottom of the structure. A second set of wires, connected diagonally from the top of one strut to a point on the opposite strut just above the top mass, exerts a force on the structure.

The test structure can be excited with a wide range of initial conditions. Large amplitude initial conditions can permanently deform the NiTiNOL wire. This is seen as a loss of pretension of the actuator after the controller has suppressed vibrations in the beam and it is once again at rest. This deformation of the SMA actuators results in system parameter variations. The experimental data presented in this paper is the response with the beam excited in the first mode and the bottom mass displaced by one inch. This moderate amplitude initial condition was chosen to limit the permanent deformation of the force SMA actuators.

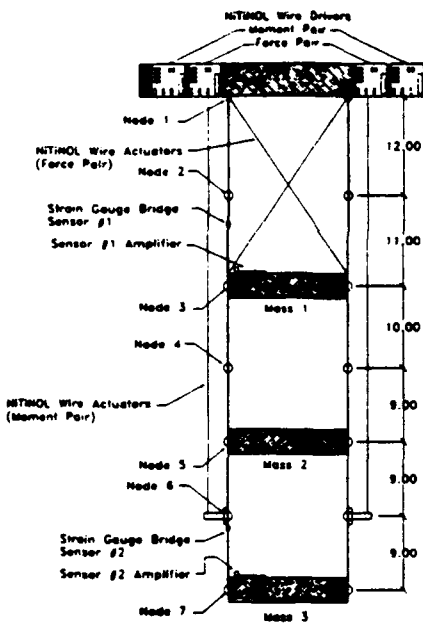


Figure 3.2. 3-Mass System Test Article

3.1. NitiNOL wire Actuation

Each shape memory alloy actuator was a pair of uncoated, trained, 9 mil NiTiNOL wires with a transition temperature of 35°C. The control force was generated by heating the wire with a current which causes the wire to contract due to the shape memory effect. To maximize the usable bandwidth of the actuator, forced air cooling was used on the cantilever beam experiment to reduce the cooling time constant of the wire. The dynamics of the actuator were experimentally determined to be described by a first order low pass

system with an effective time constant of 2.6 sec. The static input-output characteristic of the wire is shown in Fig. 3.3. The NiTiNOL wire drivers were voltage-controlled current amplifiers as shown in Fig. 3.4 designed to drive the wires in their linear range as shown in Fig. 3.4. One driver was used for each NiTiNOL wire.

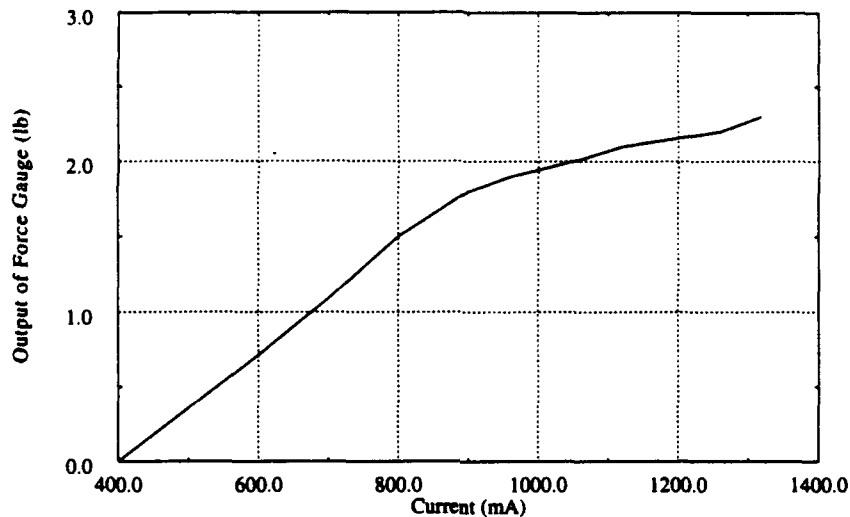


Figure 3.3. NiTiNOL wire dynamics

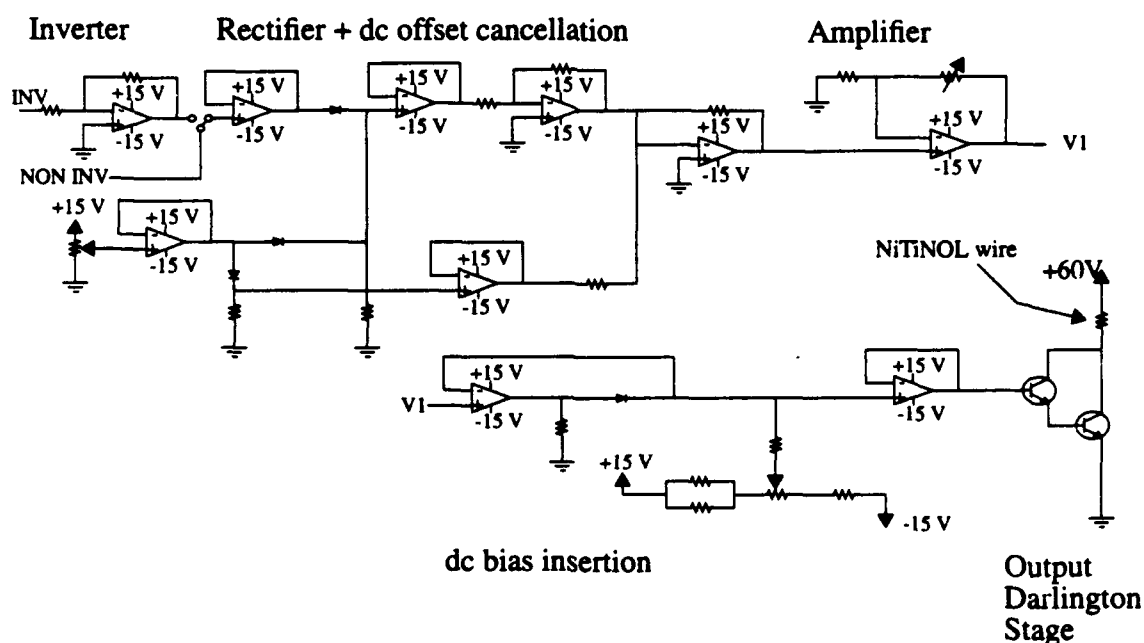


Figure 3.4. NiTiNOL wire driver circuit diagram

The first part of the driver rectifies the incoming sinusoidal voltage. The 0.7 volt d.c offset generated by the rectifying diode is cancelled by the next stage. This half wave rectified signal with zero d.c. offset is amplified to a certain voltage before it is used to drive the darlington pair which in turn passes a current through the NiTiNOL wire.

The NiTiNOL wire used is uncoated, pre-trained, nine mil wire with a transition temperature of 35°C. Each wire is clamped to the structure with an initial tension of 0.5 lbs. The tension in each wire is measured with a load cell mounted in line with the wire. The wires are driven such that the current supplied for one wire is 180° out of phase with the current of the other driver in the pair. Each driver circuit has adjustments for gain, bias and dead-band. A small dead band is allowed in the driver circuit so that current is never applied simultaneously to both wires.

A second component of the dead band is the SMA actuator itself. Since the actuation force is a function of the temperature of the SMA wire, small amounts of current flow thought the wire with no resulting force.

The relation between the DC voltage applied to the driver and the resulting force in one of the moment actuators is shown in Fig. 3.5. From Fig. 3.5, it can be seen that the deadband of the SMA actuator for the DC input is approximately 1.6 volts. The actual deadband during operation of the system will vary from the DC value due to the heating and cooling of the NiTiNOL actuator. The dead-band has the benefit of increasing the noise immunity of the actuator.

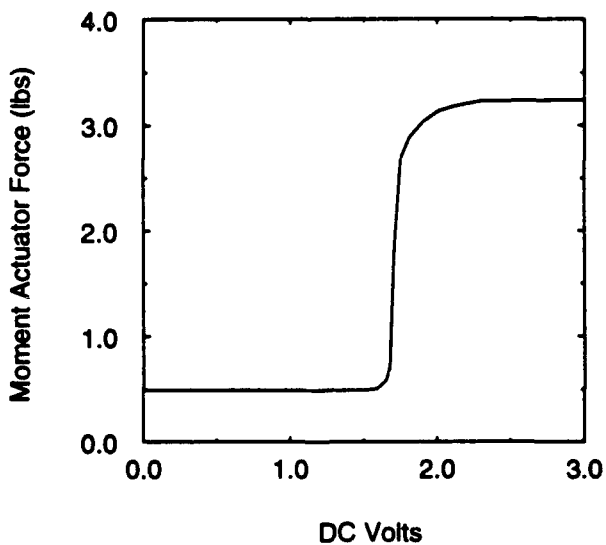


Figure 3.5. NiTiNOL Force Characteristics

3.2. Strain Gauge Sensing

The strain gauge bridge was powered by a regulated 10V supply and the output was amplified by an instrumentation amplifier with a gain of approximately 110. Assuming the strain in the beam at the fixed end is proportional to the tip displacement, the sensor voltage is proportional to the tip displacement.

The bridge configuration of the four strain gauges and the difference amplifier circuit is as shown in the following circuit.

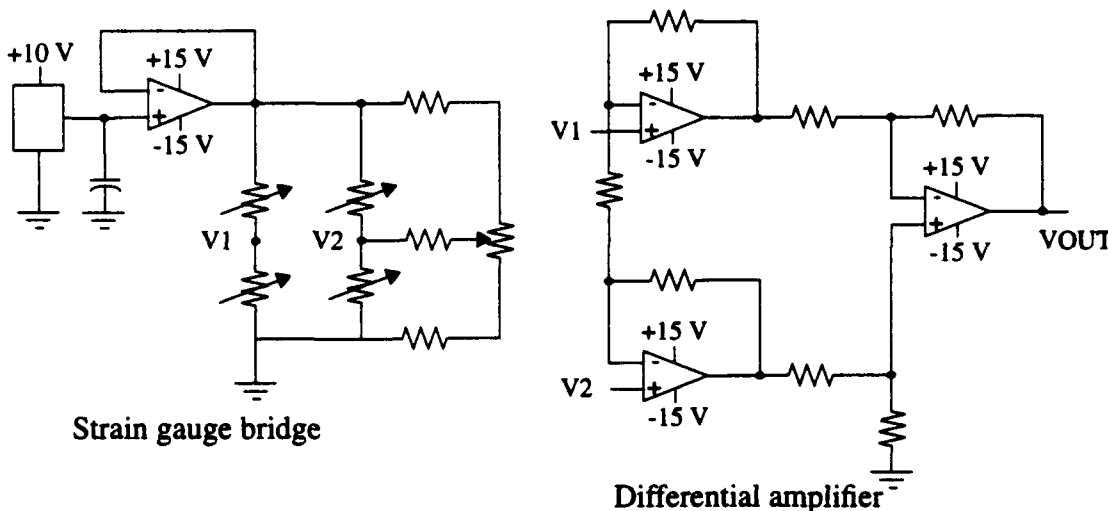


Figure 3.6. Sensor circuit diagram

The differential voltage out of the strain gauge bridge appears at points V1 and V2. This voltage is amplified by the differential instrumentation amplifier to generate a single ended voltage that is proportional to the (V1-V2).

3.3. Controller Implementation

For purposes of implementing the digital controllers, the strain gauge electronic circuits and the driver circuits are interfaced to a personal computer. For the cantilever beam test article, a Keithley-Metabyte DAS-20 interface board was used for the A/D and D/A conversions. For the 3-mass system, a Keithley-Metabyte DAS-20 A/D board with a SSH-4 simultaneous sample and hold interface was used for the A/D conversions. This allows the strain gauge data collection for control as well as the collection of other data of interest such as wire load cell information. The driver circuits on the 3-mass system are interfaced to the personal computer through a Keithley-Metabyte DDA-06 simultaneous sample and hold board.

The control block diagram representation of the test articles is as shown below.

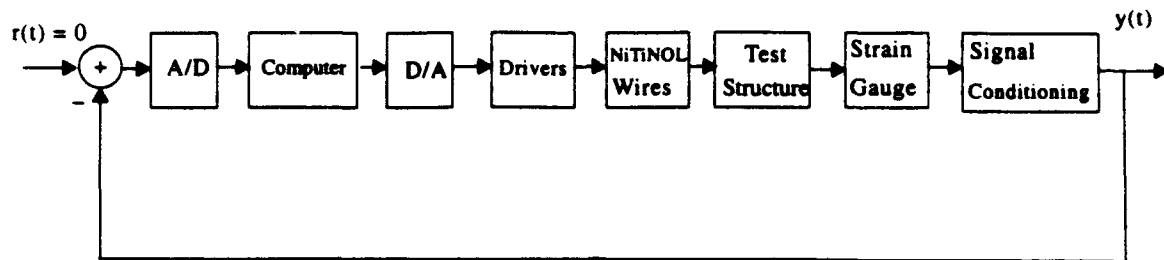


Figure 3.7. Block diagram representation of the test article

The physical implementation of the system is represented in the following diagram.

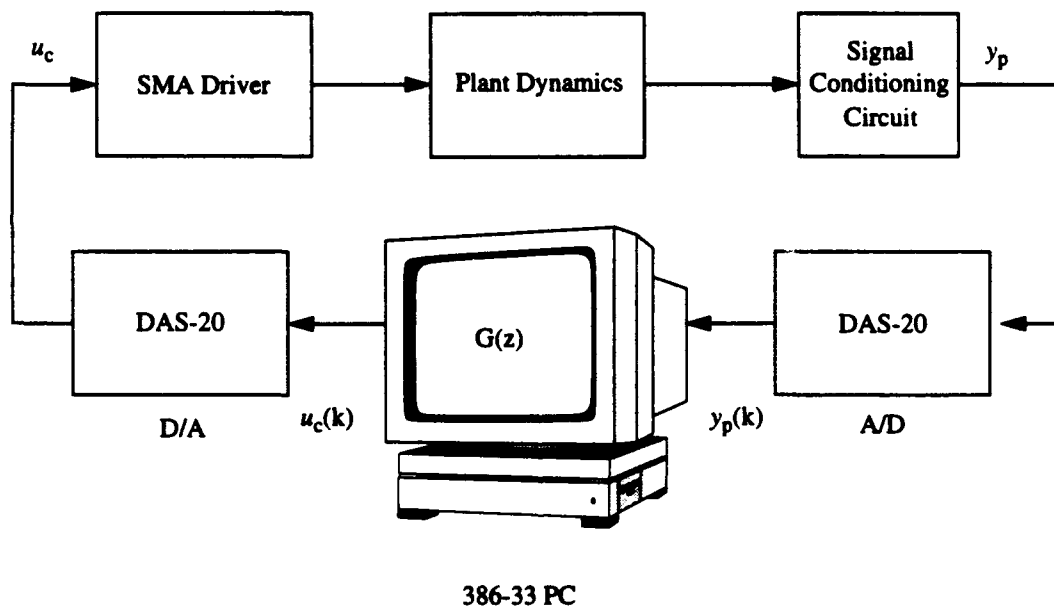


Figure 3.8. Block Diagram of Experimental Setup

4. Structural Modelling Techniques

The objective of this study was to show the effectiveness of robust control on structural behavior of smart structures. Most of these techniques rely on an accurate knowledge of the systems modal characteristics. A mathematical representation of a system can be obtained in two different ways. The first method is to generate a model based on the various laws of physics and the knowledge about the physical construction of the system. These analytical models for composite structures can be developed by using finite element methods. The second method, known as the Structural Identification Technique, utilizes the experimental input-output response of the system for deriving mathematical models of the structural systems. The results of structural identification are utilized in validating the finite element models. Juang and Pappa [92] have developed a modal parameter identification method, called the Eigensystem Realization Algorithm (ERA) for determining a mathematical model of a structure directly from experimental data. A salient feature of this method is that it allows one to include only good or strongly measured signals without loosing any capabilities. This feature of selection of appropriate data minimizes the effects of measurement noise on the identified parameters of the system. The ERA method is used for determining a mathematical model of the cantilever beam with actuators and sensors.

4.1. The Eigensystem Realization Algorithm

The Eigensystem Realization Algorithm [92] uses the Markov parameters of a system to identify a minimal order state space representation of the system. The Markov parameters of a physical system $Y(k)$ ($q = \#$ of outputs of the system, $m = \#$ of inputs) are used to form a $r \times s$ block size Hankel matrix.

$$H_{rs}(k-1) = \begin{bmatrix} Y(k) & Y(k+1) & \dots & Y(k+s-1) \\ Y(k+1) & \dots & \dots & \dots \\ \dots & \dots & \dots & \dots \\ Y(k+r-1) & \dots & \dots & Y(k+r+s-2) \end{bmatrix} \quad (1)$$

The singular value decomposition of $H_{rs}(0)$ gives

$$H_{rs}(0) = PDQ^T \quad (2)$$

where P and Q are nonsingular matrices and D is a diagonal matrix of singular values. If there are n non-zero singular values in D then the matrices P , D and Q can be truncated to a $rq \times n$ sized P_1 , a $n \times n$ sized D_1 and a $n \times ms$ sized Q_1 . Then

$$H_{rs}(0) = P_1 \times D_1 \times Q_1^T \quad (3)$$

Here n becomes the order of the identified system.

Define two matrices $E_q = [I_q, 0_q, \dots, 0_q]$ and $E_m = [I_m, 0_m, \dots, 0_m]^T$ where $I_q = q \times q$ identity matrix and

$0_n = q \times q$ zero matrix. Then the discrete state space matrices of the system are given by

$$\begin{aligned} A &= D_1^{-1/2} P_1^T H_n(1) Q_1 D_1^{-1/2} \\ B &= D_1^{1/2} Q_1^T E_n \\ C &= E_n^T P_1 D_1^{1/2} \end{aligned} \quad (4)$$

Then the system equations are

$$\begin{aligned} x(k+1) &= Ax(k) + Bu(k) \\ y(k) &= Cx(k) \end{aligned} \quad (5)$$

4.2. Observer Method of Calculating the Markov Parameters of the System

For flexible structures, it is very difficult to generate and accurately record the Markov parameters due to the small magnitude and low damping of a typical pulse response. The difficulty is compounded for MIMO systems. Hence, asymptotically stable observer formulation [93] as outlined below is used to calculate the Markov parameters of a system from its response to a random input.

The state variable equations for a system with an observer can be written as

$$\begin{aligned} \hat{x}(k+1) &= \bar{A}\hat{x}(k) + \bar{B}v(k) \\ y(k) &= C\hat{x}(k) + Du(k) \end{aligned} \quad (6)$$

where

$$\begin{aligned} \bar{A} &= A + MC \\ \bar{B} &= [B + MD, -M] \\ v(k) &= \begin{bmatrix} u(k) \\ y(k) \end{bmatrix} \end{aligned} \quad (7)$$

The matrix M is chosen such that the eigenvalues of \bar{A} are placed at any desired location. The eigenvalues of \bar{A} can be chosen to be either real or complex conjugate pairs. An outline of the formulation to calculate the system Markov parameters with real eigenvalue assignment of the observer is described below. The formulation for complex eigenvalue assignment and a combination of real and complex eigenvalue assignment follows similar steps.

The input-output relation of the above observer system can be written as

$$y(k) = \alpha \sum_{\tau=0}^{p-1} \lambda_m^{(\tau)} u(k-\tau-1) + \beta \sum_{\tau=0}^{p-1} \lambda_q^{(\tau)} y(k-\tau-1) + Du(k) \quad k \geq p \quad (8)$$

where α, β, D are the unknown observer parameters and λ 's are given by

$$\begin{aligned}\lambda_m^{(\tau)} &= [\lambda_{1,m}^{(\tau)}, \lambda_{2,m}^{(\tau)}, \dots, \lambda_{n,m}^{(\tau)}] \\ \lambda_q^{(\tau)} &= [\lambda_{1,q}^{(\tau)}, \lambda_{2,q}^{(\tau)}, \dots, \lambda_{n,q}^{(\tau)}] \\ \lambda_{1,m}^{(\tau)} &= \text{diag}(\lambda_1^{(\tau)}, \dots, \lambda_n^{(\tau)})_{m \times m}\end{aligned} \quad (9)$$

Eq.(8) can be written as

$$\begin{aligned}y(k) &= \gamma \Gamma(k-1) \\ \text{where } \gamma &= [\alpha, \beta, D] \\ \gamma &= \text{matrix of unknown observer parameters}\end{aligned} \quad (10)$$

The unknown matrix of observer parameters can be calculated recursively⁶ using the relation

$$\hat{\gamma}(i) = \hat{\gamma}(i-1) + \Delta \hat{\gamma}(i-1) \quad (11)$$

where,

$$\Delta \hat{\gamma}(i-1) = \left[\frac{\Re(i-2) \Gamma(i-1) [y(i) - \hat{\gamma}(i-1) \Gamma(i-1)]^T}{1 + \Gamma(i-1)^T \Re(i-2) \Gamma(i-1)} \right]^T \quad (12)$$

$$\Re(i-2) = \Re(i-1) - \frac{\Re(i-2) \Gamma(i-1) \Gamma(i-1)^T \Re(i-2)}{1 + \Gamma(i-1)^T \Re(i-2) \Gamma(i-1)} \quad (13)$$

The initial value of $\hat{\gamma}(i)$ and $\Re(i-2)$ are

$$\begin{aligned}\hat{\gamma}(i) &= 0_{q \times (nm+nq+m)} \\ \Re(i-2) &= 10000 \times I_{(nm+nq+m) \times (nm+nq+m)}\end{aligned} \quad (14)$$

Once the observer parameters are calculated using Eq.(11), Eq.(12) and Eq.(13), the Markov parameters of the system can be calculated using the following relation

$$Y_t = \alpha \lambda_m^{(t)} + \beta \left[\sum_{i=0}^{t-1} \lambda_q^{(i)} Y_{t-i-1} + \lambda_q^{(t)} D \right] \quad (15)$$

4.3. The MDVV Linear System Identification Algorithm

This algorithm to identify a linear state space model of a system from experimental test data was suggested by Moonen, DeMoor, Vandenberghe and Vandewalle (MDVV). [94]

The MDVV algorithm is based on the system identification method using the canonical variate analysis by Larimore. [95] The algorithm is a 2 step procedure to get a minimal order state space realization of a system from experimental random input output data. First, a state vector sequence is realized as the intersection of the row spaces of two block Hankel matrices constructed using the input output data. Then the system matrices are obtained from the least-squares solution of a set of linear equations involving the states calculated in the first step and the input output data. The steps involved in the MDVV algorithm are as follows

Step 1. Form H_1 , H_2 and H as shown

$$H_1 = \begin{bmatrix} u(k) & u(k+1) & u(k+j-1) \\ y(k) & y(k+1) & y(k+j-1) \\ u(k+1) & u(k+2) & u(k+j) \\ y(k+1) & y(k+2) & y(k+j) \\ u(k+i-1) & u(k+i) & u(k+j+i-2) \\ y(k+i-1) & y(k+i) & y(k+j+i-2) \end{bmatrix} \quad (16)$$

$$H_2 = \begin{bmatrix} u(k+i) & u(k+i+1) & u(k+i+j-1) \\ y(k+i) & y(k+i+1) & y(k+i+j-1) \\ u(k+i+1) & u(k+i+2) & u(k+i+j) \\ y(k+i+1) & y(k+i+2) & y(k+i+j) \\ u(k+2i-1) & u(k+2i) & u(k+j+2i-2) \\ y(k+2i-1) & y(k+2i) & y(k+j+2i-2) \end{bmatrix} \quad (17)$$

$$H = \begin{bmatrix} H_1 \\ H_2 \end{bmatrix} \quad (18)$$

where $u(k)$ and $y(k)$ are m and q dimensional vectors of system input and output respectively.

Step 2. Form the singular value decomposition of H

$$H = USV^T = \begin{bmatrix} U_{11} & U_{12} \\ U_{21} & U_{22} \end{bmatrix} \begin{bmatrix} S_{11} & 0 \\ 0 & 0 \end{bmatrix} V^T \quad (19)$$

here the sizes of the matrices are

$$\begin{aligned} \text{size}(S_{11}) &= (2mi + n) \times (2mi + n) \\ \text{size}(U_{11}) &= (mi + qi) \times (mi + qi) \\ \text{size}(U_{12}) &= (mi + qi) \times (2qi - n) \\ \text{size}(U_{21}) &= (mi + qi) \times (2mi + n) \\ \text{size}(U_{22}) &= (mi + qi) \times (2qi - n) \end{aligned} \quad (20)$$

Step 3. Form the singular value decomposition of the product $U_{12}^T U_{11} S_{11}$ as shown

$$U_{12}^T U_{11} S_{11} = [U_q U_q^\perp] \begin{bmatrix} S_q & 0 \\ 0 & 0 \end{bmatrix} \begin{bmatrix} V_q^T \\ V_q^{T\perp} \end{bmatrix} \quad (21)$$

where U_q is a $(2qi - n) \times n$ matrix.

Step 4. Then the identified n th order model is given by

$$\begin{bmatrix} A & B \\ C & D \end{bmatrix} = \begin{bmatrix} U_q^T U_{12}^T U(m+q+i:(i+1)(m+q)::)S \\ U(mi+qi+m+1:(m+q)(i+1),:)S \end{bmatrix} \begin{bmatrix} U_q^T U_{12}^T U(1:(m+q)i,:)S \\ U(mi+qi+1:mi+qi+m,:)S \end{bmatrix}^\dagger \quad (22)$$

4.4. Swept Sinewave Testing Method

This is a conventional method to obtain a transfer function model of a system from experimental test data. In this method, a system is excited using sinusoidal inputs within a certain frequency range. The output

of the system is recorded and the magnitude and phase is plotted against frequency. A curve fitting technique is used to generate a transfer function model of the system from the recorded frequency response plot (bode plot). The whole procedure of recording the data followed by the curve fitting analysis was automated using the HP 35665A spectrum analyzer.

4.5. Experimental Results on the Cantilever Beam Test Article

The three methods viz. the Observer-ERA method, the MDVV method and the swept sinewave testing method were used to generate a model of the cantilever beam. For the Observer-ERA and the MDVV algorithm the experimental data used was the response of the beam to a uniformly distributed random input for 60 seconds at 5 Hz sampling frequency. In the Observer-ERA algorithm, various sets of observer poles and window size were selected and the response of the model generated using each of the sets was compared to the frequency response of the beam. Finally, we selected observer poles at $-0.9 \pm j0.2$, $-0.8 \pm j0.31$ and ± 0.1 and a window size p of 90. The frequency as well as the time response of the model generated using this set matched that of the beam over the frequency range of interest as shown in Figures 4.1 and 4.2. Another experimentally derived model was generated using a HP35665A spectrum analyzer. This model was produced using sinusoidal inputs between 0.1 Hz and 2 Hz and the curve fitting software available with the analyzer. This model was called the swept sine model (SSW). The third model was obtained using the MDVV algorithm on the same sequence of input output data that was used in the Observer-ERA algorithm.

For comparison, the Markov parameters generated by the Observer-ERA method, and the MDVV algorithm are plotted in Fig. 4.1 along with the pulse response of the swept sine model. For clarity, only the first 20 Markov parameters have been shown. The symbols on the plot show the values of the calculated Markov parameters.

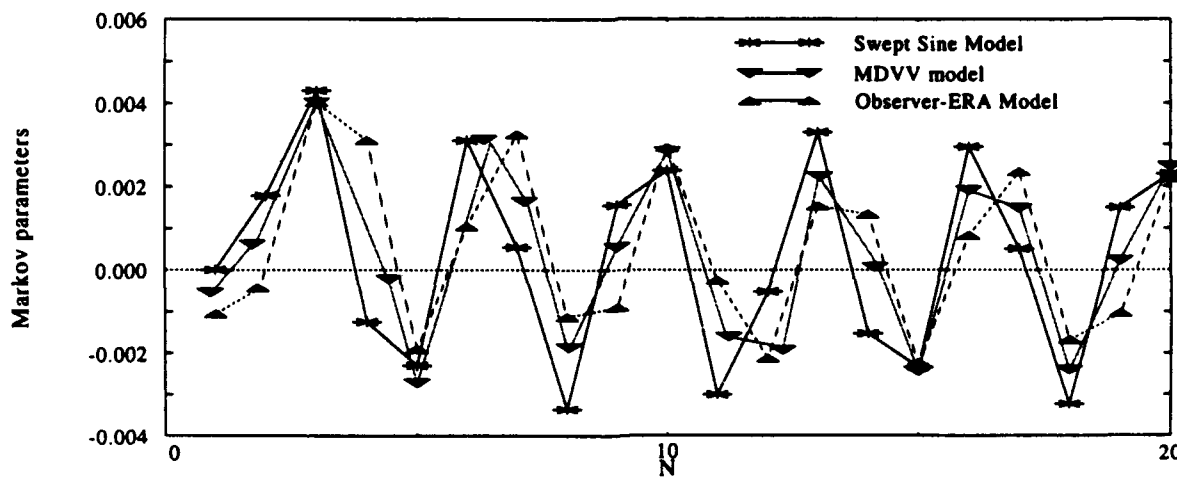


Figure 4.1. Comparison of the calculated Markov parameters

Once the Markov parameters have been calculated, the ERA can be used to identify a model of the test

article. The discrete time model ($T = 0.2$ sec) of the cantilever beam generated using the Observer-ERA method is given by

$$\Phi_{obs} = \begin{bmatrix} -0.1956 & -0.9409 & 0.1873 \\ 0.9409 & -0.3737 & -0.0896 \\ 0.1873 & 0.0896 & 0.5492 \end{bmatrix} \quad \beta_{obs} = \begin{bmatrix} 0.0366 \\ -0.0416 \\ 0.0311 \end{bmatrix} \quad C_{obs} = \begin{bmatrix} 0.0366 & 0.0416 & 0.0311 \end{bmatrix} \quad (23)$$

The equivalent continuous time transfer function of the system in Eq. (22) is

$$G_{obs}(s) = \frac{-0.0074s^2 + 0.0071s + 1.0233}{s^3 + 2.8153s^2 + 88.9844s + 237.3496} \quad (24)$$

In comparison, the discrete time state space model ($T = 0.2$ sec) of the cantilever beam generated using the MDVV algorithm is

$$\Phi_{mdvv} = \begin{bmatrix} -0.1642 & -9.3596 & -19.318 \\ 0.0836 & 0.064 & -1.9318 \\ 0.0084 & 0.1064 & 0.8068 \end{bmatrix} \quad \beta_{mdvv} = \begin{bmatrix} 0.1869 \\ 0.0187 \\ 0.0017 \end{bmatrix} \quad C_{mdvv} = \begin{bmatrix} -0.0008 & -0.0544 & -0.5853 \end{bmatrix} \quad (25)$$

The continuous time transfer function equivalent of Eq. (24) is

$$G_{mdvv}(s) = \frac{0.01s^2 - 0.0059s - 1.3482}{s^3 + 2.7302s^2 + 88.8654s + 231.12} \quad (26)$$

Finally, the Swept Sine Model is given by Eq. (26)

$$G(s) = \frac{1.55}{s^3 + 1.6502s^2 + 88.925s + 136.8651} \quad (27)$$

The comparison of the frequency response of the three models in Eqs. (23), (25) and (26) and the measured frequency response of the beam is shown in Fig. 4.2.

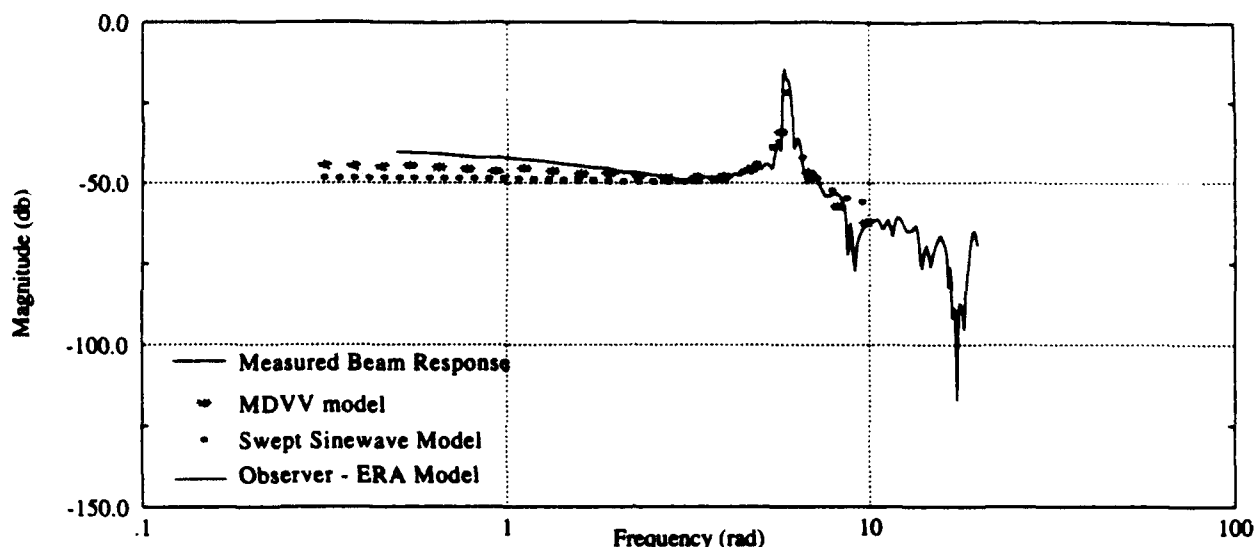


Figure 4.2. Comparison of the frequency responses

Figure 4.2 shows that there is an acceptable match between the frequency of the first mode of the three models and the measured frequency response of the beam. From Fig. 4.1 and 4.2 we can conclude that any of the three mathematical models obtained is a plausible structural model of the cantilever beam system.

4.6. Experimental Results on the Three Mass System

An experimental model was obtained for the test article from frequency response data acquired with a HP35665A dynamic signal analyzer. Four transfer functions were obtained for the two input-two output system. For each measurement, the analyzer's source sweeps the desired frequencies in a series of very small steps. The input signal power is automatically adjusted at each frequency in the sweep to provide the optimal signal to noise ratio. An advantage of this swept sine measurement is that all of the energy in the frequency response test is concentrated at the desired frequency which gives good excitation of the structural system [96,97,98]. Modal frequencies taken from the bode plots of the system are listed in Table (4.8). From this table it can be seen that the frequency of the modes is a function of the actuator used to excite the beam. The frequency of the modes is also dependent upon the initial tension in the SMA wires.

Table 4.8. 3-Mass System Modal Frequencies

Mode	Experimental - Force Actuators (Hz)	Experimental - Moment Actuators (Hz)
1	0.96	0.90
2	2.54	2.37
3	3.31	3.09

For each of the four transfer functions, a model was generated by the HP analyzer's built-in curve fitting program. The curve fitting program derives a linear system model from the measured frequency response

data. A pole/zero model is developed by calculating a weighted least squares fit of the frequency response data to a rational polynomial. The curve fitting is performed in the s-domain so that the program determines the transfer function. Due to control structure interaction, each actuator generates two 8th order transfer functions with similar complex poles. A common denominator for all 4 transfer functions was then generated by compromising between the two sets of frequencies. [99] The measured transfer functions and the resulting "fitted" curves are shown in Fig. 4.3.

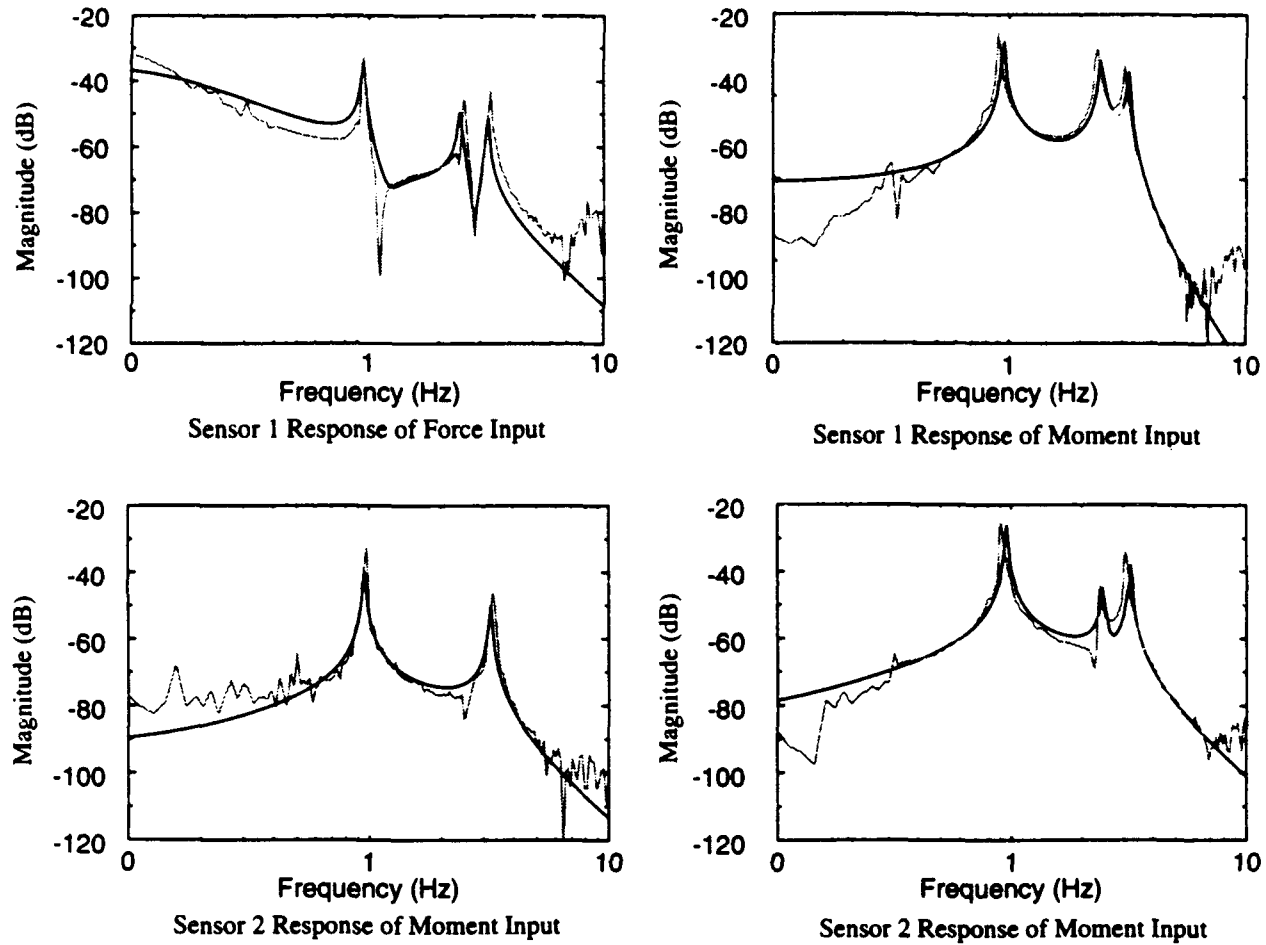


Figure 4.3. Measured Transfer Functions (Dashed) and Fitted Curves (Solid)

The corresponding numerators were modified so that the four transfer functions could be written as

$$\begin{bmatrix} Y_1(s) \\ Y_2(s) \end{bmatrix} = H(s) \begin{bmatrix} U_1(s) \\ U_2(s) \end{bmatrix} \quad \text{where} \quad H(s) = \frac{1}{d(s)} \begin{bmatrix} N_{11} & N_{12} \\ N_{21} & N_{22} \end{bmatrix} \quad (28)$$

where

$$\begin{aligned}
d(s) &= s^8 + 2.89s^7 + 6.82 \times 10^2 s^6 + 1.77 \times 10^3 s^5 + 1.21 \times 10^5 s^4 + 2.75 \times 10^5 s^3 + 3.64 \times 10^6 s^2 + 7.42 \times 10^6 s + 3.95 \times 10^6 \\
N_{11} &= 8.48 \times 10^{-1} s^5 + 2.53 s^4 + 3.07 \times 10^2 s^3 + 1.17 \times 10^3 s^2 + 1.32 \times 10^4 s + 7.68 \times 10^4 \\
N_{12} &= -3.14 \times 10^{-1} s^3 - 1.64 \times 10^3 s^2 - 2.42 \times 10^3 s - 1.10 \times 10^3 \\
N_{21} &= 2.18 \times 10^{-3} s^6 + 4.59 \times 10^{-1} s^5 + 2.06 s^4 - 1.11 \times 10^2 s^3 - 3.24 \times 10^2 s^2 - 3.19 \times 10^2 s - 1.04 \times 10^2 \\
N_{22} &= -1.96 s^5 - 9.85 \times 10^4 s^4 - 5.31 \times 10^2 s^3 - 1.36 \times 10^3 s^2 - 1.12 \times 10^3 s - 2.81 \times 10^3
\end{aligned}$$

4.7. Determination of State Variable Representation from Transfer Function Matrix [99,100]

Even though the transfer function matrix has been determined, the state space representation is needed for the model so that LQG/LTR controllers can be designed. The desired form of the model is contained in Eq. (29).

$$\begin{aligned}
\dot{\hat{x}} &= A_p \hat{x} + B_p u \\
\hat{y} &= C_p \hat{x} + D_p u
\end{aligned} \tag{29}$$

The state space realization will be a controller-form realization from a right matrix fraction description (MFD). First, the TFM must be in the form of a strictly proper right MFD having the form given in Eq. (30).

$$H(s) = N(s) D^{-1}(s) \tag{30}$$

In order to obtain a strictly proper right MFD, the TFM was transformed into a Smith McMillian form given in Eq. (31).

$$H(s) = \frac{\Lambda(s)}{d(s)} \tag{31}$$

After performing pole/zero cancellations in the Smith McMillan form, the minimal order of the system was determined to be 14. Equation (32) contains the minimal order, column reduced transfer function matrix.

$$H(s) = N_r(s) D_r^{-1}(s) \tag{32}$$

Once the TFM is in the form of a strictly proper right MFD, a controller form state space realization can be obtained. First, rewrite $D_r(s)$ as shown in Eq. (33).

$$D_r(s) = D_{hc} S(s) + D_{lc} \Psi(s) \tag{33}$$

where,

$$S(s) = \text{diag}(s^{k_1}, s^{k_2})$$

$$\Psi^T(s) = \begin{bmatrix} s^{k_1-1} & s^{k_1-2} & \dots & s & 1 & 0 \\ 0 & & & s^{k_2-1} & s^{k_2-2} & \dots & s & 1 \end{bmatrix}$$

and k_1, k_2 are the column degrees of $D_r(s)$, $D_{hc(s)}$ is the highest column degree coefficient matrix of $D_r(s)$

Once the matrices in Eq. (33) are determined, the state space realization can be formed using the matrix definitions given in Eqs. (34) through (36).

$$A_p^o = \text{block diag}\left(\begin{bmatrix} 0 & 0 & 0 \\ 1 & \dots & 0 \\ 0 & 1 & 0 \end{bmatrix}, k_i x k_i, i = 1, 2\right) \quad (34)$$

$$(B_p^o)^T = \text{block diag}([1 \ 0 \ \dots \ 0], 1 \times k_i, i = 1, 2) \quad (35)$$

$$C_p^o = I_2 \quad (36)$$

Finally, the state space matrices are obtained using Eqs. (37) through (39)

$$A_p(s) = A_p^o - B_p^o D_{hc}^{-1} D_{lc} \quad (37)$$

$$B_p = B_p^o D_{hc}^{-1} \quad (38)$$

$$C_p = N_{lc} \quad (39)$$

where,

$$N_r = N_{lc} \Psi(s)$$

4.8. Formulation of Reduced Order State Space Model [101]

Next to reduce the order of the controller and allow for the modelling and control of complex systems, a reduced order model was developed. The reduced order model of the system was acquired utilizing the balance and truncation methodology. First, an internally balanced representation of the system is obtained in

which the controllability and observability Gramians (given in Eq. (40)) are equal and diagonal.

$$\Sigma = \text{diag}(\sigma_1, \sigma_2, \dots, \sigma_n) \quad (40)$$

with

$$\sigma_1 \geq \sigma_2 \geq \dots \geq \sigma_n \quad (41)$$

The σ_i 's are Hankel singular values. The order of the reduced order model is determined by retaining the dominant Hankel singular values. Once the dominant values have been determined, the state space model is partitioned as in Eq. (41)

$$\begin{bmatrix} A_{bal} & B_{bal} \\ C_{bal} & D_{bal} \end{bmatrix} = \begin{bmatrix} [A_{11} \ A_{12}] & [B_1] \\ [A_{21} \ A_{22}] & [B_2] \\ [C_1 \ C_2] & D \end{bmatrix} \quad (42)$$

where $A_{11} \in R^{r \times r}$, $A_{22} \in R^{(n-r) \times (n-r)}$, r is the number of dominated Hankel singular values, and $(n-r)$ is the number of nondominant values.

Finally, after the partitioning is completed, the reduced order model is determined as in Eq. (43)

$$\begin{aligned} \dot{\hat{x}}_r &= A_r \hat{x}_r + B_r u \\ \hat{y}_r &= C_r \hat{x}_r + D_r u \end{aligned} \quad (43)$$

where,

$$\begin{aligned} A_r &= A_{11}; & B_r &= B_1 \\ C_r &= C_1; & D_r &= D \end{aligned} \quad (44)$$

\hat{x}_r = reduced order state vector

4.9. Modelling Results

A comparison of the frequency response of the transfer function matrix and the reduced order model is given in Fig 4.4. This figure shows that the reduced order model produces a close representation of the response of the transfer function matrix.

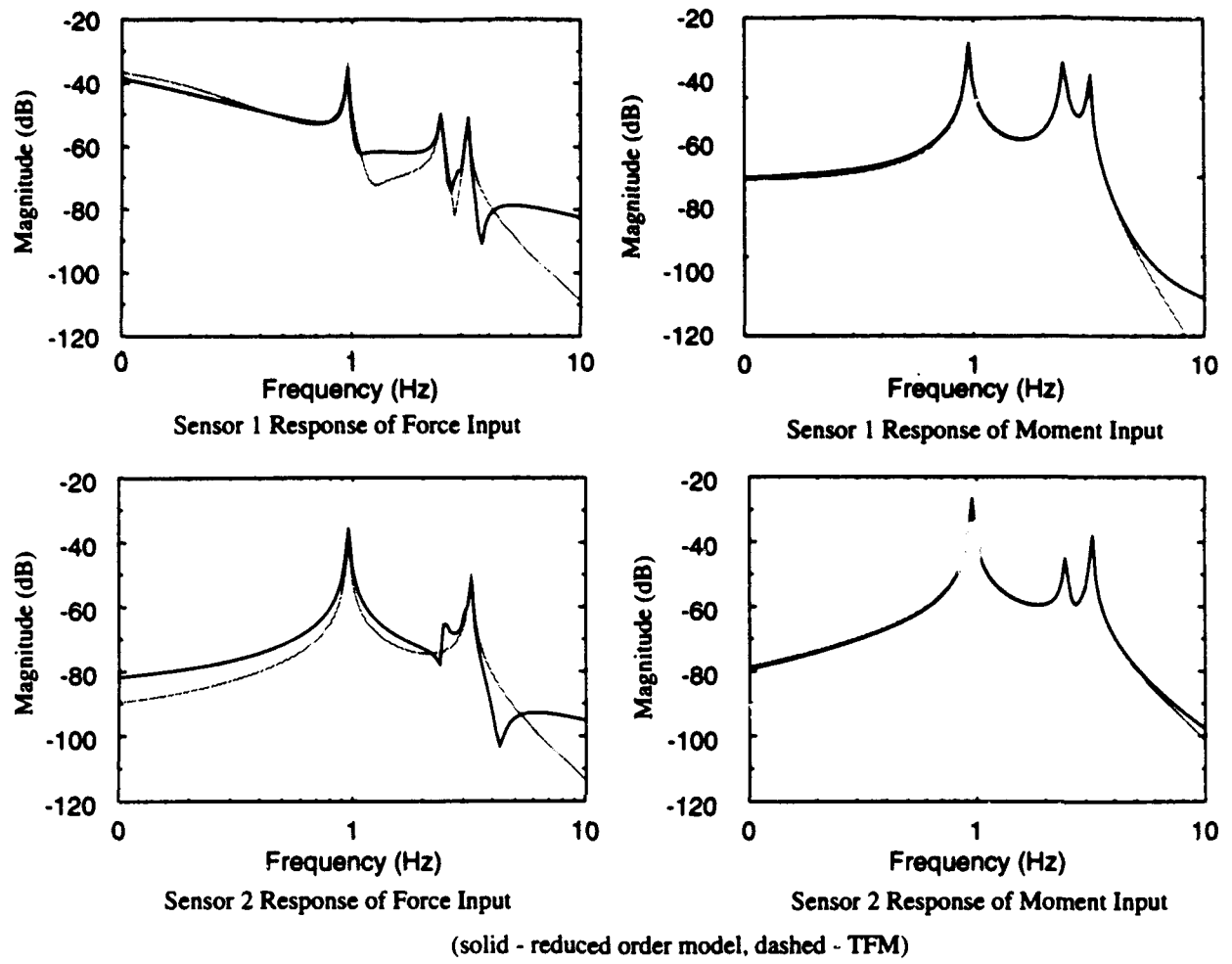


Figure 4.4. Comparison of Frequency Response

The next figure shows the comparisons of the frequency response of the models obtained using the Observer-ERA algorithm, MDVV algorithm and the frequency response of the three mass system recorded by the HP 35665A spectrum analyzer.

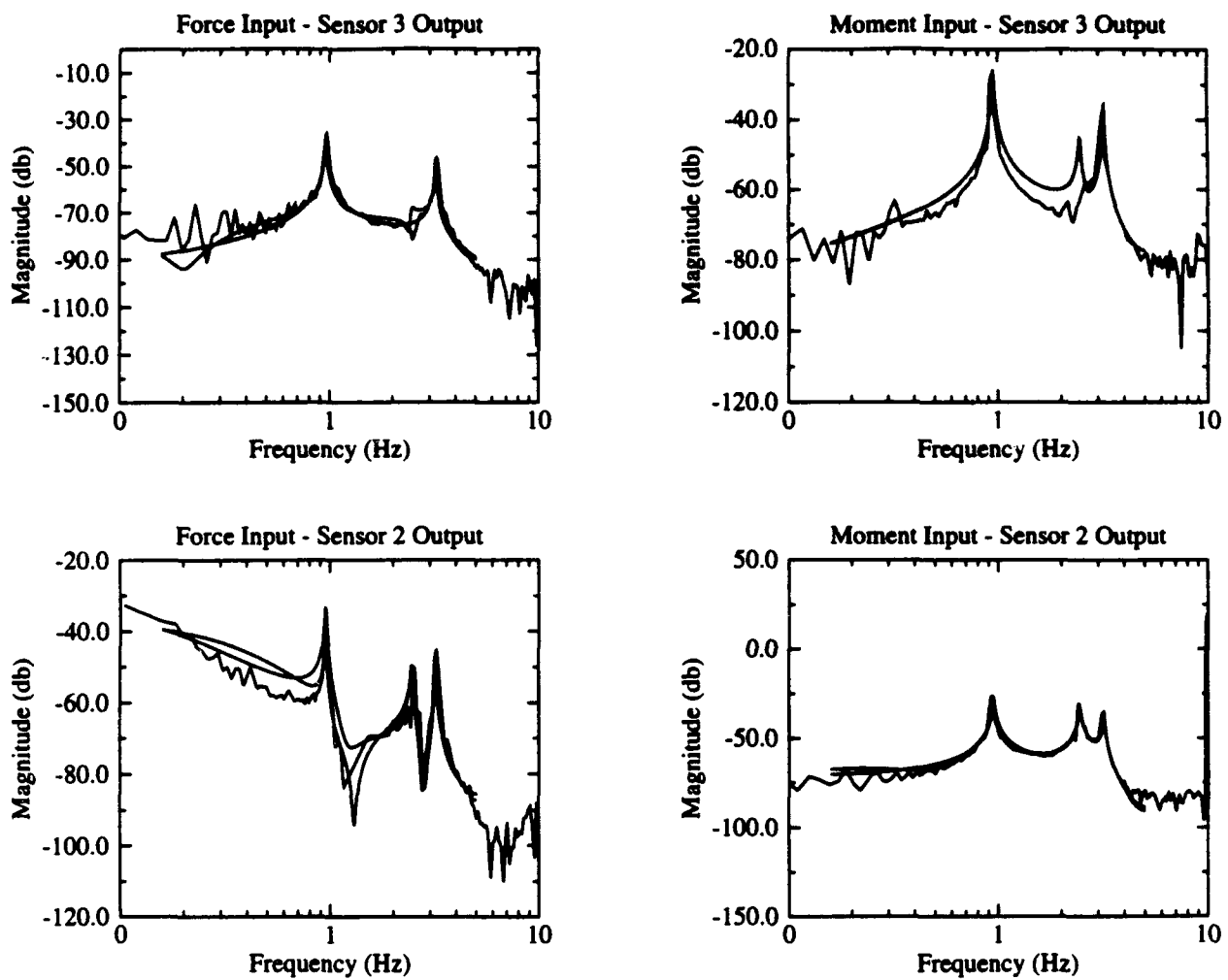


Figure 4.5. Comparison of Frequency Responses

Figures 4.4 and 4.5 shows that the state space models obtained from the Observer-ERA, the MDVV algorithm and the swept sine testing method give a fairly good representation of the three mass structure. Therefore any of the above models can be used to design conventional as well as robust controllers.

5.0 Controller Design Methodologies

The design and implementation of control strategies for large, flexible smart structures presents challenging problems. To demonstrate the capabilities of shape-memory-alloy actuators, we have designed and fabricated a three-mass test article with multiple shape-memory-alloy (NiTiNOL) actuators. The force and moment actuators were implemented on the structure to examine the effects of control structure interaction and to increase actuation force. These SMA actuators exhibit nonlinear effects due to deadband and saturation. The first step in the modeling process was the experimental determination of the transfer function matrix derived from frequency response data. A minimal state space representation was determined based on this transfer function matrix. Finally in order to reduce the order of the controller, a reduced order state space model was derived from the minimal state space representation. The simplified analytical models are compared with models developed by structural identification techniques based on vibration test data.

From the reduced order model, a controller was designed to dampen vibrations in the test bed. To minimize the effects of uncertainties on the closed-loop system performance of smart structures, a LQG/LTR control methodology has been utilized. An initial standard LQG/LTR controller was designed; however, this controller could not achieve the desired performance robustness due to saturation effects. Therefore, a modified LQG/LTR design methodology was implemented to accommodate for the limited control force provided by the actuators. The closed-loop system response of the single input-single output and multiple input-multiple output (MIMO) test articles with robustness verification have been experimentally obtained and presented in the sections. The modified LQG/LTR controller demonstrated performance and stability robustness to both sensor noise and parameter variations.

5.1 Classical Control Design Methods

As a first step toward the design of closed loop controllers for smart structures, classical control algorithms have been designed and implemented on test articles. The salient results are presented in this section.

5.1.1 Actuator Dynamics

The first task was to model the Nitinol wire. The wire was given an initial 3% of permanent strain, mounted in a test fixture, and then heated past the phase transition temperature via electrical resistance heating. Figure 5.1 shows a typical experimental heating-cooling cycle.

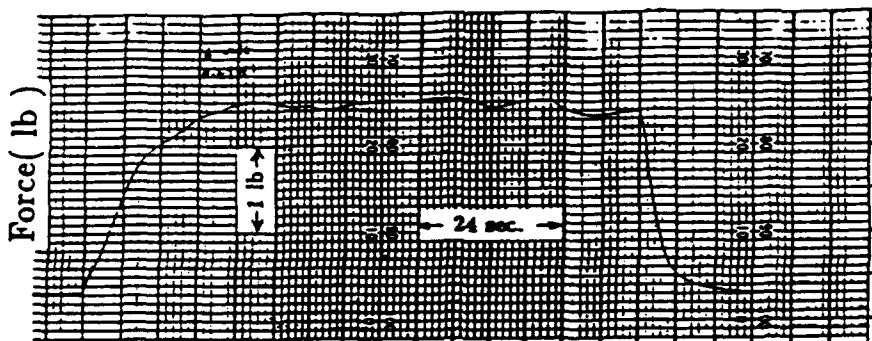


Figure 5.1. Typical heating-cooling cycle of Nitinol wire

This resulting force-time history indicates that a first-order model is an appropriate approximation, in the form of Eq. (1)

$$\tau \dot{F} + F = a_b P \quad (1)$$

where F = force, τ = time constant, a_b = slope of force-vs-power curve, $P = V^2/R$ = power supplied to wire, V = voltage, and R = electrical resistance of the wire. Figure 5.2 shows the experimentally-derived curve of τ vs. P . The value of τ selected was $\tau = 5$ sec on the basis that typical power levels were in the 2-4 watt range. Figure 5.3 shows a typical value of steady-state force vs. power having a slope of about 1.25 lb/watt for a 42-inch Nitinol wire having an initial permanent strain of 3%. Equation (1) gives a nonlinear relation between force and voltage. The voltage was supplied by a power driver for which the voltage V was given by $V = 2.2 V_{pc}$, where V_{pc} was the output of the PC which was used to generate the control action. Hence, Eq. (1) has the form (for the 42-inch wire which had a resistance of 18Ω)

$$5\dot{F} + F = 0.336 V_{pc}^2 \quad (2)$$

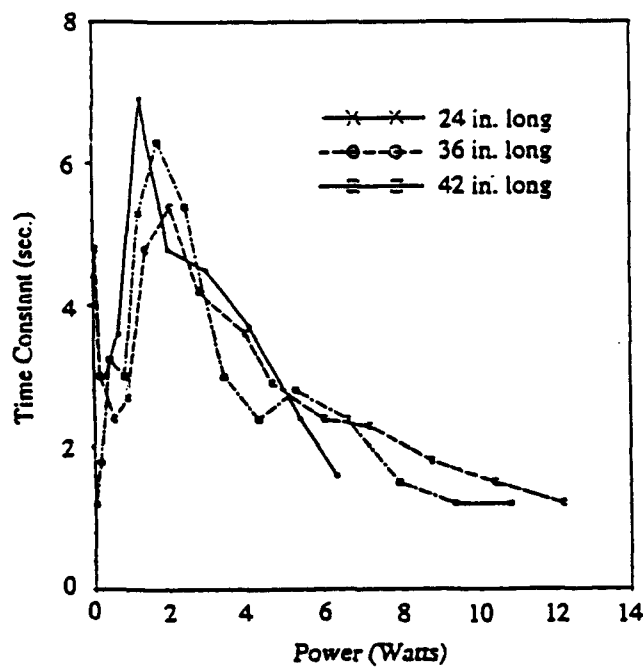


Fig 2. Time constants of 3%-strained Nitinol Wire
(10 mils)

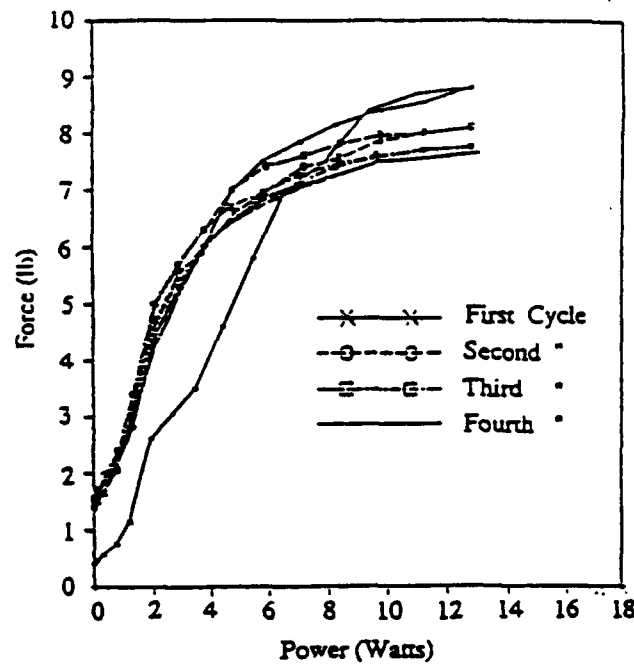


Fig 3. Force curve of 42" wire

Equation (2) is a nonlinear equation between force and voltage. Linearization of Eq. (2) about a nominal voltage of $V_{pc} = 2.5v$ leads to

$$5f + f = 1.68V_{pc} \quad (3)$$

to which corresponds the transfer function

$$G_a(s) = \frac{0.336}{s + 0.2} \quad (4)$$

When tested experimentally only 3.75 lb of force was generated when the D/A port of the PC applied 5 volts to the wire. This led to a modification of the numerator of $G_a(s)$ so that Eq. (4) was replaced by

$$G_a(s) = \frac{0.15}{s + 0.2}. \quad (5)$$

It is this empirical $G_a(s)$ which was used to represent the actuator in the controller design for the cantilever beam. Similar reasoning led to

$$\begin{aligned} G_a(s) &= \frac{0.27}{s + 0.2} \quad \text{for the 54"-wire} \\ &= \frac{0.302}{s + 0.2} \quad \text{for the 24"-wire.} \end{aligned} \quad (6)$$

These two latter wires were used in the three-mass simulation and experiment.

Another experiment performed on the Nitinol wire had to do with how the generated force was affected by the frequency at which applied voltage was turned on and off. As this frequency was increased, the effective force that could be generated decreased, mainly because there was not sufficient time for the wire to cool before it was reheated. This tended to inhibit the transition back and forth between the martensite and austenite phases. In the experiment no artificial means were used to cool the wires, such as blowing air over the wires by means of fans. Table 5.1 shows the effect of frequency on the effective force that could be generated by the 54" Nitinol wire. Clearly, its effectiveness in the present application appears to be limited to systems with frequencies below 2 Hz. The transfer functions in Eqs. (5) and (6) do produce the type of behavior exhibited in Table 5.1.

Table 5.1. Effective Force of Nitinol Wire (54 inch)

Frequency (Hz)	Peak-to-Peak Force (lb)	Frequency (Hz)	Peak-to-Peak Force (lb)
0.2	1.44	1.0	0.24
0.3	0.92	1.2	0.20
0.4	0.72	1.4	0.16
0.5	0.64	1.5	0.13
0.6	0.40	1.7	0.12
0.7	0.36	1.9	0.10
0.8	0.32	2.1	0.08
0.9	0.25		

5.1.2 Cantilever Beam

Two 42-inch Nitinol wires were used on each side of a cantilevered aluminum beam of length 47". The beam was 6" wide and 0.125-inch thick with a tip mass of maximum weight 6.44 lb which was used to vary the fundamental frequency of the beam. Figure 5.4 shows a schematic diagram of the experiment. Two Nitinol wires ran the length of the beam and were alternately heated and cooled to act in a differential-type actuator mode. A strain gage mounted at the root of the beam was used as a sensor.

5.1.3 Beam Transfer Function

A finite element model was formulated for the cantilever beam. Three-element and 10-element models gave virtually identical results for the lower frequencies. Table 5.2 shows a comparison between the FE calculations and experimental results for three different tip masses. It is evident that only the fundamental mode is capable of being affected by the shape memory action of the Nitinol wire. Hence, the beam experiment was limited to a single-input/single-output control problem. To aid in the design of the controller, the transfer function for the fundamental mode of the cantilever beam must be formulated.

Table 5.2. Comparison of Natural Frequency (Hz)

Tip Mass (lb)	Mode	Experiment	NASTRAN
0.00	1	1.60	1.75
	2	10.8	11.3
	3	30.0	32.0
1.146	1	1.20	1.17
	2	8.80	9.21
	3	26.0	27.7
6.437	1	0.58	0.62
	2	7.20	8.62
	3	23.2	22.1

The differential equation (based on the finite element model) for the fundamental mode was computed to be

$$\ddot{q}_1 + 0.0235 \dot{q}_1 + 15.31q_1 = 1.684m_a(t) \quad (7)$$

where q_1 is the generalized coordinate for the fundamental mode. An experimentally-measured damping ratio of 0.30% has been added to the equation. On the right side of Eq. (7), $m_a(t)$ is the moment applied by the Nitinol actuators. The actuators stand off the neutral axis of the beam by 1.5", and the effect of the axially-directed actuator force (maximum of about 5 lb) is neglected. If $f(t)$ is the force generated by the Nitinol wire, then $m_a(t) = 1.5 f(t)$. Furthermore, in the transformation from global coordinates to the modal coordinates that generated Eq. (7), the tip displacement y_T turned out to equal q_1 , so that the equation for the beam tip displacement is

$$\ddot{y}_T + 0.0235 \dot{y}_T + 15.31 y_T = 2.526f(t). \quad (8)$$

This tip displacement is sensed with a strain gage mounted at the root of the beam. Hence, the voltage output of the strain gage is proportional to y_T , and is given by

$$\ddot{v} + 0.0235\dot{v} + 15.31v = 2.526a f(t) = a_f f(t) \quad (9)$$

where $a_f = 2.526a$, and a is the constant of proportionality between the strain gage output and the tip displacement. This parameter was obtained experimentally. When a force $f(t) = 2.7$ lb was generated in the Nitinol wire, the strain gage output was measured at 0.011 volts. Hence, $a_f = 0.0624$ volt/lb, and Eq. (9) becomes

$$\ddot{v} + 0.0235\dot{v} + 15.31v = 0.0624f(t) . \quad (10)$$

Corresponding to Eq. (10), the transfer function between the strain gage output and the actuator force is

$$G_p(s) = \frac{0.0624}{s^2 + 0.0235s + 15.31} \quad (11)$$

Figure 5.5 shows the block diagram for the control system, including the Nitinol actuator and beam dynamic model.

To verify Eq. (11), the frequency response of the cantilever beam with actuator was computed and compared with experiment. Figure 5.6 shows a Bode plot of the theoretical model and Fig. 5.7 is a Bode plot of the actual system. The comparison between them is quite acceptable. It is noted that the phase angle is -45° at a frequency of 0.2 rad/sec. This would correspond to the $(s+0.2)$ factor in the denominator of the transfer function for the actuator.

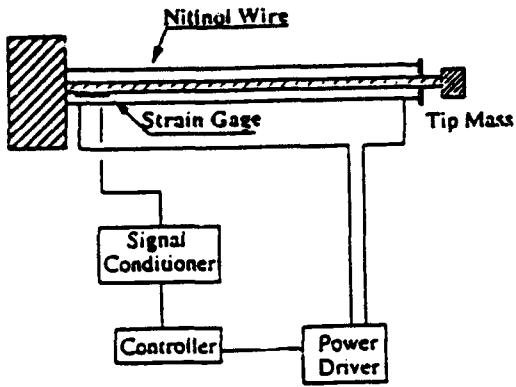


Fig. 5.4 Experimental Setup

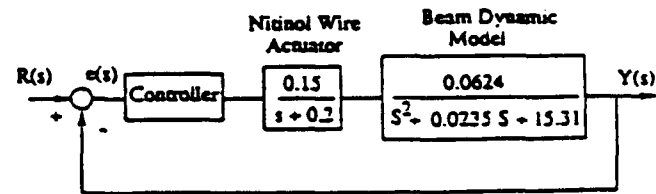


Fig. 5.5 Block Diagram of Cantilever Beam with Actuator

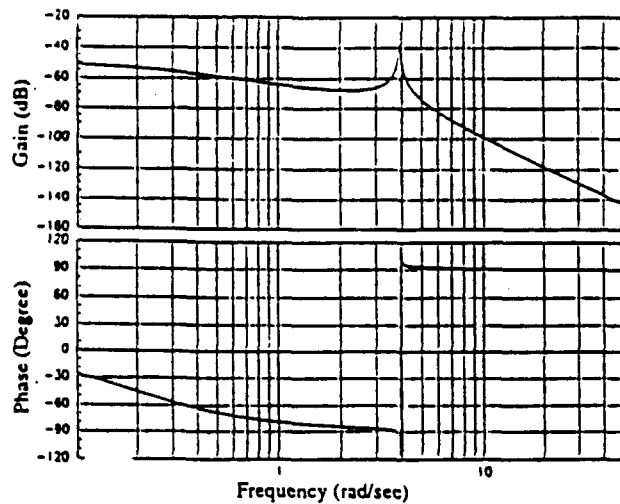


Fig. 5.6 Theoretical Bode plot

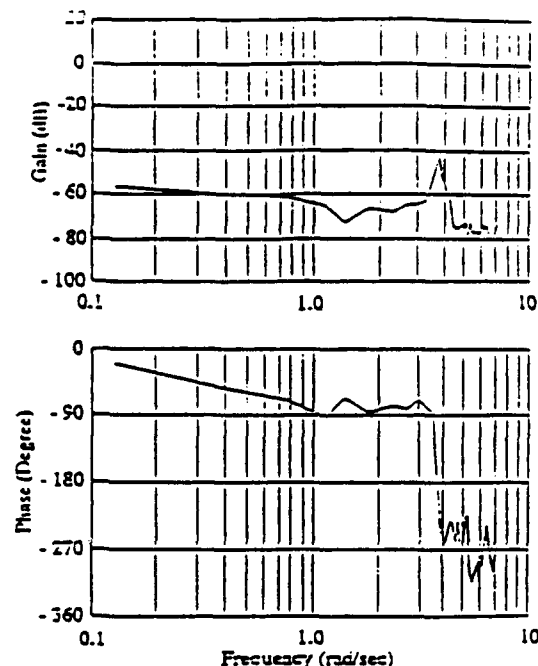


Fig. 5.7 Experimental Bode plot

Simulation

Several control algorithms were employed in the simulation of the entire system. The baseline was an open-loop system with the Nitinol wires attached, but inactive. Then an "on-off" control algorithm was examined, as well as proportional, proportional-plus-integral, and robust. The robust controller was designed using standard MATRIX_x software. Figures 5.8 - 5.12 show the simulated open-loop response, and responses for the on-off, P, PI, and robust controller, respectively. The gains of the classical P and PI control were selected by varying them so as to obtain the best performance in terms of smallest decay time, without going unstable. The gains used were $K_p = -350$ for P-control, and $K_p = -200$, $K_i = 100$ for PI control. A Routh-Hurwitz stability analysis for the P-controlled system indicated stability for $(-327) < K_p < 38$. Because of small differences between the simulation and the actual system, the lower limit on the experimental K_p was actually about (-350) instead of the theoretical value of (-327). In both simulation and experiment, the negative gain gave better results than did the positive gain.

Experimental results

Figures 5.13 - 5.17 show the experimental results for the open-loop response, and the on-off, P, PI, and robust controllers, respectively. The free vibration, in all cases, was induced by an initial displacement of the tip of the beam. The tip mass was at maximum value of 6.44 lb to give the beam a fundamental frequency of 0.623 Hz. Comparisons with the corresponding simulation curves shows good correlation. This is summarized in Table 5.3, where (for convenience) the time required to reduce the vibration amplitude to 10% of its initial value is used as a measure of effectiveness of the control algorithm. The corresponding open-loop decay time was 220 seconds.

Table 5.3. Summary of 10% Settling Time

Controller Type	Simulation (sec)	Experimental Results (sec)
On-Off	37	38
P	22	24
PI	36	34
LQG/LTR	19	17

5.1.4 Three-Mass System

To work with an MIMO case, a three-mass system was constructed, as shown in Fig. 5.18. The three weights were $W_1 = 23.2$ lb, $W_2 = 19.3$ lb, and $W_3 = 15.4$ lb. The three springs had spring

lengths of 23", 19", and 18", respectively. The upper spring was 2" x 0.090", and the lower two were 2" x 0.080". The weights were steel; the springs, aluminum. Two sets of Nitinol wires were used: 54-inch wires running lengthwise, and 24-inch wires crisscrossing above the uppermost mass, as shown in Fig. 5.18. Figure 5.18 also shows a schematic of the experimental setup. Two full-bridge 1000-ohm strain gages were used as sensors and were located in the top and bottom springs as indicated in Fig. 5.18.

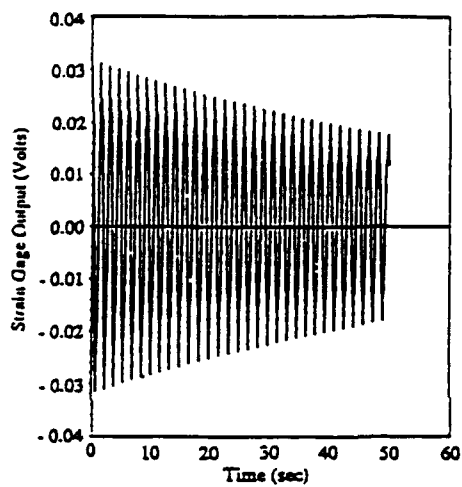


Fig. 5.8 Open-loop simulation with inactive wires.

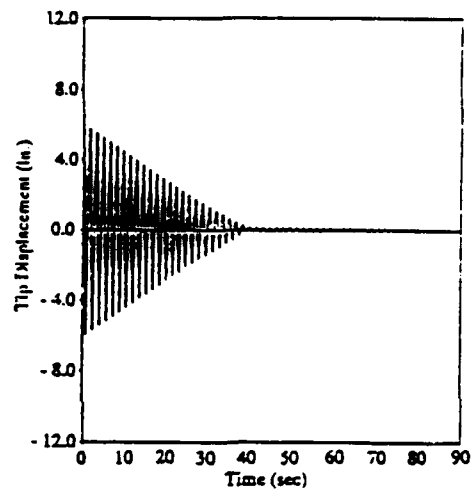


Fig. 5.9 Simulation of On-Off controller

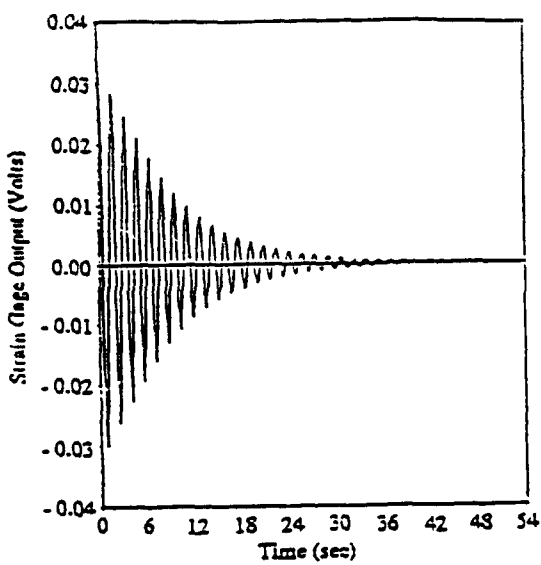


Fig. 5.10 Simulation of P-controller

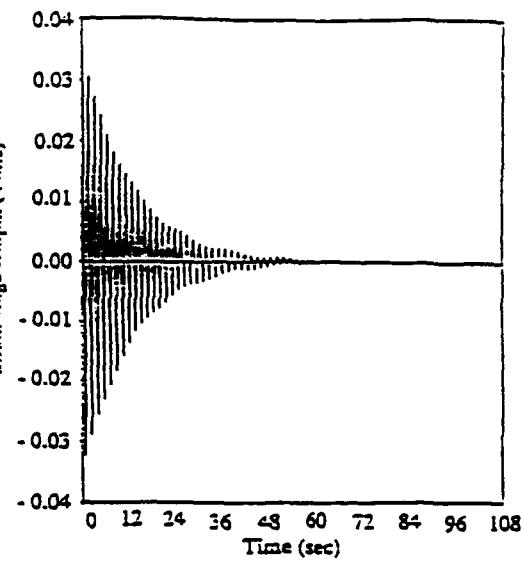


Fig. 5.11 Simulation of PI-controller

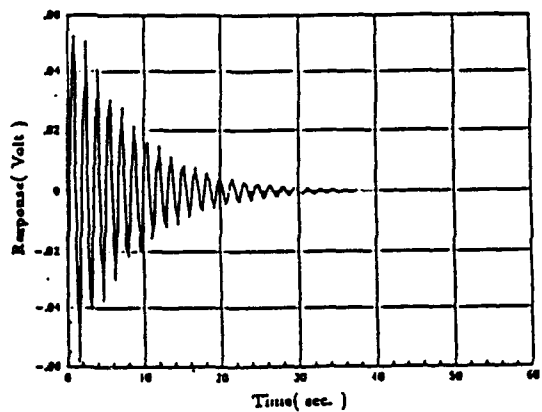


Fig. 5.12 Simulation of LQG/LTR controller

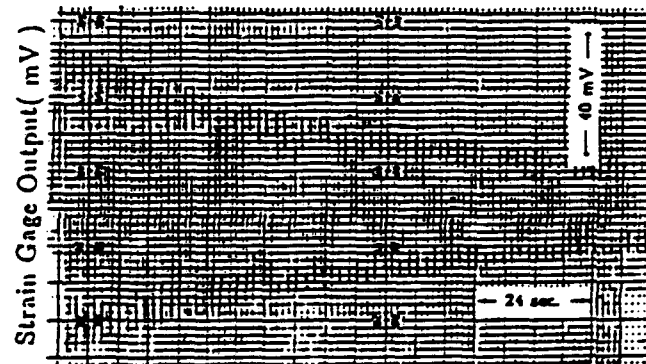


Fig. 5.13 Experimental Open-Loop response
($f_1=0.581$ Hz.)

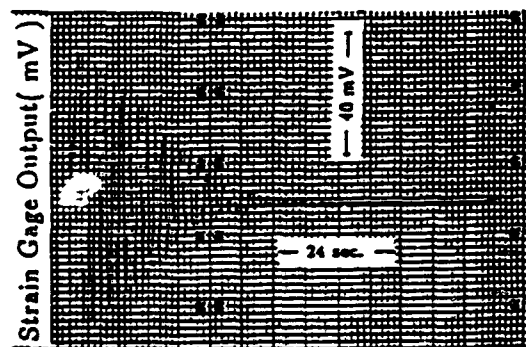


Fig. 5.14 Experimental response with On-Off controller



Fig. 5.15 Experimental response with
P-controller

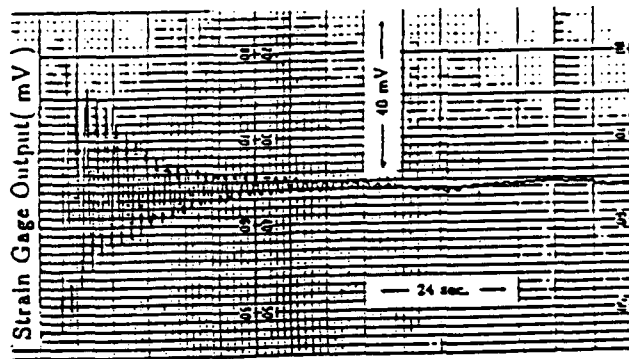


Fig. 5.16 Experimental response with PI-controller

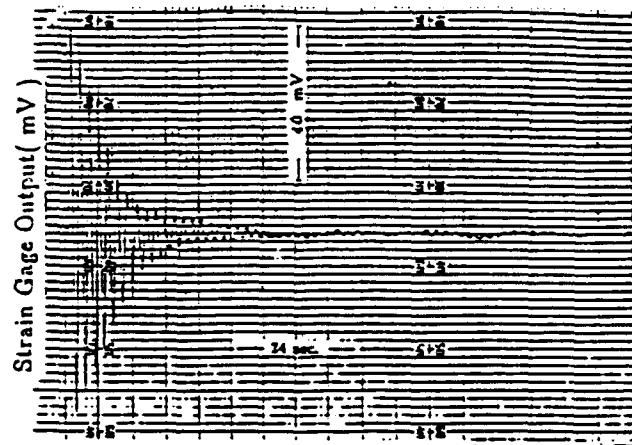


Fig. 5.17 Experimental response with LQG/LTR controller

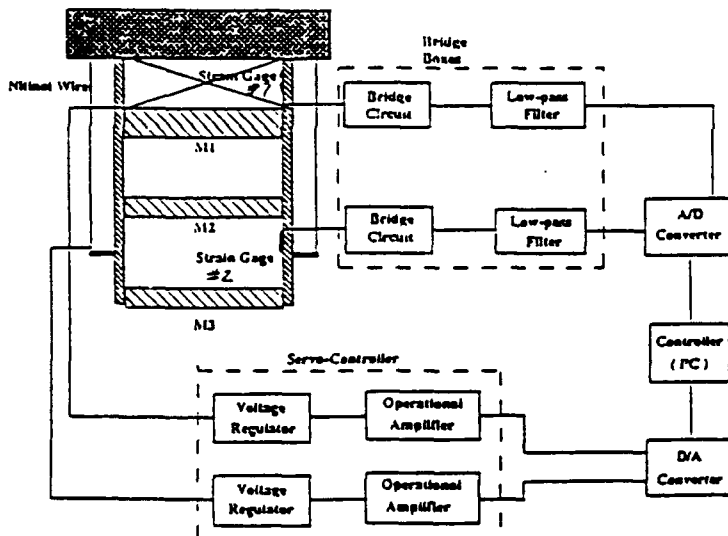


Fig. 5.18 Block diagram of three-mass system experimental set-up.

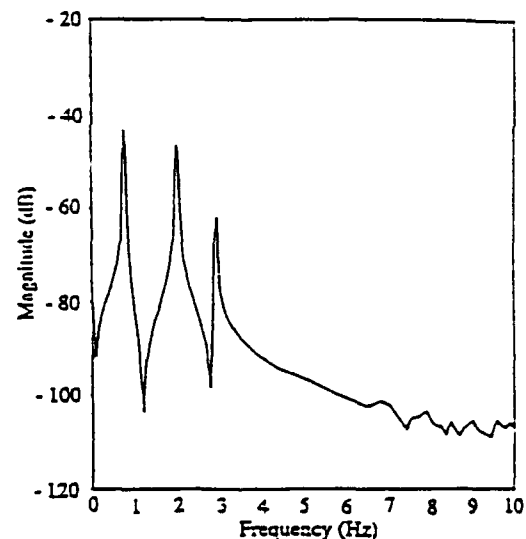


Fig. 5.19 Experimental frequency response of 3-mass system.

State-variable model

A finite element model with 15 nodes and 45 degrees of freedom was used to model the three-mass structure. Table 5.4 shows the first 10 computed natural frequencies. Only the first three, which involved displacements of the three masses, were within the bandwidth of the Nitinol actuators. Higher frequencies corresponded to spring resonances wherein the mass displacements were very

small, if not zero. Hence, only the first three modes were used in formulating the state-variable model. Figure 5.19 shows the frequency response of the actual structure, as determined by the impact-hammer method. The three peaks occur at 0.76, 2.00, and 2.92 Hz, respectively. The agreement between theory and experiment is good. The stiffening effects of the relatively-large static weight of the 3 masses were included in the finite element calculations.

Table 5.4. MSC/NASTRAN Output for Three-Mass System

MODE NO.	FREQUENCY (Hz)	GENERALIZED MASS (lb·s ² /in)	GENERALIZED STIFFNESS (lb/in)
1	0.7507	0.0871	1.9373
2	1.9318	0.1076	15.849
3	2.7957	0.0906	27.954
4	35.365	0.0010	51.315
5	35.450	0.0010	51.812
6	43.633	0.0008	57.358
7	43.782	0.0008	58.228
8	46.028	0.0007	60.470
9	46.213	0.0007	61.524
10	130.45	0.0936	62859.

The equations for the first three modes are given by (damping with $\zeta = 0.003$ has been added to the FE result)

$$\begin{bmatrix} 0.087 & 0. & 0. \\ 0. & 0.108 & 0. \\ 0. & 0. & 0.091 \end{bmatrix} \begin{Bmatrix} \ddot{q}_1 \\ \ddot{q}_2 \\ \ddot{q}_3 \end{Bmatrix} + \begin{bmatrix} 0.002 & 0. & 0. \\ 0. & 0.0051 & 0. \\ 0. & 0. & 0.0072 \end{bmatrix} \begin{Bmatrix} q_1 \\ q_2 \\ q_3 \end{Bmatrix} + \begin{bmatrix} 1.9 & 0. & 0. \\ 0. & 15.8 & 0. \\ 0. & 0. & 28. \end{bmatrix} \begin{Bmatrix} q_1 \\ q_2 \\ q_3 \end{Bmatrix} = \begin{bmatrix} -0.45 & -0.017 \\ -1.0 & 0.108 \\ 0.654 & 0.129 \end{bmatrix} \begin{Bmatrix} f_2 \\ m_5 \end{Bmatrix} \quad (12)$$

where q_i are the modal generalized coordinates, f_2 represents the effective transverse force from the 24" crisscrossed Nitinol wires, and m_5 the moment supplied by the longer 54" actuators (as in the case of cantilever beam).

Equation (12) can be put in state-variable form

$$\begin{aligned} \{\dot{x}\} &= [A_s] \{x\} + [B_s] \{u\} \\ \{y\} &= [C_s] \{x\} \end{aligned} \quad (13)$$

by defining a vector $\{x\}^T = [q_1 \ q_2 \ q_3 \ \dot{q}_1 \ \dot{q}_2 \ \dot{q}_3]$. The first of Eq. (13) then takes the form

$$\{\ddot{x}\} = \begin{bmatrix} 0 & I \\ -M^{-1}K & -M^{-1}C \end{bmatrix} \{x\} + \begin{bmatrix} 0 \\ M^{-1}B_s \end{bmatrix} \left\{ \begin{array}{l} f_2 \\ m_5 \end{array} \right\} \quad (14)$$

where M , C , K are matrices given in Eq. (12). The output $\{y\}$ in Eq. (13) are strain gage readings

$$\{y\}^T = [\epsilon_1 \ \epsilon_2 \ \epsilon_3 \ \dots] \quad (15)$$

To illustrate how these are computed, consider a case of 3 strain gages mounted on beam elements, as shown in Fig. 5.20.

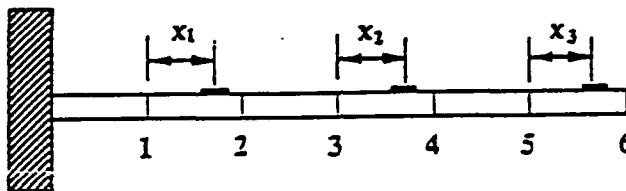


Fig. 5.20 Beam Elements with Three Strain Gages

For a beam bending element, the standard expression for the transverse deflection anywhere within the element is

$$y(x) = [N_1(x), N_2(x), N_3(x), N_4(x)] [y_1 \ \theta_1 \ y_2 \ \theta_2]^T \quad (16)$$

where $y_1, \theta_1, y_2, \theta_2$ are deflections and rotations at the left and right ends of the element, respectively, and $N_i(t)$ are standard beam-bending shape functions. The corresponding strain measured by a strain gage at $x = x_s$ is then

$$\epsilon(x_s) = -zy''(x_s) = -z[N_1''y_1 + N_2''\theta_1 + N_3''y_2 + N_4''\theta_2] \quad (17)$$

where $(\cdot)''$ denotes the second derivative of N_i evaluated at $x = x_s$, and z is the distance from the neutral axis of the beam element to its outer fibers where the gage is mounted.

Now, suppose that there are 3 gages, as indicated in Fig. 5.20. Then

$$\{y\} = \begin{Bmatrix} \epsilon_1 \\ \epsilon_2 \\ \epsilon_3 \end{Bmatrix} = - \begin{bmatrix} z_1 N''_1 & z_1 N''_2 & z_1 N''_3 & z_1 N''_4 & 0 & \dots & 0 \\ \vdots & \ddots & \ddots & \ddots & \ddots & \dots & \ddots \\ 0 & 0 & 0 & 0 & z_3 N''_1 & \dots & z_3 N''_4 \end{bmatrix} \begin{Bmatrix} \bar{y}_1 \\ 0_1 \\ \bar{y}_2 \\ 0_2 \\ \vdots \\ \bar{y}_6 \\ 0_6 \end{Bmatrix}, \quad (18)$$

or

$$\{y\} = -[zN''] \{\bar{y}\}. \quad (19)$$

But

$$\{\bar{y}\} = [T_a][q_1 q_2 q_3]^T \quad (20)$$

where $[T_a]$ is an abbreviated version (the upper left portion) of the modal matrix used to transform the original differential equations to modal coordinates. Also,

$$\begin{Bmatrix} q_1 \\ q_2 \\ q_3 \end{Bmatrix} = \begin{bmatrix} 1 & 0 & 0 & 0 & 0 & 0 \\ 0 & 1 & 0 & 0 & 0 & 0 \\ 0 & 0 & 1 & 0 & 0 & 0 \end{bmatrix} \begin{Bmatrix} x_1 \\ x_2 \\ x_3 \\ x_4 \\ x_5 \\ x_6 \end{Bmatrix} = [R] \{x\}. \quad (21)$$

Thus, the output equation is

$$\{y\} = [C_s] \{x\} \quad (22)$$

where

$$[C_s] = -[zN''] \quad (23)$$

Equations (14) and (23) constitute the state-variable model for the three-mass structure.

This state-variable model must be augmented by a model for the actuators. This can be formulated as follows. Corresponding to the transfer functions for the crisscrossed 24" wire and the lengthwise 54" wire, the actuator forces are represented by

$$\begin{Bmatrix} \dot{f}_s \\ \dot{f}_\ell \end{Bmatrix} = \begin{bmatrix} -0.2 & 0 \\ 0 & -0.2 \end{bmatrix} \begin{Bmatrix} f_s \\ f_\ell \end{Bmatrix} + \begin{bmatrix} 0.27 & 0 \\ 0 & 0.302 \end{bmatrix} \begin{Bmatrix} v_1 \\ v_2 \end{Bmatrix} \quad (24)$$

where f_s is the actuating force generated by voltage v_1 applied to the 24" wire, and f_ℓ is the force generated by voltage v_2 applied to the 54" wire. Equation (24) can be written as

$$\{\dot{f}_a\} = [A_a] \{f_a\} + [B_a] \{v\} \quad (25)$$

where $\{f_a\} = [f_s \ f_\ell]^T$ and $\{v\} = [v_1 \ v_2]^T$.

These actuator forces apply a transverse force f_2 and a moment m_5 to the 3-mass structure, where

$$\begin{Bmatrix} f_2 \\ m_5 \end{Bmatrix} = \begin{bmatrix} \sin\Theta & 0 \\ 0 & a \end{bmatrix} \begin{Bmatrix} f_s \\ f_\ell \end{Bmatrix} \quad (26)$$

and where Θ is the inclination to the vertical of the crossed 24" wires, and $a = 1.5"$ is the stand-off moment arm for the lengthwise 54" wire. Thus,

$$\begin{Bmatrix} f_2 \\ m_5 \end{Bmatrix} = [C_a] \{f_a\} \quad (27)$$

Equations (25) and (27) constitute the state-variable model for the actuator.

Finally, the augmented state-variable model including structural dynamics and actuator dynamics is

$$\begin{Bmatrix} \dot{x} \\ \dot{f}_a \end{Bmatrix} = \begin{bmatrix} A_s & B_s C_a \\ 0 & A_a \end{bmatrix} \begin{Bmatrix} x \\ f_a \end{Bmatrix} + \begin{Bmatrix} 0 \\ \dots \\ B_a \end{Bmatrix} \{v\} \quad (28)$$

$$\{y\} = [C_s : 0] \begin{Bmatrix} x \\ f_a \end{Bmatrix} \quad (29)$$

It is Eqs. (28) and (29) which are used in the simulation of the 3-mass system.

5.1.5 Comparison Between Simulation and Experiment

System verification

The step-response method was used to verify the mathematical model of Eqs. (28) and (29). A simple code in the C-language was written to send a constant command input voltage from the D/A port to the servo-amplifier. Figures 5.21 and 5.22 show the experimental results. Figure 5.21 shows the response of the first sensor to a 5-volt step-input to the force actuator (24" wire), and Fig. 5.22 shows the response of the second sensor when a step-input voltage of (-2) volts was applied to the moment actuator (54" wire). Figure 5.23 shows the corresponding simulation of the experiment. The dotted line represents the output from the second sensor to a (-2) volt moment actuation and the solid line represents the first sensor output to a 5-volt force actuation. The comparison is fairly good.

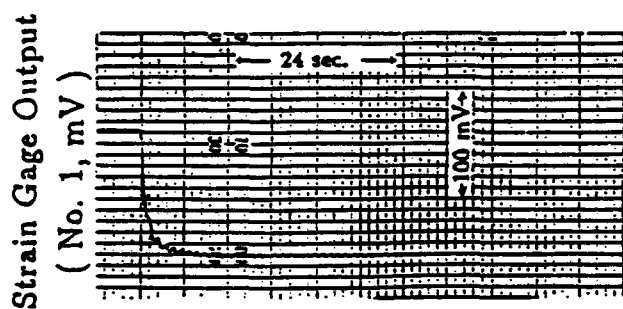


Fig. 5.21 Experimental step response of sensor No. 1.

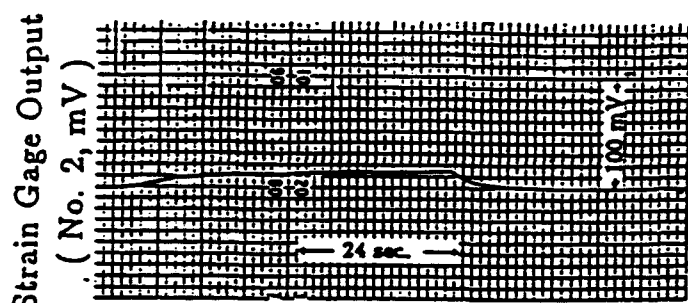


Fig. 5.22 Experimental step response of sensor No. 2.

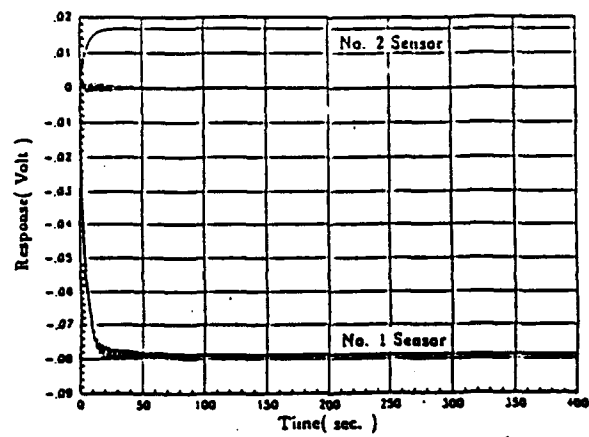


Fig. 5.23 Simulated step responses of 3-mass system.

5.2. Design of Robust Regulators with Arbitrary Eigenvalue Assignment

It is well known that given a system modeled by

$$\dot{x} = Ax + Bu \quad (30)$$

$$y = Cx \quad (31)$$

using the feedback control

$$u = -K_c x \quad (32)$$

yields the closed-loop regulator

$$\dot{x} = (A - BK_c)x = \Phi x \quad (33)$$

The feedback gain matrix, K_c , may be chosen to yield any desired set of eigenvalues. [102] In a MIMO system the choice of K_c is not unique and the available degrees of freedom can be used to choose eigenvectors as well as to specify the choice of eigenvalues. [102] It is also known that in order to make the performance of the resulting regulator as insensitive as possible to variations in model parameters, the eigenvectors should be chosen to be mutually orthogonal or as close to orthogonal as possible. [102,103]

Because the regulator for this particular situation is intended to provide active damping for the 2 input-2 output system, the closed-loop pole placements were chosen solely to improve (increase) the damping ratio of all lightly damped system poles without altering the undamped natural frequencies. Using the eighth order model discussed above, the performance of two different regulators has been investigated. The pole placement of these regulators is as shown in Table (5.5) below. This table gives the pole locations in the s-plane in order to aid the reader in visualizing the effect that the regulator has on the pole placement.

Table 5.5. Regulator Pole Locations

Model Poles	ω_n	ζ	For Damping Ratio $\zeta = 0.05$	For Damping Ratio $\zeta = 0.1$
$-0.160 \pm 20.109i$	20.109	0.0080	$-1.005 \pm 20.08i$	$-2.011 \pm 20.00i$
$-0.314 \pm 15.383i$	15.392	0.0204	$-0.773 \pm 15.44i$	$-1.539 \pm 15.315i$
$-0.061 \pm 5.987i$	5.9875	0.0102	$-0.279 \pm 5.98i$	$-0.599 \pm 5.957i$

Table 5.5. Regulator Pole Locations

Model Poles	ω_n	ζ	For Damping Ratio $\zeta = 0.05$	For Damping Ratio $\zeta = 0.1$
-1.5038	-	-	-1.5038	-1.5038
-6.8838	-	-	-6.8838	-6.8838

From Table (5.5) it can be seen that the design goal for the regulator is to keep all s-plane complex poles at the same ω_n , i.e., at the same distance from the origin as in the open-loop system. The closed-loop system will then move each complex pole pair on a circle of constant ω_n to a point where the damping ratio is increased to the chosen value.

5.2.1. Implementation

The regulators were implemented using a digital control with a standard predictor type observer. [105] A sampling frequency of 20 Hz (sampling time of 50 ms) was chosen so that the highest natural frequency of the model poles was less than one half the sampling frequency. Using this sampling frequency, a discrete time model of the cascaded combination of the continuous eighth order model driven by a D/A converter was developed. [104] Thus the model used to develop the controller is of the form

$$x(k+1) = Fx(k) + Gu(k) \quad (34)$$

$$y(k) = Cx(k) + Du(k) \quad (35)$$

The controller equations then will have the form

$$\hat{x}(k+1) = (F - GK_c - K_f C) \hat{x}(k) + K_f y(k) \quad (36)$$

$$u(k) = -K_c \hat{x}(k) \quad (37)$$

To implement the pole-placement controllers, the desired s-plane closed-loop pole locations listed in Table (5.5) were mapped into the z-plane using the mapping $z=e^{sT}$ where the values of s are the eight pole locations listed in the appropriate columns of Table (5.6) and T is the sampling time. The desired z-plane

locations listed in Table (5.6) were obtained in this manner.

Table 5.6. Desired z-Plane Locations for Closed-loop Poles

For Damping Ratio $\zeta = 0.05$		For Damping Ratio $\zeta = 0.01$	
s-Plane	z-Plane	s-Plane	z-Plane
$-1.005 \pm 20.08i$	$0.5106 \pm 0.8023i$	$-2.011 \pm 20.000i$	$0.4886 \pm 0.7610i$
$-0.773 \pm 15.44i$	$0.6894 \pm 0.6711i$	$-1.539 \pm 15.315i$	$0.6675 \pm 0.6417i$
$-0.279 \pm 5.98i$	$0.9423 \pm 0.2905i$	$-0.599 \pm 5.957i$	$0.9278 \pm 0.2848i$
-1.5038	0.9276	-1.5038	0.9276
-6.8838	0.7088	-6.8838	0.7088

Using the desired z-plane locations and the discrete time model for $T= 0.05$ seconds given Eqs. (34) and (35), the feedback gains for the two regulators were calculated using the Kautsky algorithm. [103,104] The results appear in Table (5.7).

Table 5.7. Regulator Feedback Matrices

K_D (for $\zeta = 0.05$)	4.644	-3.508	-1.181	-10.256	5.979	-6.680	1.595	-2.921
	9.053	41.255	44.088	-4.732	1.484	5.852	-10.797	-29.826
L_D^T (for $\zeta = 0.05$)	-10.750	6.591	-1.755	2.441	14.907	-52.969	-2.432	3.900
	-20.034	6.757	-4.734	-12.069	8.974	0.090	4.512	0.835
K_D (for $\zeta = 0.1$)	3.682	-1.499	-5.476	-31.487	10.770	-3.040	11.898	-26.038
	0.077	-10.057	-0.948	1.122	12.412	15.811	-4.810	-17.980
L_D^T (for $\zeta = 0.1$)	-10.759	6.591	-1.755	2.441	14.907	-0.530	-2.432	3.900
	-20.034	6.757	-4.734	-12.068	8.974	0.090	4.512	0.834
K_D (for LQG/ LTR)	12.328	15.120	6.256	3.580	9.530	-0.118	-0.547	-12.674
	24.199	8.033	-1.413	0.167	13.777	-6.314	-3.118	-43.107
L_D^T (for LQG/ LTR)	0.152	0.050	-0.044	-0.699	0.383	-0.161	-0.288	0.152
	-0.771	0.020	-0.371	-0.770	0.198	1.008	-0.130	-0.529

Two requirements were placed on the observer poles. First the real parts were chosen so that the time constants of the observer are short compared to those of the closed-loop regulator. Second, the observer Eq.

(36) must be open-loop stable. A choice of eight s-plane poles uniformly spaced on the interval [-20, -40] and then mapped into the z-plane using the mapping $z=e^{sT}$ satisfied these requirements for both regulators. Therefore, the same observer was used for both regulators. Table (5.8) contains the s-plane observer poles and the corresponding z-plane locations for $T= 0.05$ seconds.

Table 5.8. Observer Poles

s-plane	z-plane
-20.0000	0.3679
-22.8571	0.3189
-25.7143	0.2765
-28.5714	0.2397
-31.4286	0.2077
-34.2857	0.1801
-37.1429	0.1561
-40.0000	0.1353

Because the calculation of the observer gain, K_f , is a dual to the calculation of the regulator gain, K_c , the same algorithm and software may be used for calculating K_f . [106] The observer gains for the two regulators are also listed in Table (5.7).

The feedback and observer gains used for the LQG/LTR are also included in Table (5.7).

The controllers were implemented using Quick Basic programming. To verify that the controllers were correctly implemented, a step response was calculated using Eq. (36). The step response of each implemented controller was measured and compared to the designed controller step response. The step response of the eigenvalue assignment controller for $\zeta = 0.05$ and the step response for the LQG/LTR controller appears in Fig. (5.29). In each instance, the measured response was identical to the response predicted by simulation.

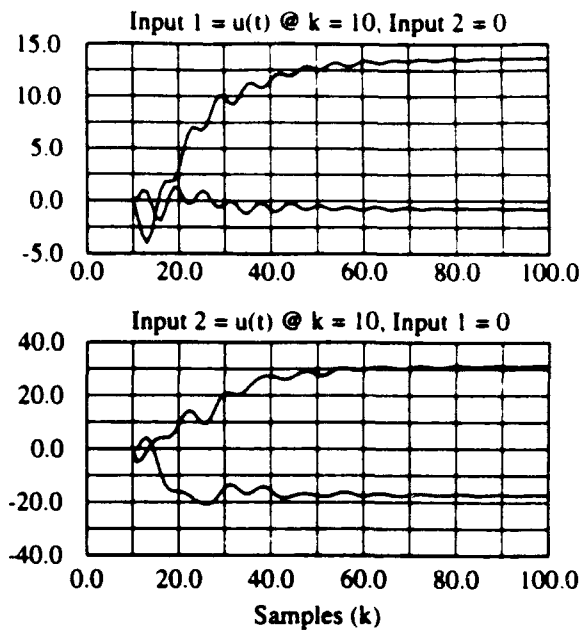
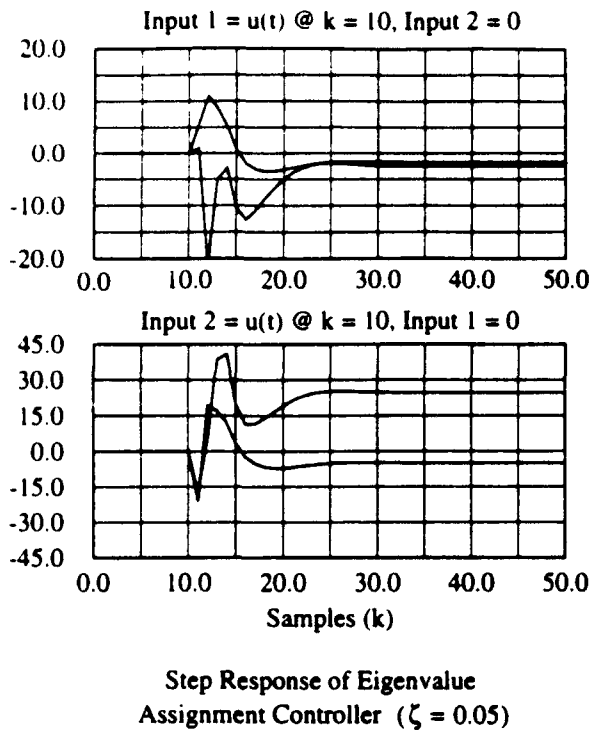


Figure 5.24 Controller Step Responses

5.2.2. Results

Figure 5.25 shows the open-loop time response of the test article when initially excited in the first mode. The natural damping is approximately 0.3%. Closing the loop with the Robust Regulator designed in Section 5.2 with $\zeta = 0.05$ yielded the results shown in Fig. 5.31. The envelope of the open-loop response is also shown for comparison. The controller performed as was predicted in simulation. The effect of the dead-band can be seen when the control output no longer drives the wires. At this point, the oscillations decay at the

natural damping rate.

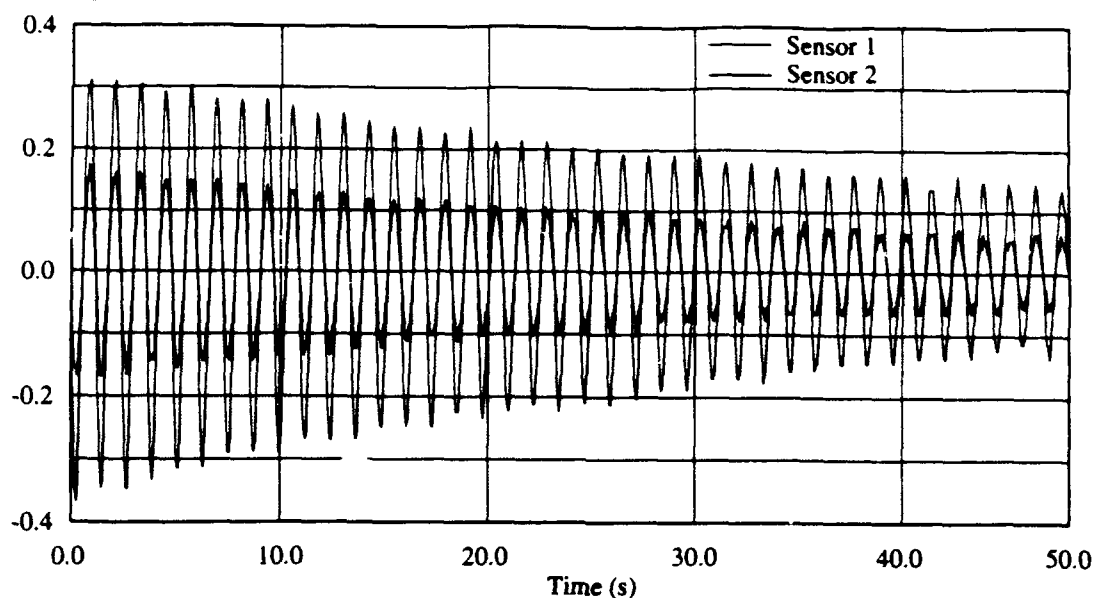


Figure 5.25 Open-Loop Time Response

Sensor 1

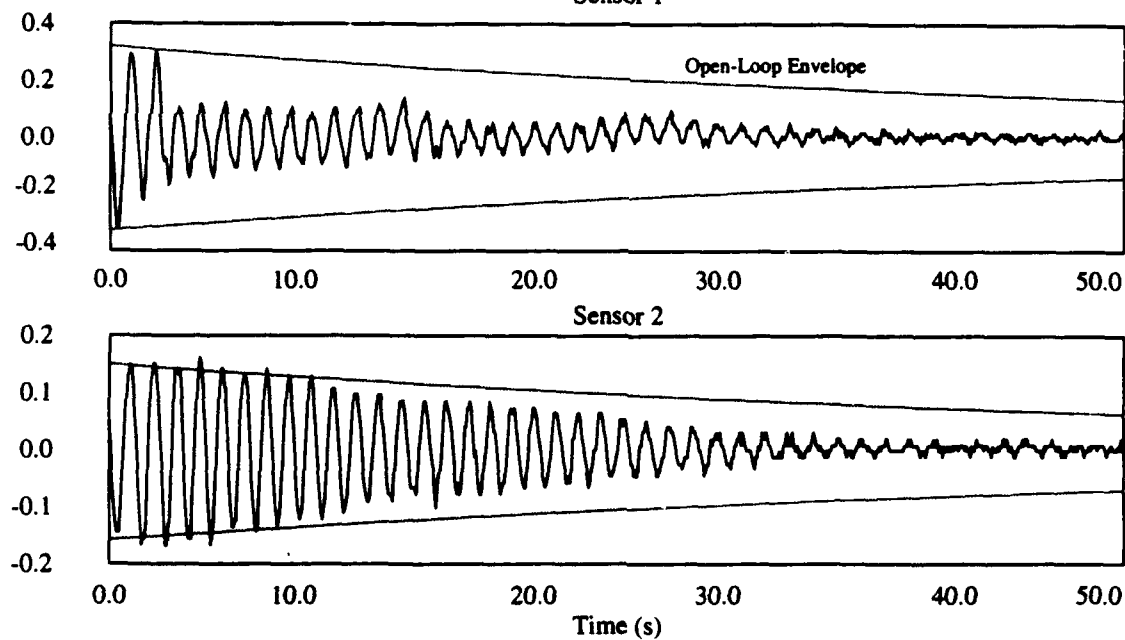


Figure 5.26 Time Response with Eigenvalue Assignment Controller

To test the "robustness" of the controller, an additional 2.25# was added to the bottom mass and 1.25# to the middle mass. The new open-loop time response is plotted in Fig. 5.27. The additional mass resulted in decreased damping and an increased modal frequencies. As can be seen in Fig. 5.28, the performance of the

controller in damping the response is virtually unchanged.

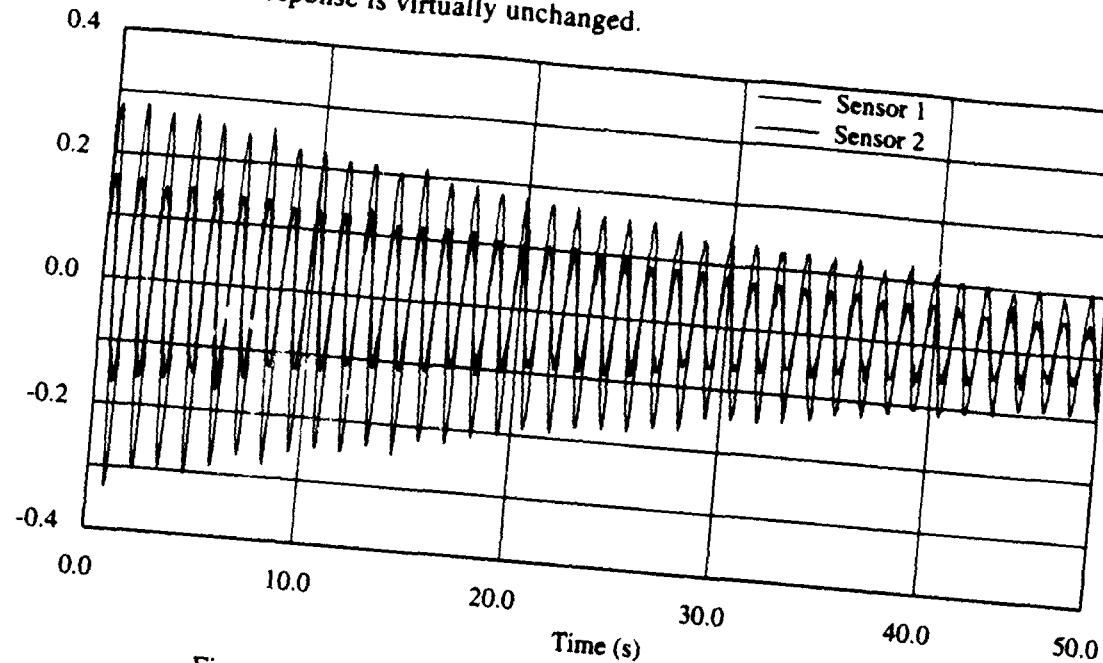


Figure 5.27 Open-Loop Time Response (Robustness Test)

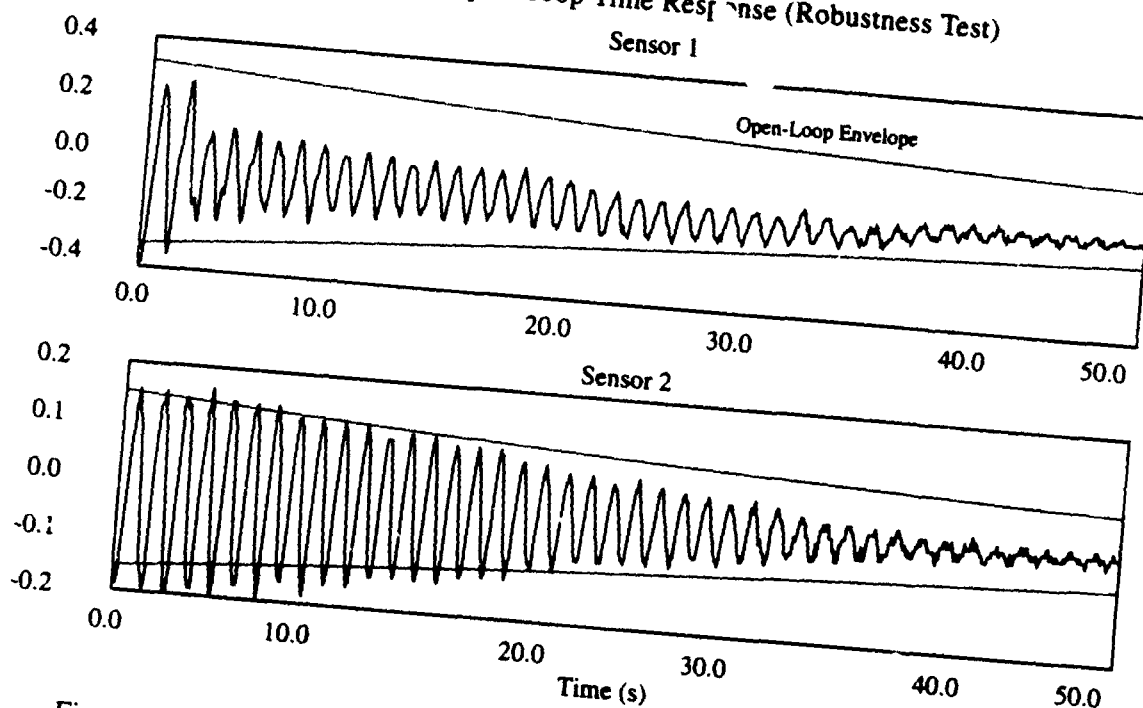


Figure 5.28 Time Response with Eigenvalue Assignment Controller (Robustness Test)

5.3. Robust Controllers

After designing conventional controllers for the cantilever beam and three mass structures, robust controllers were designed to quell the vibrations in the test articles. We needed a controller algorithm that would

be insensitive to parameter uncertainty, linearized model error and sensor noise. To overcome these difficulties, a robust controller was designed using the linear quadratic Gaussian loop transfer recovery (LQG/LTR) methodology. The block diagram of the controller and plant is shown in Fig. 5.29.

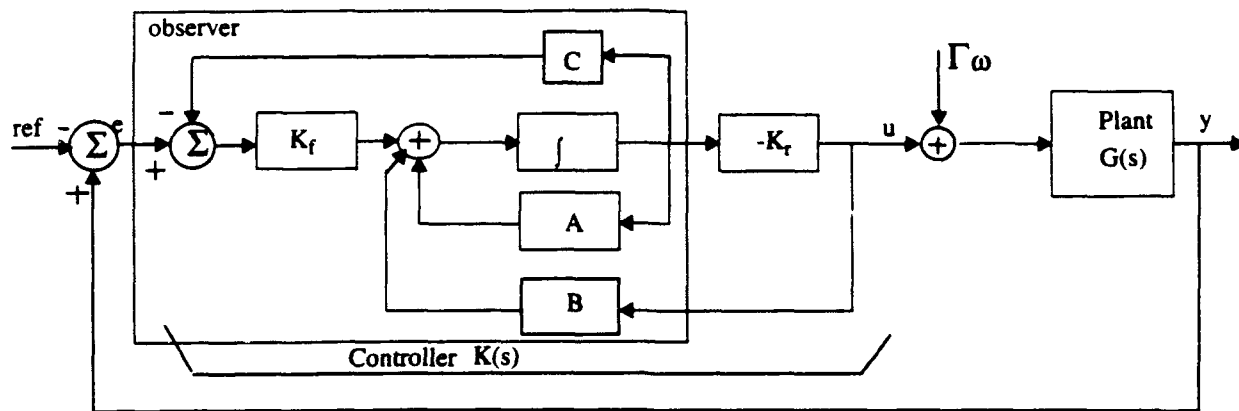


Figure 5.29 Controller and Plant Block Diagram

5.3.1. Nominal LQG/LTR Design Method

The fundamental equations needed in the LQG/LTR design are given in Eqs. (38 - 43). These equations are developed in Doyle [106], Maciejowski [109], and Ridgely [110].

$$\dot{x}(t) = Ax(t) + Bu(t) + \Gamma w(t) \quad (38)$$

$$J = \lim_{T \rightarrow \infty} E \left\{ \int_0^T (x^T(t) Q_c x(t) + u^T(t) R_c u(t)) dt \right\} \quad (39)$$

$$0 = AP_f + P_f A^T + \Gamma \Gamma^T - \frac{1}{\mu} P_f C^T C P_f \quad (40)$$

$$K_f = \frac{1}{\mu} P_f C^T$$

$$0 = A^T P_c + P_c A - P_c B R_c^{-1} B^T P_c + Q_c \quad (41)$$

$$K_c = R_c^{-1} B^T P_c$$

where

$$Q_c = C^T C + q^2 C^T C \quad (42)$$

The basic design methodology is to determine K_f so that you obtain a certain open-loop transfer function shape and then to determine K_c so that you recover the robustness stability properties desired. The loop gain is varied using μ . The loop shape is changed using Γ . Finally, the amount of stability recovered is determined by the parameter q^2 . After K_f and K_c are obtained, the controller is then implemented using the state equations in Eq. (43).

$$\begin{aligned} \dot{X}_c &= (A - BK_c - K_f C) X_c + K_f e \\ U_c &= -K_c X_c \end{aligned} \quad (43)$$

An initial controller design was performed without restricting the control effort. The parameters for this design were $\mu = 0.2$, $\Gamma = B$ and $q^2 = 1 \times 10^5$. Figure (5.30) shows the amount of recovery achieved with this controller. Notice that we do not have perfect recovery around the frequency of interest (3.6 rad/sec). Although from Fig (5.31), we see that we are already saturating the actuators (control effort $> 1.2V$). The saturation problem is caused by the q^2 parameter. As q^2 is increased, the accuracy of the loop transfer recovery increases (i.e. controller performance); however, the magnitude of the control force $u(t)$ also increases. Because of limited control effort when using NiTiNOL wire, the saturation effect will always be a major system constraint.

In order to initially overcome this constraint, we decided to reduce the amount of recovery until we acquired a controller that would no longer saturate the actuators. The parameters for this design were $\mu = 0.2$, $\Gamma = B$ and $q^2 = 50$. The maximum control effort produced for this controller was 0.9V. However, Fig (5.30) shows that the amount of recovery for this design was extremely low which translates into poor system performance. Therefore, we needed to develop a controller that would not only not saturate our actuators but would also be insensitive to system uncertainties. We turned to a modified structure for the LQG/LTR controller developed by Prakash [111] which quickens the loop transfer recovery process.

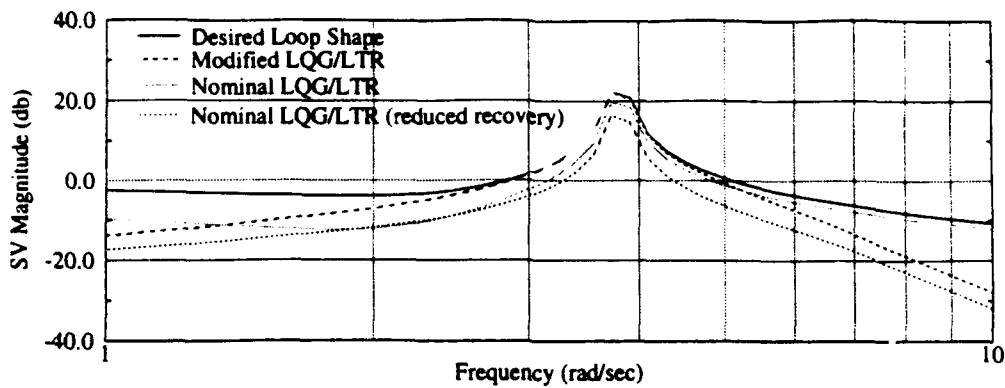


Figure 5.30 Comparison of Loop Transfer Recovery

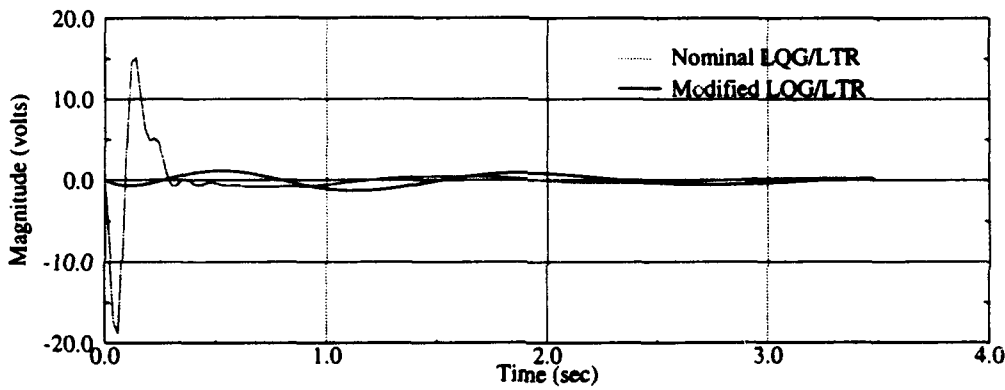


Figure 5.31 Comparison of Control Effort

5.3.2. Modified LQG/LTR Method

Before we show the results obtained using the modified LQG/LTR structure, we will first motivate the physical insight behind the structure. In order to develop the insight behind the modified structure, we will first demonstrate why observer based LQG/LTR methodologies result in high gain controllers. The first main objective behind LQG/LTR controllers is given a system configuration shown in Fig. 5.32 design a controller $K(s)$ such that $P(jw)K(jw)$ is approximately equal to $L(jw)$ which is the desired open-loop transfer function. Therefore, the error transfer function between the desired open-loop transfer function and the actual open-loop transfer function is $E_0(s) = L(s) - P(s)K_0(s)$ where $K_0(s)$ is the transfer function of an observer based controller. From Eq. (43), the transfer function for the standard LQG/LTR structure is.

$$K_0 = K_f (\Phi^{-1} + K_f C + B K_f)^{-1} K_f \quad (44)$$

where $\Phi = (sI - A)^{-1}$

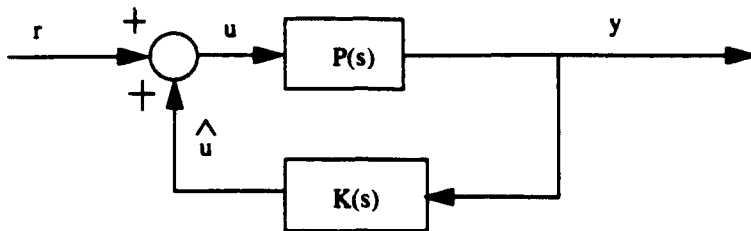


Figure 5.32 Basic LQG/LTR System Configuration

The exact LQG/LTR design procedure depends on whether the closed-loop system is broken at the input or output of the plant. We will concentrate on the LQG/LTR algorithm if the loop is broken at the output of the plant. For a system with the loop broken at the output of the plant, the desired open-loop transfer function becomes.

$$L(s) = C\Phi K_f \quad (45)$$

Given the plant transfer function, the desired open-loop transfer function, and the controller transfer function, Prakash showed that the error transfer function becomes.

$$E_0(s) = (I + C\Phi(s)K_f)(I + N(s))^{-1}N(s) \quad (46)$$

where $N(s) = C(\Phi^{-1} + BK_c)^{-1}K_f$

The desired goal of the LQG/LTR design is for the error transfer function to equal zero for all frequencies; however, Prakash showed that this can only be true if $N(s) = 0$ for all frequencies. Since this cannot be achieved, the size of $N(jw)$ must be small in some sense for all w of interest. In order to achieve this, let K_f be parameterized in terms of a parameter σ such that, $N(s) = C(\Phi^{-1} + BK_c(\sigma))^{-1}K_f \rightarrow 0$ pointwise in s as $\sigma \rightarrow 0$. However, we want the state feedback and observer gains to be independent of one another; therefore this requires that $C(\Phi^{-1} + BK_c(\sigma))^{-1} \rightarrow 0$ pointwise in s as $\sigma \rightarrow 0$. To satisfy this requirement, the observer

based LQG/LTR approaches require that $\|K_c(\sigma)\| \rightarrow \infty$ as $\sigma \rightarrow \infty$. Thus the standard LQG/LTR algorithm is a high gain approach. Since there is a trade-off between robustness properties and the size of the feedback gain and the size of the feedback gain is a major system constraint, we need to use an algorithm which provides as low a gain as possible.

By allowing ourselves to design a LQG/LTR controller that is not observer based the link from the estimated states to the observer can be eliminated because the effect of the above link on the output of the observer based controller vanishes asymptotically as $\sigma \rightarrow \infty$. The structure for this new LQG/LTR controller is given in Fig (5) with the appropriate link missing from the standard LQG/LTR structure.

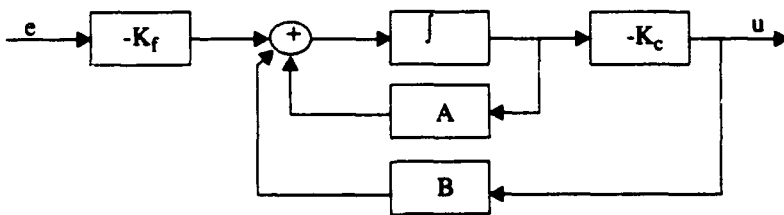


Figure 5.33 Block Diagram of Modified LQG/LTR Structure

The feedback gain and estimator gain vectors are determined exactly as in the standard LQG/LTR approach, the only difference is the structure of the controller after the gains are determined. The state equations for the modified LQG/LTR structure are

$$\begin{aligned}\dot{X} &= (A - BK_c) X_c + K_f e \\ U &= -K_c X_c\end{aligned}\tag{47}$$

Since this controller is no longer observer based then the separation principle is not valid. Prakash however has proven that the design objectives of the closed-loop stability and recovering the target loop shape can both be simultaneously achieved.

Finally to demonstrate that the new structure does quicken the loop transfer recovery process, we need to return to the error transfer function. Prakash showed that the error transfer function for the modified structure is

$$E_0 = N(s)\tag{48}$$

Also assuming that the singular values of $N(s)$ are small over a frequency range of interest and that the

singular values of $C\Phi K$, are large for the frequency range of interest (i.e. good controller performance), then comparing Eqs. (46) and (48) shows that as q^2 is increased, Eq. (48) becomes small more quickly than Eq. (46) [111].

5.3.3. Results

Using this structure, we designed a new controller with $\mu = 0.2$, $\Gamma = B$, $q^2 = 100$. Figure 5.30 shows a comparison of the recovery between the two structures. Notice that the modified structure has a much greater recovery in the 3.6 rad/sec region. Figure 5.31 shows that the control effort for the modified structure is less than 1.2V. Therefore, the modified structure does not saturate the actuators.

The robustness of the controller was tested by allowing the tip mass to vary from 6.5 lbs to 9.0 lbs. Figure 5.34 shows the system performance for both the initial tip mass and the increased tip mass. Notice that the system damping is insensitive to the variation in the tip mass.

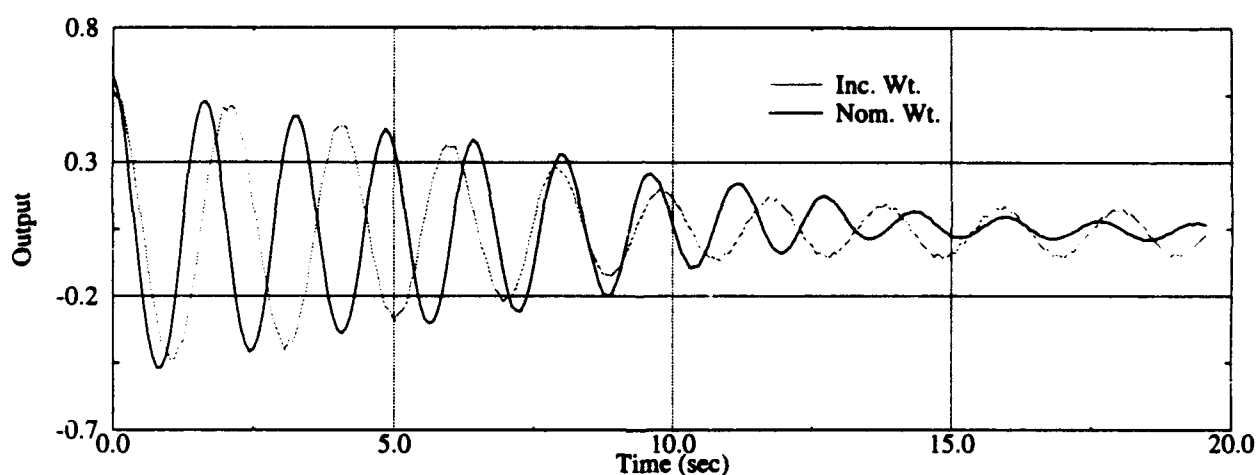


Figure 5.34 System Performance with the Modified Structure LQG/LTR Controller

After the modified LQG/LTR algorithm was applied to the SISO system, the algorithm was then applied to the three mass system (MIMO system). Again an initial comparison was performed between the standard LQG/LTR controller and the modified LQG/LTR controller. Figure 5.35 shows that the modified structure again produced a controller with much less control effort.

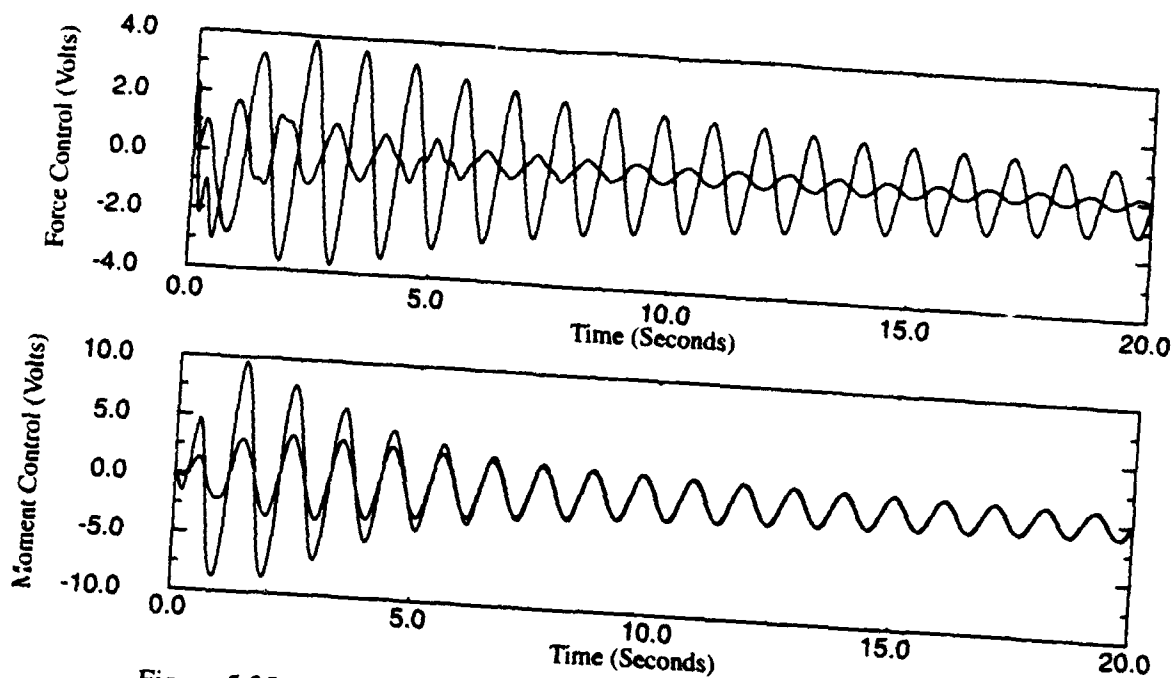


Figure 5.35 Comparison of Controller Effort for Three Mass Structure

In addition to the control effort comparison, Fig. 5.36 shows a time response to an initial condition for both the standard LQG/LTR structure and the modified LQG/LTR structure. The exponentially decaying envelopes in Fig. 5.36 shows the open-loop response. Notice that the modified structure is performing better for both sensors. The modified structure suppressed the vibrations to the dead band level in approximately 7.5 seconds; while, the standard structure suppressed the vibrations to the dead band level in approximately 12 seconds for sensor one. While for sensor two, the standard structure did not perform much better than open-loop and the modified structure suppressed the vibrations in approximately 5 seconds. This is expected because of the reduced recovery for the standard structure so that the actuators would not saturate.

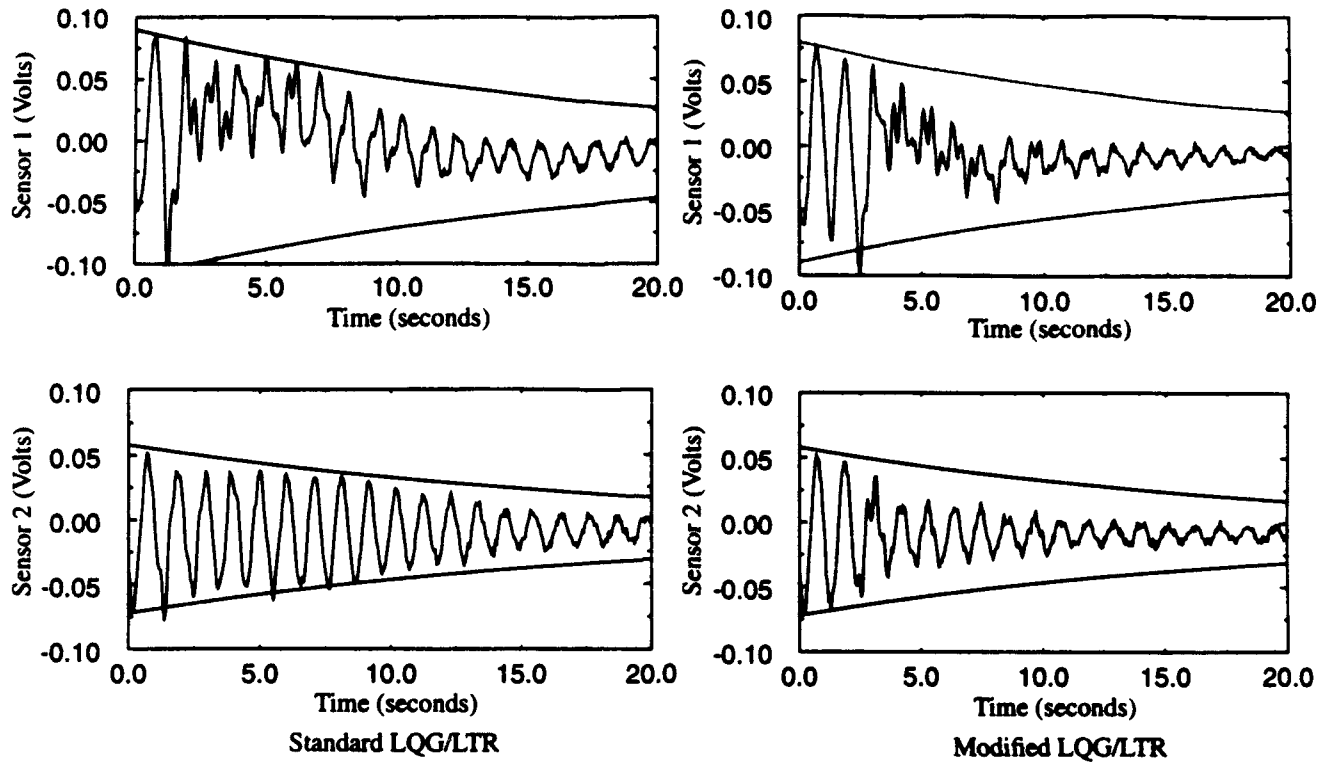


Figure 5.36 Initial Condition Responses for Three Mass System

The first robustness test was the addition of sensor noise. The sensor noise was a normally distributed noise signal with a variance of 400 and a mean of zero. Figure 5.37 contains the noise corrupted sensor values and the actual system response for both of the controllers. Even though the signal to noise ratio is poor, the modified LQG/LTR controller damped the oscillations to the dead band level in approximately 10 seconds, while the standard LQG/LTR controller was unstable.

Next, a parameter variation robustness test was conducted by adding mass to the test article. The second and third masses were increased by 1.4 lbs. Figure 5.38 contains the experimental system responses. With this parameter variation, both controllers were able to damped the oscillations to the dead band level in approximately 15 seconds.

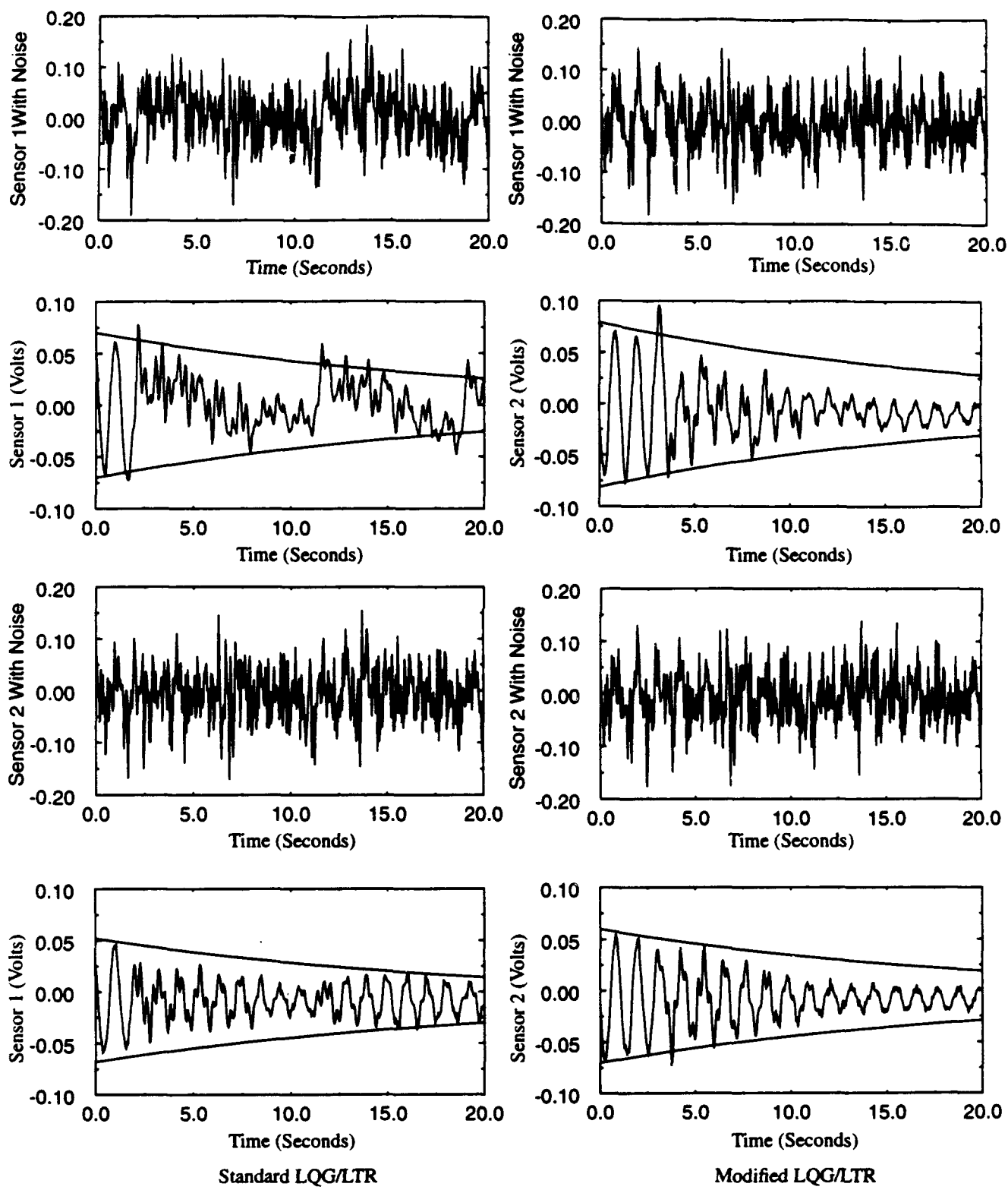


Figure 5.37 Controller Responses with Added Noise for the Three Mass System

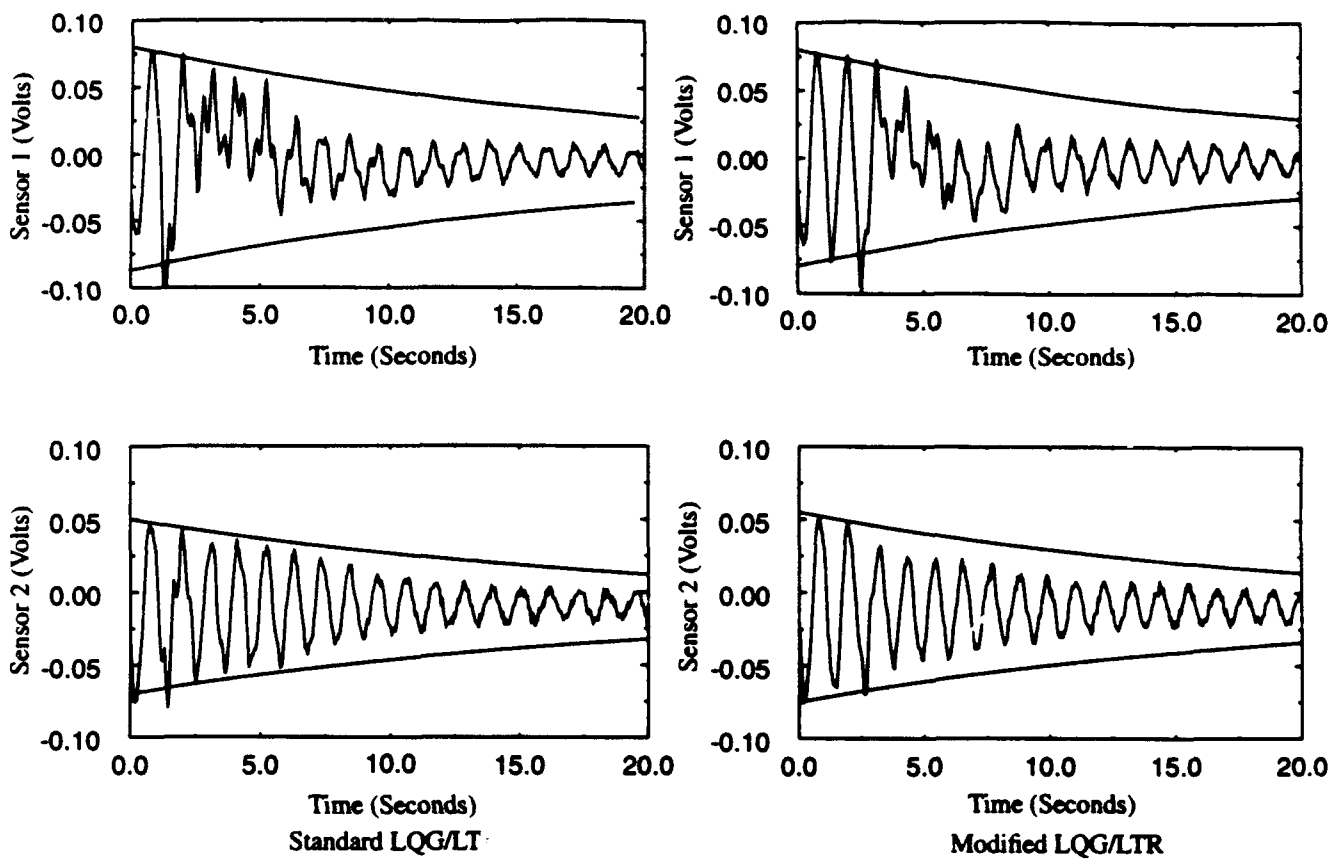


Figure 5.38 Controller Responses with Added Mass for the Three Mass Structure

5.4. Adaptive Controllers

Let a system be described by

$$\begin{aligned}\dot{x} &= f(x, u, p, \theta, t) \\ y &= h(x, p, \theta, t)\end{aligned}\tag{49}$$

where x is the system state, u is the system input, p and θ together make up the system parameters. The elements of the vector p are those parameters which are either unknown and constant or vary with time in an independent fashion and the elements of θ represent the parameters which are under the control of the designer. t is the time index. Adaptation then corresponds to the adjustment of the control parameter vector θ to compensate for the unknown parameter p .

If the functions f and h are linear mappings, the system can be represented by

$$\begin{aligned}\dot{x} &= A(p, \theta, t)x + B(p, \theta, t)u \\ y &= H(p, \theta, t)x\end{aligned}\tag{50}$$

where A , B and H are matrices of bounded, piecewise-continuous, time functions. Furthermore, if the system is time-invariant, it can be expressed in the form

$$\begin{aligned}\dot{x} &= A(p, \theta)x + B(p, \theta)u \\ y &= H(p, \theta)x\end{aligned}\tag{51}$$

In the class of systems governed by Eq. (51), the differential equations governing the plant are linear and the parameters are unknown but constant. The goal of the adaptive system is to find a constant parameter vector, θ^* using the measured signals of the system such that $\lim_{t \rightarrow \infty} \theta(t) = \theta^*$ and the system is modeled by

$$\begin{aligned}\dot{x} &= A(p, \theta^*, t)x + B(p, \theta^*, t)u \\ y &= H(p, \theta^*, t)x\end{aligned}\tag{52}$$

behaves in the desired fashion. Since θ is adjusted dynamically as a function of the states, the overall system becomes nonlinear. Equation can then be rewritten as

$$\begin{aligned}\dot{x} &= A(p, \theta, t)x + B(p, \theta, t)u \\ \dot{\theta} &= g(x, \theta, t)\end{aligned}\tag{53}$$

As time, t , goes to infinity, the behavior of the nonlinear system in Eq. (53) should approach that of the linear system in Eq. (52). It is this special class of nonlinear systems which shall be referred to as *adaptive systems* throughout this thesis.

5.4.1. Direct vs. Indirect Adaptive Control

For many years, there have basically been two distinct methods for finding the solution of the adaptive control problem. These are *direct* and *indirect control*. When the controller parameters, $\theta(k)$, are directly adjusted to reduce some norm of the output error between the reference model and the plant, this is called direct control or *implicit identification*. In indirect control, also referred to as *explicit identification*, the

parameters of the plant are estimated as the elements of a vector $\hat{p}(k)$ at each instant k and the parameter vector $\theta(k)$ of the controller is chosen assuming that $\hat{p}(k)$ represents the true value of the plant parameter vector, p . Figure 5.39 and Fig. 5.40 respectively show the direct and indirect model-reference adaptive control structures for a *Linear Time Invariant* (LTI) plant. It is important to note that in both cases efforts have to be made to probe the system to determine its behavior as control action is being taken based on the most recent information available. The input to the process is therefore used simultaneously for both identification and control purposes. However, not every estimation scheme followed by a suitable control action will result in optimal or even stable behavior of the overall system. Therefore, considerable care must be taken in blending estimation and control schemes to achieve the desired objective [107].

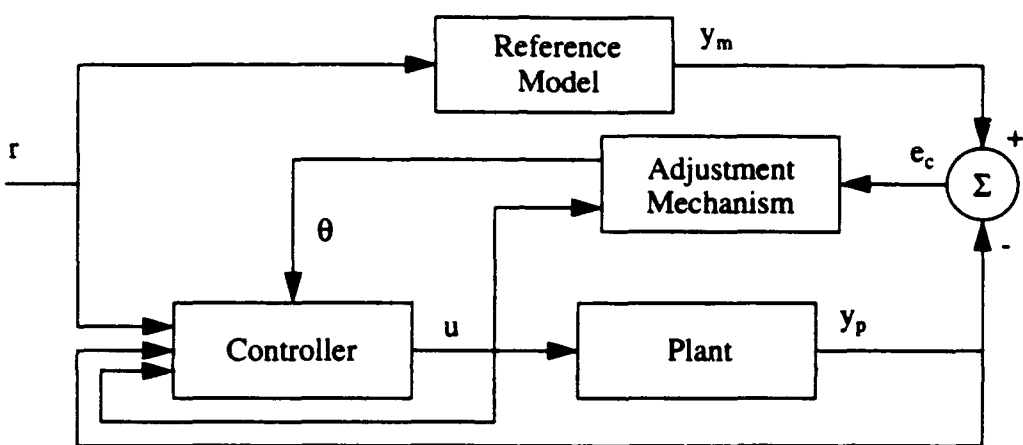


Figure 5.39 Direct Model-Reference Adaptive Control Structure

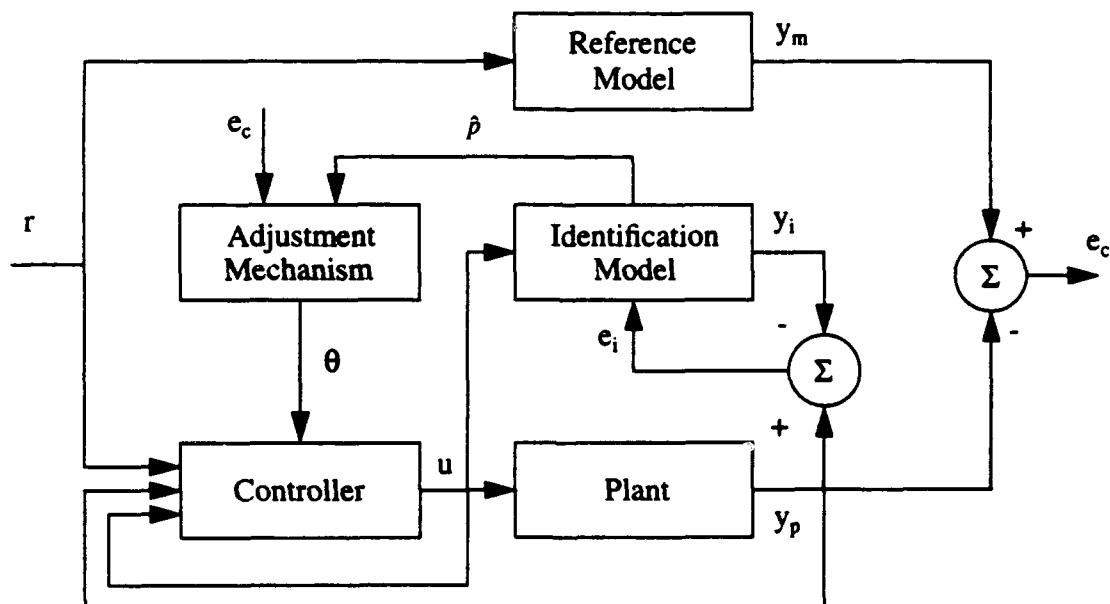


Figure 5.40 Indirect Model-Reference Adaptive Control Structure

5.4.2. Model-Reference Adaptive Systems

The *Model-Reference Adaptive System* (MRAS) used previously to demonstrate the difference between direct and indirect control is one of the main adaptive control techniques. *Model-Reference Adaptive Control* (MRAC) was originally proposed to solve a problem in which the specifications are given in terms of a reference model that describes how the process output ideally should respond to the command signal. This is called the *model-following* problem. The model-following problem can be solved using pole-placement controller design when the plant parameters are completely specified with some given degree of certainty. However, when parts of the plant are unknown or contain a high degree of uncertainty, adaptive techniques can be used. Looking back at Fig. 5.39, a process is controlled via a regulator with input/output feedback loops. The desired performance of the plant is described as the output of a linear, or nonlinear, reference model, y_m , which gives the desired response to a command signal, r . The error, e_c , is then used by the outer loop to adjust the controller parameter vector, θ . In Fig. 5.40, the process is controlled in the same manner. Again, the desired performance is specified by the pair $\{r, y_m\}$. The plant parameter vector, $\hat{p}(k)$, is estimated and used with the error, e_c , by the outer loop to adjust the controller parameter vector, θ . In both cases the main problem is to determine an adjustment mechanism such that a stable system which drives the output error to zero is obtained. Note that the feedback control loop, consisting of the process and the regulator, is assumed to be faster than the outer loop, which adjusts the regulator parameters.

Another class of adaptive system is the *Self-Tuning Regulator* (STR) mentioned in the introduction. The STR is based on the ideas of separating the estimation of the unknown plant parameters from the design of the controller. The basic STR consists of a parameter estimator, a linear controller and a block which determines the control parameters from the estimated parameters. See Fig. 5.41. The unknown plant parameters are estimated on-line using a recursive estimation method. The estimated parameters are used in the control design equation as if they are true, i.e., the uncertainties of the estimates are not considered. Any control design method can be used, e.g., minimum variance, Linear Quadratic Gaussian/Loop Transfer Recovery (LQG/LTR), pole-placement, model-following, etc. The design method is chosen depending on the specifications of the closed-loop system. The STR was originally developed for sampled-data systems, but has since been extended to continuous-time. Hybrid algorithms have also been developed [108]. STRs have been studied extensively and enjoy a wide popularity due to their flexibility. They are easily understood and implemented [108]. STRs can be implemented as direct or indirect controls similar to the MRAS. In many cases, there is a direct correspondence between STRs and MRAS.

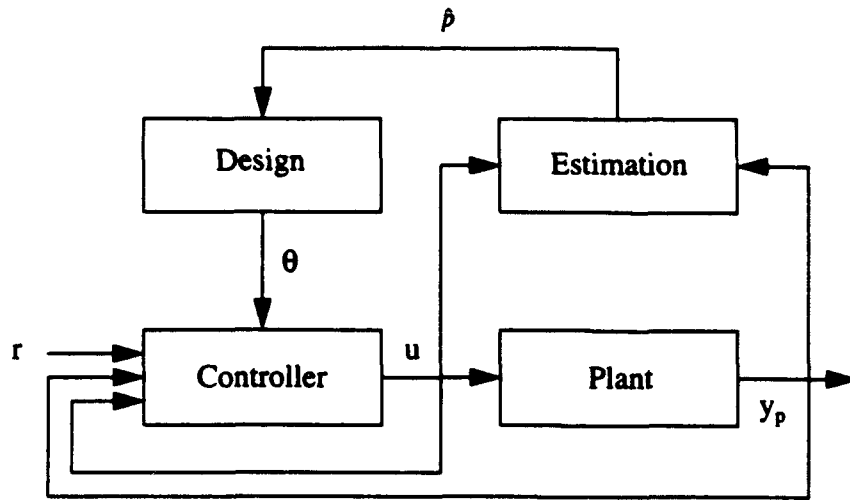


Figure 5.41 Self-Tuning Regulator Structure

5.4.3. Conventional Direct MRAC

The first controller implemented on the structure was the Direct MRAC shown in Fig. 5.42. This gives a basis for comparison between direct and indirect control. The Direct MRAC was implemented using the algorithm presented in Section II. (See Listing C.1 in See Appendix C.) Fig. 5.43 shows a plot of the open-loop response envelope, the desired response envelope, and the closed-loop response achieved. As can be seen, closed-loop system adapts to the reference-model response until deadband is reached (approximately 11 seconds), at which point adaptation is turned off. In Fig. 5.44, the control parameter vector $\theta(k)$ has stabilized after about 8 seconds and before deadband is reached.

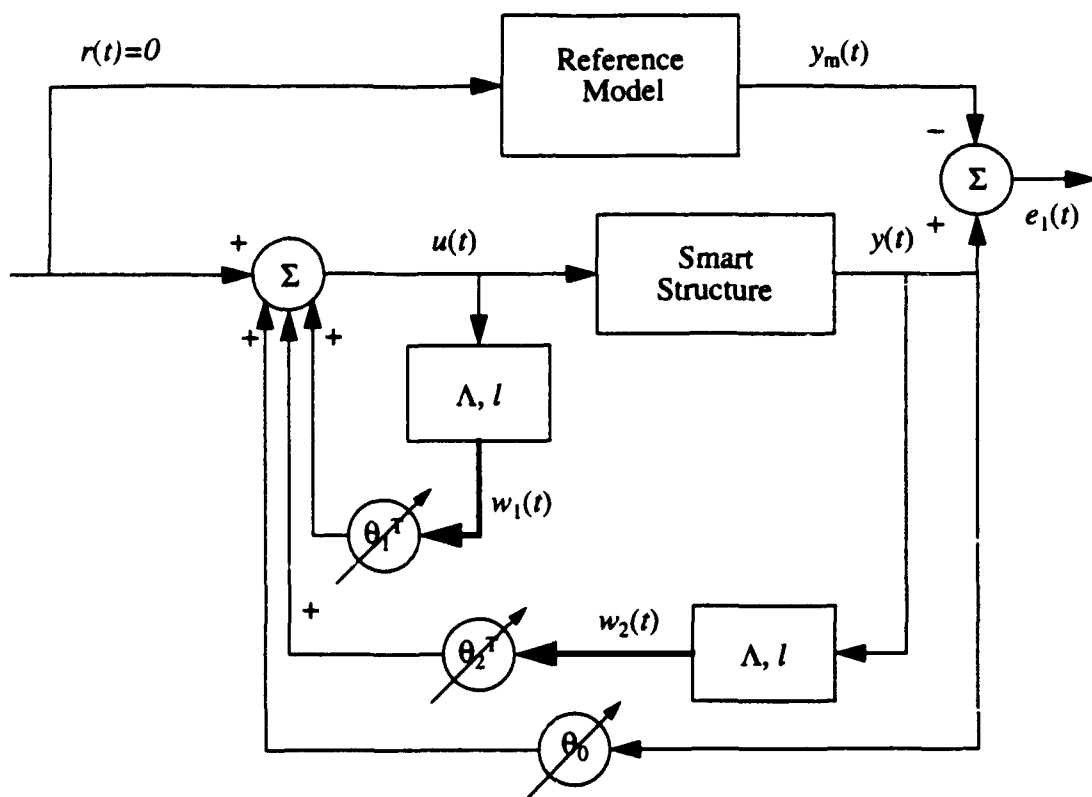


Figure 5.42 Direct MRAC Regulator for Smart Structure

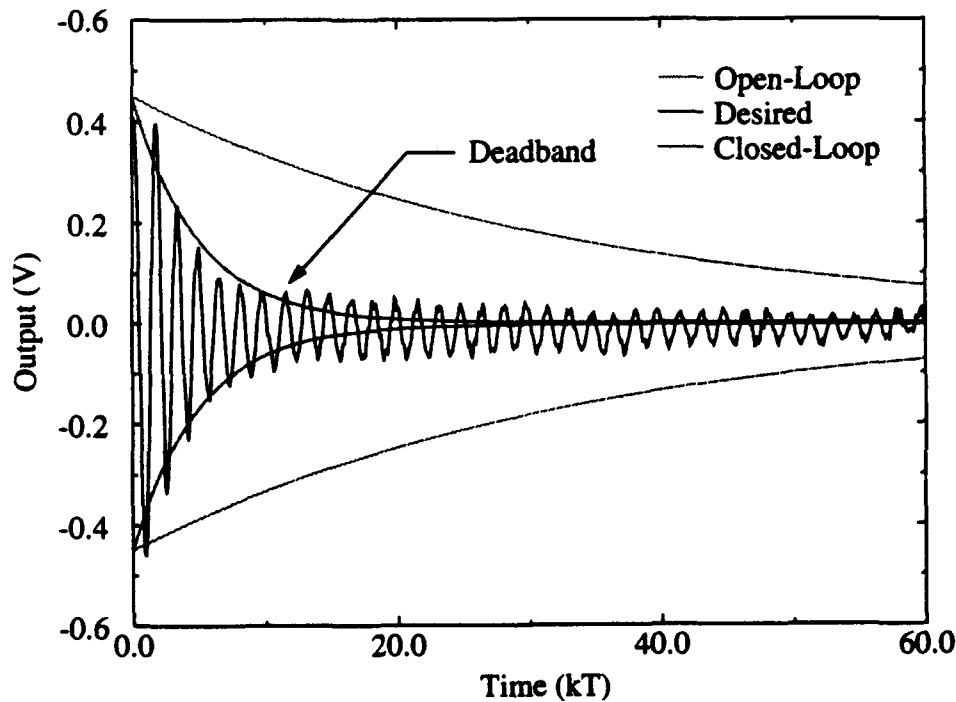


Figure 5.43 Open vs. Closed-Loop Response (Direct MRAC)

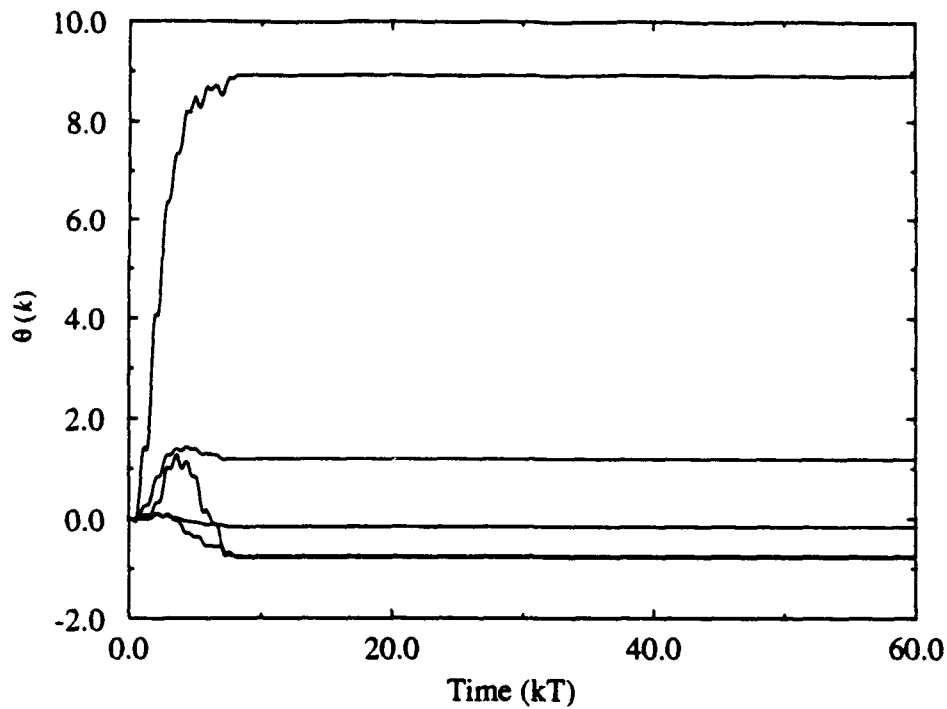


Figure 5.44 Evolution of Control Vector, $\theta(k)$ (Direct MRAC)

The final values of the controller parameters are given below

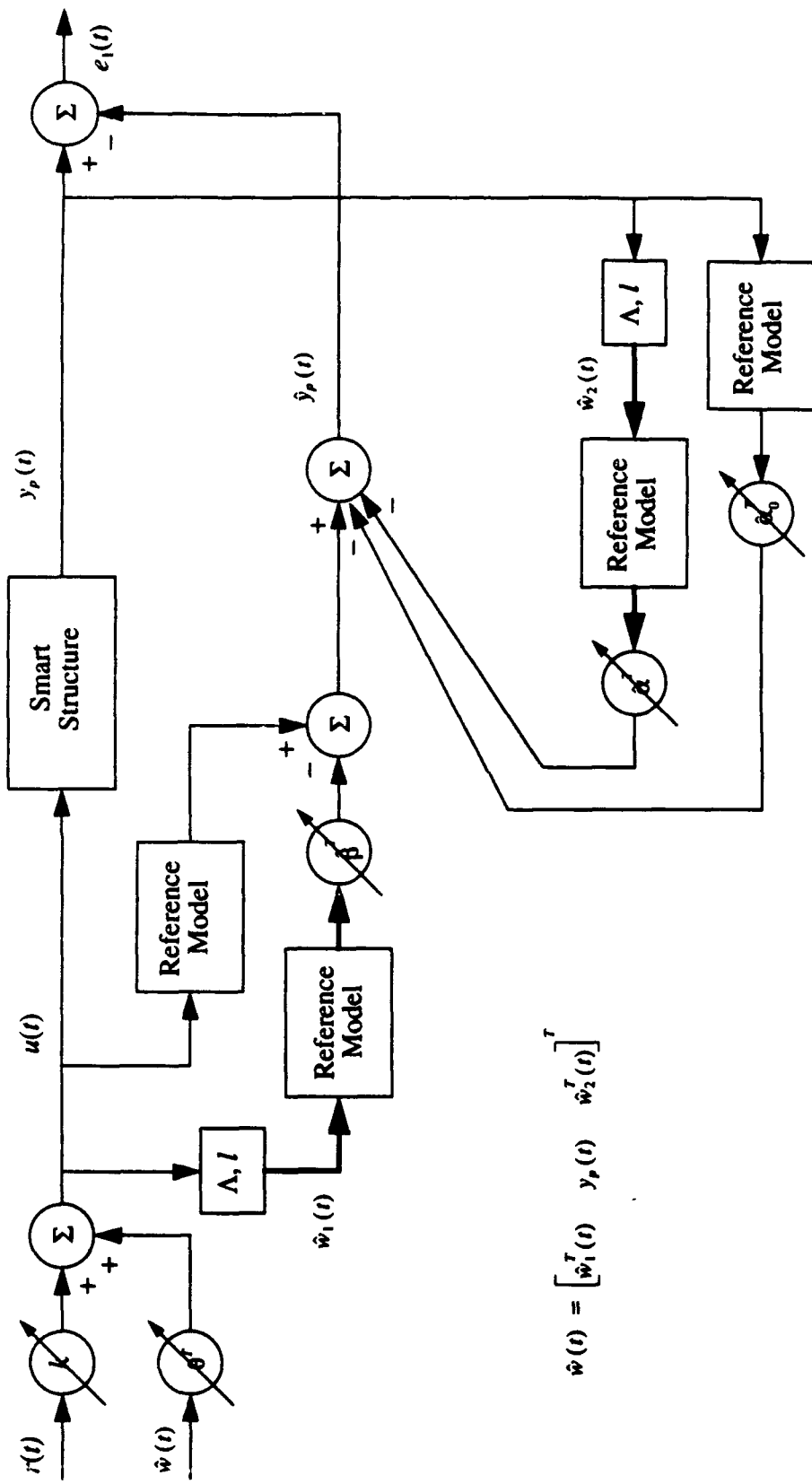
$\theta(k)$	Final Value
$\theta_1(k)$	$[-0.78069 \ 0.75716]^T$
$\theta_0(k)$	8.92846
$\theta_2(k)$	$[1.18814 \ -0.16468]^T$

1. Conventional Indirect MRAC

Next, an Indirect MRAC was implemented on the structure as shown in Fig. (5.42). Like the Direct MRAC, the Indirect MRAC was implemented using the algorithm presented in Section II. (See Listing C.2 in See Appendix C.) Figure (5.46) shows a plot of the open-loop response envelope, the desired response envelope, and the closed-loop response and Fig. (5.47) shows the time evolution of the control parameter vector $\theta(k)$. Again, the parameters stabilize after about 8 seconds with deadband reached by 11 seconds.

The final values of the controller parameters are given below

$\theta(k)$	Final Value
$\theta_1(k)$	$[0.98276 \ -1.01170]^T$
$\theta_0(k)$	9.36202
$\theta_2(k)$	$[1.61385 \ -0.14307]^T$



$$\hat{\psi}(t) = [\hat{\psi}_1^T(t) \quad y_p(t) \quad \hat{y}_p^T(t)]^T$$

Figure 5.45 Indirect MRAS Regulator for Smart Structure

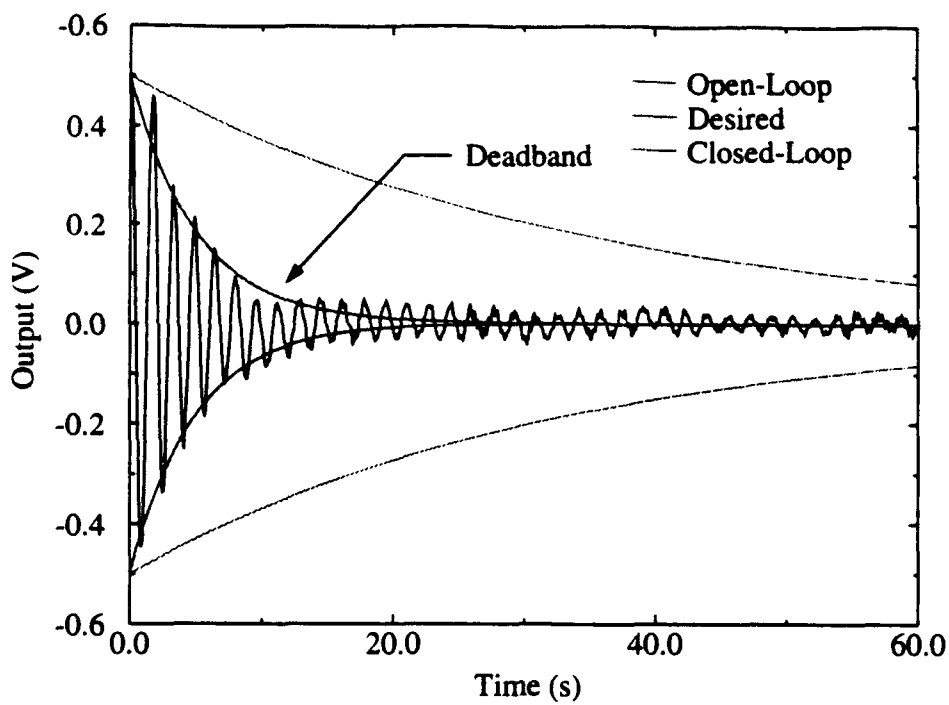


Figure 5.46 Open vs. Closed-Loop Response (Indirect MRAC)

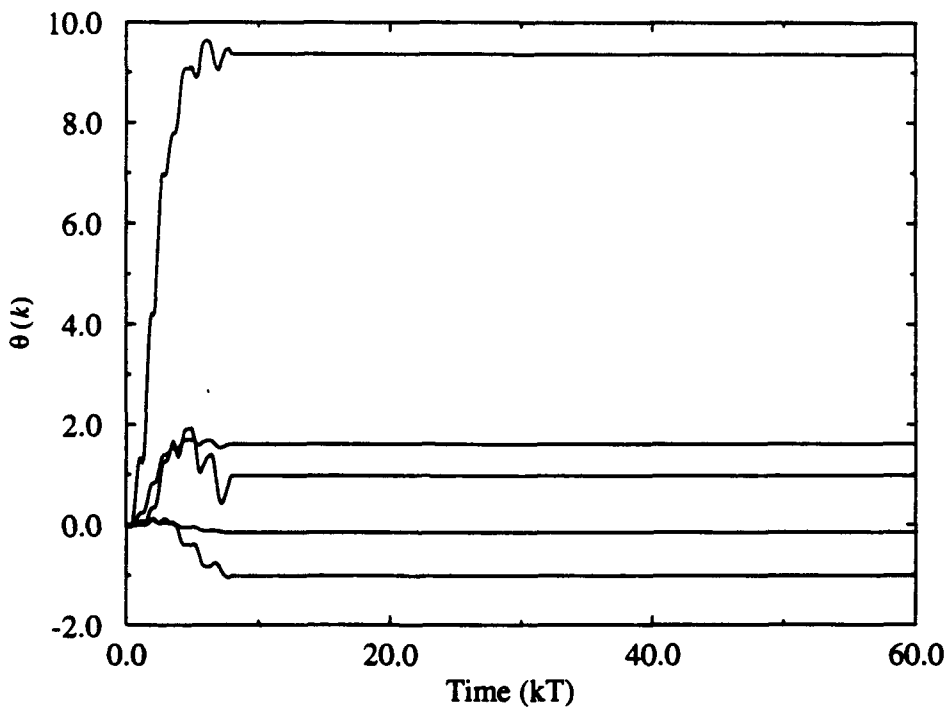


Figure 5.47 Evolution of Control Vector, $\theta(k)$ (Indirect MRAC)

6. Identification and Control Using Neural Networks

The linear and non-linear mapping properties of neural networks have been extensively utilized in system identification [112-117]. Many control strategies using neural networks have been suggested where both system identification as well as control is accomplished using multilayered networks. Most of the control strategies assume very little or no apriori knowledge about the system and therefore use the property of adaptation of the neural networks. Networks used for identification in these schemes do not provide any knowledge about the parameters of the mathematical model of the system. In this section, we have used a neural network to determine a linear model of a system in two different ways. First, we have used multilayered neural networks for determining the Markov parameters of a dynamical system from experimentally determined input-output sequences. A mathematical model of the structural system is then determined from these Markov parameters using the ERA. Second, we have developed a method of determining a linear state space model of a system from experimental test data using neural networks. In this method, a sequence of state vectors are calculated from the input-output data of the system. These state vectors along with the input-output data are used to train a multilayered network. The product of the weights of the trained network gives the state space model of the system. The neural network architectures for system identification utilize the standard backpropagation learning algorithm [112] for training and are often large in size. Therefore, such networks typically require very long training times. To enhance the rate at which such networks learn and hence to reduce the learning time, we have developed an accelerated adaptive learning rate algorithm. This algorithm adjusts the learning rate used in the standard backpropagation algorithm at every epoch so as to minimize the output error at a faster rate.

6.1. Neural Network Technique to Generate the Markov Parameters

In the method suggested by Bialasiewicz et. al [116], a multilayered feedforward network [see Fig. 6.1] is trained using the input-output data of the system. Once the network is trained, the required Markov parameters are found to be proportional to the product of the weighting matrices of the network.

The computational simplicity of this method is one of the main advantages over the conventional observer formulation to calculate the Markov parameters of a system. In addition, the noise rejection properties of the neural networks allow more accurate estimation of the Markov parameters from noisy experimental data as compared to the observer formulation.

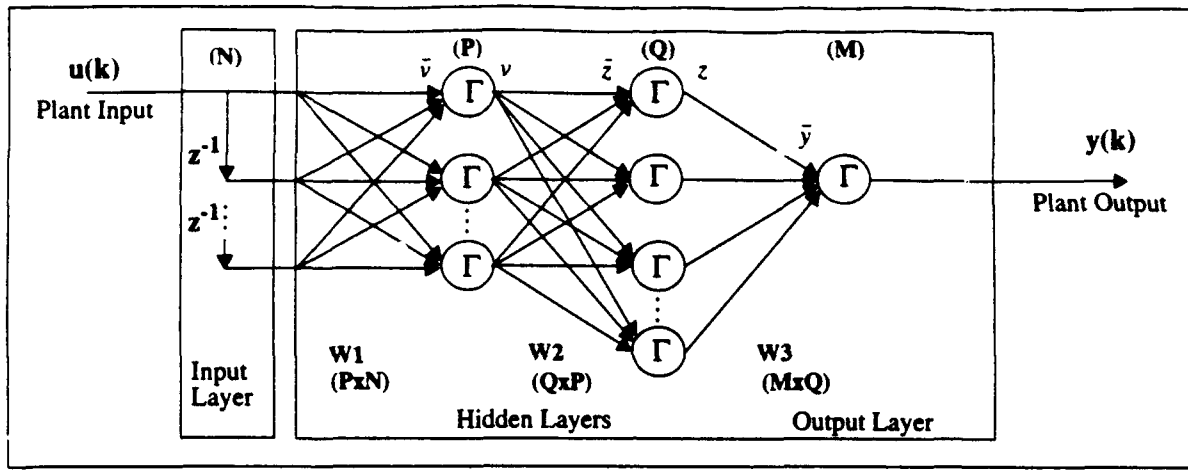


Figure 6.1. Neural network architecture for determining the Markov parameters

In the neural network shown in Figure 6.1, the activation functions used by each of the hidden layers and the output layer are hyperbolic tangent and a linear respectively. The hyperbolic tangent and the linear activation functions are given by

$$\begin{array}{ll} \text{Hyperbolic Tangent} & \Gamma(x) = K \tanh\left(\frac{1}{2}\alpha x\right) \\ \text{Linear} & \Gamma(x) = Kx \end{array} \quad (1)$$

The input to this network consists of only the past inputs of the plant [see Figure 6.1] whose Markov parameters are to be determined. Let the vector consisting of the past inputs of the plant be denoted by

$$Z^{-1}[u(k)] = \begin{bmatrix} u(k) \\ u(k-1) \\ \dots \end{bmatrix}_{N \times 1} \quad (2)$$

Let the number of neurons in the first hidden layer, second hidden layer and the output layer are P , Q and M respectively, then the input to the first hidden layer is

$$\bar{v}(k) = w_1 \times Z^{-1}[u(k)] \quad (3)$$

And the output of the first hidden layer is

$$v(k) = \Gamma(w_1 \times Z^{-1}[u(k)]) \quad (4)$$

Similarly, the input and output vectors of the second hidden layer and the output layer can be written as

$$\bar{z}(k) = w_2 \times v(k) \quad (5)$$

$$z(k) = \Gamma(w_2 \times \Gamma(w_1 \times Z^{-1}[u(k)])) \quad (6)$$

$$\bar{y}(k) = w_3 \times z(k) \quad (7)$$

$$y(k) = \Delta \times w_3 \times \Gamma(w_2 \times \Gamma(w_1 \times Z^{-1}[u(k)])) \quad (8)$$

where w_1 , w_2 and w_3 are the weighting matrices of the network and Δ is a constant. Equation (8) gives the relation between the output and the input of the network.

Once the network is trained, the neurons can be assumed to operate in the linear range of the nonlinear activation functions and will behave as a linear network within a certain range of input signals. Then, Eq. (8) can be approximated by

$$y(k) = \Delta \times [w_3 \times w_2 \times w_1] \times [Z^{-1}[u(k)]] \quad (9)$$

Now, consider an n^{th} order linear discrete time system described by

$$\begin{aligned} X(k+1) &= \Phi X(k) + \beta u(k) \\ y(k) &= CX(k) \end{aligned} \quad (10)$$

The system in Eq. (10) can also be described in terms of its Markov parameters as follows

$$y(k) = [C\Phi^0\beta \quad C\Phi^1\beta \quad C\Phi^2\beta \quad \dots \quad C\Phi^{N-1}\beta] \times Z^{-1}[u(k)] \quad (11)$$

where $[C\Phi^0\beta \quad C\Phi^1\beta \quad C\Phi^2\beta \quad \dots \quad C\Phi^{N-1}\beta]$ are the Markov parameters of the system.

From Eq. (9) and Eq. (11) it can be seen that for a proper choice of the number of past inputs (N) of the plant, the product of the weighting matrices of the network (Eq. (9)) is proportional to the Markov parameters of the system (Eq. (10)).

$$\Delta \times [w_3 \times w_2 \times w_1] = [C\Phi^0\beta \quad C\Phi^1\beta \quad C\Phi^2\beta \quad \dots \quad C\Phi^{N-1}\beta] \quad (12)$$

The Eigensystem Realization Algorithm can then be utilized to obtain a reduced order state space model

of the system from these Markov parameters.

6.2. Identification of State Space Model of a system using Neural Networks

Most neural network identification techniques as described in section 6.1 generate a neuro-model of a system such that the network response is similar to that of the system response for a given input. These neuro-models of systems cannot be used to design modern full state feedback controllers since no information about the parameters of the linear system are available. In 1991 Chow and Yam [118] suggested a method to identify the discrete time poles and zeros of a system from its input output data. This method assumes that the values of the transfer function coefficients were known within a certain range for training the neural network. This assumption seriously limits the applicability of this method to real world problems because there is seldom any information available about the model of a system.

In this section, an identification method based on feedforward neural networks to estimate a linear model of a system has been presented. In this method, the product of the weights of a trained feedforward network gives the state space matrices of a system.

Consider a system described by the following state space representation

$$\begin{aligned} x(k+1) &= Ax(k) + Bu(k) \\ y(k) &= Cx(k) + Du(k) \end{aligned} \quad (13)$$

where $x(k)$ is a $n \times 1$ dimensional state vector $u(k)$ and $y(k)$ are m and q dimensional input and output vectors respectively. They are described by the following equation

$$x(k) = \begin{bmatrix} x_1(k) \\ x_2(k) \\ \dots \\ x_n(k) \end{bmatrix} \quad u(k) = \begin{bmatrix} u_1(k) \\ \dots \\ u_m(k) \end{bmatrix} \quad y(k) = \begin{bmatrix} y_1(k) \\ \dots \\ y_q(k) \end{bmatrix} \quad (14)$$

Since a network with two hidden layers is shown to better approximate any mapping, a network as shown is used for the purpose of identification.

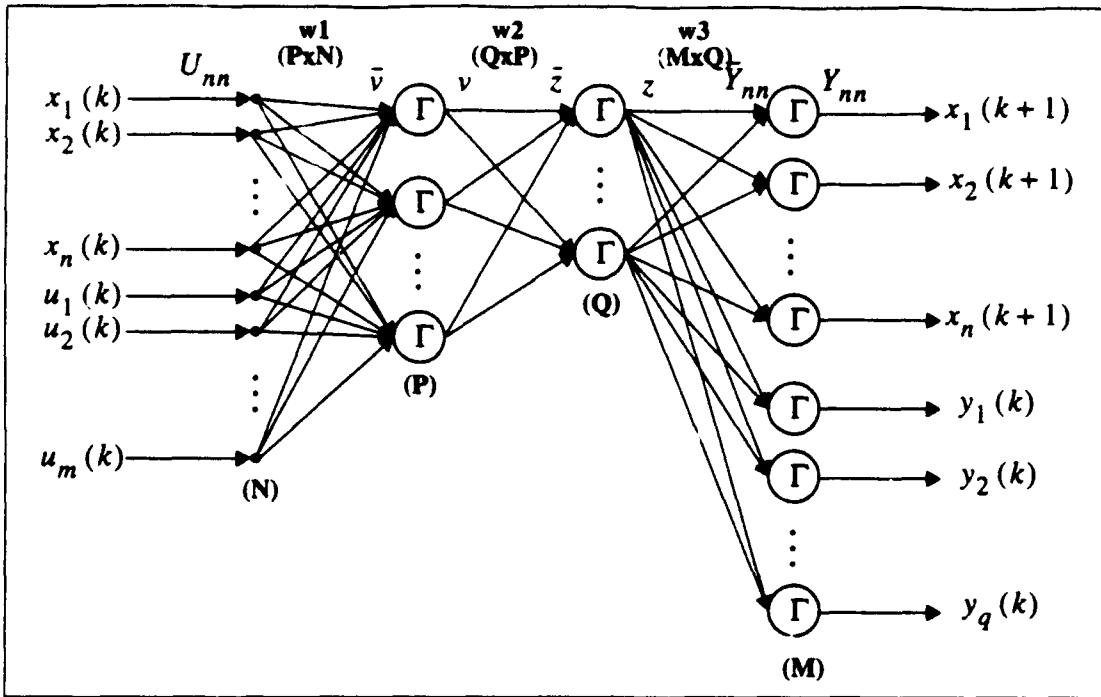


Figure 6.2. Architecture for Linear System Identification

Since this network tries to estimate models of linear systems, the activation functions used in all the layers are linear functions as given by the following equation

$$\Gamma(x) = Kx \quad (15)$$

where K is a constant defining the slope of the linear activation function. In addition, the network does not have any bias inputs. Let w_1 , w_2 and w_3 be the weighting matrices of the network shown in Fig. 6.2. Let \bar{v} , \bar{z} and \bar{y}_{nn} be the input vectors of the first hidden layer, second hidden layer and the output layer respectively. Let v , z and y_{nn} be the outputs of the first hidden layer, second hidden layer and the output layer respectively. Then the forward equations of the network in Fig. 6.2 are as follows.

Define

$$U_{nn}(k) = \begin{bmatrix} x_1(k) \\ x_2(k) \\ \vdots \\ x_n(k) \\ u_1(k) \\ \vdots \\ u_m(k) \end{bmatrix} \quad Y_{nn}(k) = \begin{bmatrix} x_1(k+1) \\ x_2(k+1) \\ \vdots \\ x_n(k+1) \\ y_1(k) \\ \vdots \\ y_q(k) \end{bmatrix} \quad (16)$$

Then the input and the output vector of the first hidden layer is given as

$$\begin{aligned}\bar{v} &= w_1 \times U_{nn} \\ v &= \Gamma(\bar{v}) = \Gamma(w_1 \times U_{nn})\end{aligned}\tag{17}$$

Similarly the input and output of the second hidden layer and the output layer are

$$\begin{aligned}\bar{z} &= w_2 \times v \\ &= w_2 \times \Gamma(w_1 \times U_{nn}) \\ z &= \Gamma(\bar{z}) = \Gamma(w_2 \times \Gamma(w_1 \times U_{nn}))\end{aligned}\tag{18}$$

$$\begin{aligned}\bar{Y}_{nn} &= w_3 \times z \\ &= w_3 \times \Gamma(w_2 \times \Gamma(w_1 \times U_{nn})) \\ Y_{nn} &= \Gamma(w_3 \times \Gamma(w_2 \times \Gamma(w_1 \times U_{nn})))\end{aligned}\tag{19}$$

Equation (19) gives the relation between the input and the output of the network. Since the activation functions used in all the layers are linear, Eq. (19) reduces to

$$Y_{nn} = [w_3 \times w_2 \times w_1] \times U_{nn}\tag{20}$$

Defining

$$w_{321} = w_3 \times w_2 \times w_1\tag{21}$$

and substituting for U_{nn} and Y_{nn} in Eq. (20)

$$\begin{bmatrix} x_1(k+1) \\ x_2(k+1) \\ \dots \\ x_n(k+1) \\ y_1(k) \\ \dots \\ y_q(k) \end{bmatrix} = w_{321} \times \begin{bmatrix} x_1(k) \\ x_2(k) \\ \dots \\ x_n(k) \\ u_1(k) \\ \dots \\ u_m(k) \end{bmatrix}\tag{22}$$

Now, the state space representation of the system in Eq. (13) can be rewritten as

$$\begin{bmatrix} x_1(k+1) \\ x_2(k+1) \\ \dots \\ x_n(k+1) \\ y_1(k) \\ \dots \\ y_q(k) \end{bmatrix} = \begin{bmatrix} A & B \\ C & D \end{bmatrix} \begin{bmatrix} x_1(k) \\ x_2(k) \\ \dots \\ x_n(k) \\ u_1(k) \\ \dots \\ u_m(k) \end{bmatrix} \quad (23)$$

Comparing Eq. (22) and (23)

$$w321 = [w3 \times w2 \times w1] = \begin{bmatrix} A & B \\ C & D \end{bmatrix} \quad (24)$$

From Eq. (24) it can be seen that when a network is trained with the state vector, the input vector and the output vector of a system as shown in Fig. 6.2, the product of the weighting matrices is the augmented state space matrix of that system.

For this identification method, the input output record can be collected experimentally and the state vectors of the system can be calculated off line from the input output sequence using an algorithm suggested by Moonen et. al [3] as outlined below.

The sequence of experimentally determined input output sequence is used to form two block Hankel matrices as shown

$$H_1 = \begin{bmatrix} Y_{h1} \\ U_{h1} \end{bmatrix} \quad H_2 = \begin{bmatrix} Y_{h2} \\ U_{h2} \end{bmatrix} \quad (25)$$

where

$$Y_{h1} = \begin{bmatrix} y(k) & y(k+1) & \dots & y(k+j-1) \\ y(k+1) & y(k+2) & \dots & y(k+j) \\ \dots & \dots & \dots & \dots \\ y(k+i-1) & y(k+i) & \dots & y(k+i+j-2) \end{bmatrix} \quad (26)$$

$$Y_{h2} = \begin{bmatrix} y(k+i) & y(k+i+1) & \dots & y(k+i+j-1) \\ y(k+i+1) & y(k+i+2) & \dots & y(k+i+j) \\ \dots & \dots & \dots & \dots \\ y(k+2i-1) & y(k+2i) & \dots & y(k+2i+j-2) \end{bmatrix} \quad (27)$$

U_{h1} and U_{h2} are similarly constructed. Here, i and j are constants such that $j \gg \text{maximum}(mi, qj)$.

Then let

$$H = \begin{bmatrix} H_1 \\ H_2 \end{bmatrix} \quad (28)$$

Then the singular value decomposition (SVD) of H gives

$$H = \begin{bmatrix} U_{11} & U_{12} \\ U_{21} & U_{22} \end{bmatrix} \begin{bmatrix} S_{11} & 0 \\ 0 & 0 \end{bmatrix} V^T \quad (29)$$

where the dimensions of the submatrices in Eq. (29) are

$$\begin{aligned} S_{11} &= (2mi + n) \times (2mi + n) \\ U_{11} &= (mi + qj) \times (2mi + n) \\ U_{12} &= (mi + qj) \times (2qj - n) \\ U_{21} &= (mi + qj) \times (2mi + n) \\ U_{22} &= (mi + qj) \times (2qj - n) \end{aligned} \quad (30)$$

Now define the state vector sequence

$$X = [x(k+i) \quad x(k+i+1) \quad \dots \quad x(k+i+j-1)] \quad (31)$$

Then

$$X = U_q^T U_{12}^T H_1 \quad (32)$$

where U_q is obtained from the singular value decomposition of the product of the matrices $U_{12}^T U_{11} S_{11}$ as

given by the equation

$$U_{12}^T U_{11} S_{11} = [U_q \quad U_q^\perp] \begin{bmatrix} S_q & 0 \\ 0 & 0 \end{bmatrix} \begin{bmatrix} V_q^T \\ V_q^{T\perp} \end{bmatrix} \quad (33)$$

6.3. Accelerated adaptive learning algorithm

Feedforward neural networks used for system identification [Fig. 6.4] tend to be very large in size. Since such networks often use the standard backpropagation algorithm for training, the number of iterations and hence the time required for training tends to be very large. In addition, a network which learns using the backpropagation algorithm with a constant learning rate, tends to settle in a local minimum if an appropriate learning rate is not chosen. In the standard backpropagation algorithm the weights of the network are updated using the recursive formula

$$W(k+1) = W(k) - \eta \frac{\partial}{\partial e} W(k) \quad (34)$$

where W 's are the weights of the network, η is the learning rate and e is the error between the output of the network and the desired output.

The rate at which a network learns using the standard backpropagation algorithm can be enhanced by changing the learning rate at the end of every epoch of training. The basic idea behind the proposed accelerated learning algorithm is to increase the learning rate if the sum of the squared error (SSE) over one epoch is less than the previous epoch and to decrease it if the SSE is greater. Thus the new weights updating equation becomes

$$W(k+1) = W(k) - \eta(kk) \frac{\partial}{\partial e} W(k) \quad (35)$$

where $\eta(kk)$ is the learning rate calculated at the end of every epoch for $kk = 1, 2, \dots$

If the SSE continues to drop over consecutive learning epochs, the rate of increase of $\eta(kk)$ is accelerated. Similarly, if the SSE increases over consecutive training epochs, the rate of decrease of $\eta(kk)$ is accelerated. While accelerating the increment in the learning rate, care must be taken to avoid a sudden increase in the SSE towards the end of the learning curve. To avoid such an increase in the SSE, the acceleration coefficient used is smaller when the SSE is very small. The steps involved in the algorithm and the different conditions which control the increase or decrease of the learning rate η is outlined in the flow diagram in Fig. 6.5.

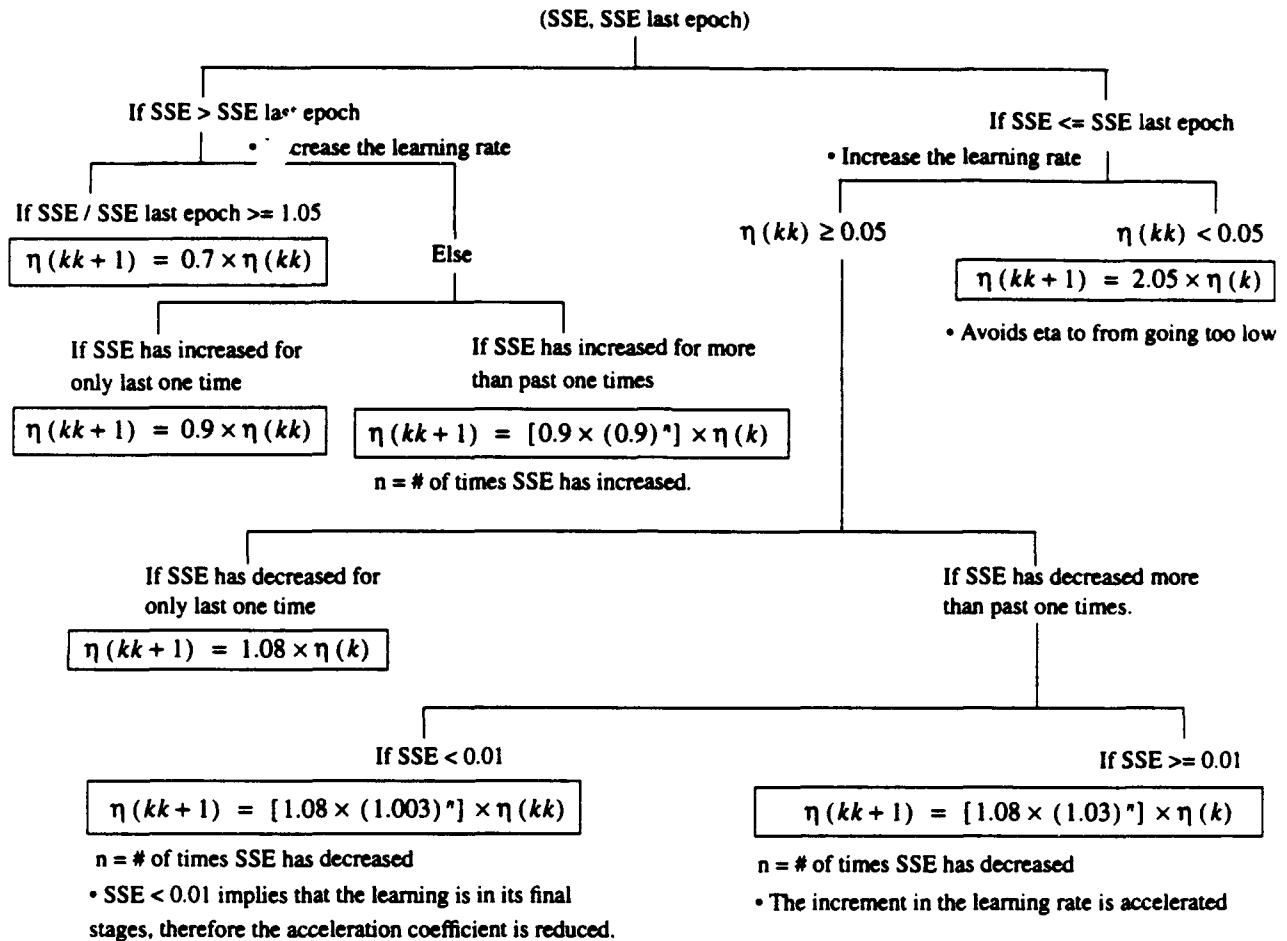


Figure 6.3. Accelerated Adaptive Learning Algorithm

The constants in the algorithm shown in Fig. 6.5 are empirically found to work for most problems, although they may be changed slightly to best suit a particular problem. As a general rule the initial value of $\eta(kk)$ is chosen to be very small. The algorithm will then increase or decrease the learning rate depending upon the SSE at the end of each epoch.

6.4. Comparison of the Identified Models

The cantilever beam was excited for 60 seconds with a random input uniformly distributed between ± 5 volts, and its response sampled every 0.2 seconds. This data set was used to generate a model using the neural network - ERA method and the neural network based direct identification method. In the neural network-ERA procedure, the architecture of the network used was a $120 \times 120 \times 60 \times 1$. The activation functions used

were the hyperbolic tangent functions given by Eq. (1). The size of the network was determined by increasing the number of neurons in the input and the first hidden layer until the output error of the trained network was on the order of 10^{-3} . In the direct state variable identification method, the parameters used to form the block Hankel matrix of the system inputs and outputs were $k = 10$, $j = 900$ and $i = 100$. Since the system is a single input single output (SISO) system $m = 1$ and $q = 1$. The singular value decomposition of this Hankel matrix resulted into the size of the matrix S_{11} in Eq. 6.29 to be 203. Then the order of the system was determined to be equal to three as follows

$$\begin{aligned}2mi + n &= 203 \\n &= 203 - (2 \times 1 \times 100) \\n &= 3\end{aligned}\tag{36}$$

A network of size $4 \times 10 \times 10 \times 4$ was trained using the appropriate training vectors. Initially, the standard backpropagation algorithm was used to train the network. Due to the size of the network, a very large number of iterations were required for satisfactory training. To decrease the number of training iterations, the accelerated adaptive learning rate algorithm, outlined in Fig. 6.3, was developed and implemented. A comparison of the performance of the SSE of the network with the standard adaptive learning rate algorithm and the accelerated adaptive learning rate algorithm is shown in Fig. 6.4. In the standard adaptive learning rate algorithm, the learning rate is increased by a factor and the weights are updated at the end of every epoch only if SSE reduces. Otherwise, the learning rate is reduced by a factor and the update of the weights are set to zero. The superiority of the accelerated learning, both in terms of learning rate and the squared error performance can be seen from Fig. 6.4.

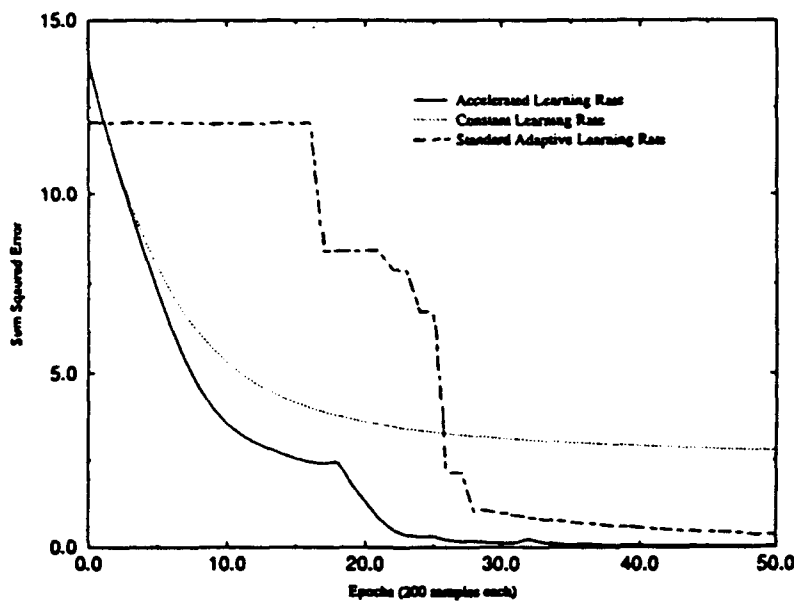


Figure 6.4. Comparison of performance of various learning rate algorithms

The state variable model of the beam obtained directly from the neural network is given in the following equation

$$A_{nn2} = \begin{bmatrix} -0.5517 & -3.5755 & -3.4387 \\ 0.1242 & -0.3079 & -1.8064 \\ 0.0653 & 0.2523 & 0.6215 \end{bmatrix} \quad B_{nn2} = \begin{bmatrix} 0.1242 \\ 0.0653 \\ 0.0137 \end{bmatrix} \quad (37)$$

$$C_{nn2} = [0.0012 \quad -0.0010 \quad 0.1300] \quad (38)$$

The equivalent continuous time transfer function (at T = 0.2 sec) is

$$G_{nn2}(s) = \frac{0.003s^2 - 0.0062s + 2.0313}{s^3 + 4.9072s^2 + 89.01s + 432.5375} \quad (39)$$

In comparison, the discrete time state space model (T = 0.2 sec) of the cantilever beam generated using the neural network - ERA method was

$$\Phi_{nn} = \begin{bmatrix} -0.3067 & 0.9420 & 0.0316 \\ -0.9420 & -0.2971 & -0.1595 \\ -0.0316 & -0.1595 & 0.7465 \end{bmatrix} \quad \beta_{nn} = \begin{bmatrix} 0.0510 \\ -0.0154 \\ 0.0459 \end{bmatrix} \quad C_{nn} = [-0.051 \quad -0.0154 \quad 0.0459] \quad (40)$$

The continuous time transfer function equivalent of Eq. (40) is

$$G_{nn}(s) = \frac{-0.0006s^2 - 0.1069s + 1.1652}{s^3 + 1.4554s^2 + 89.4893s + 120.1713} \quad (41)$$

The comparison of the frequency response of the two models obtained using the neural network based methods and the measured frequency response of the beam is shown in Fig. 6.5.

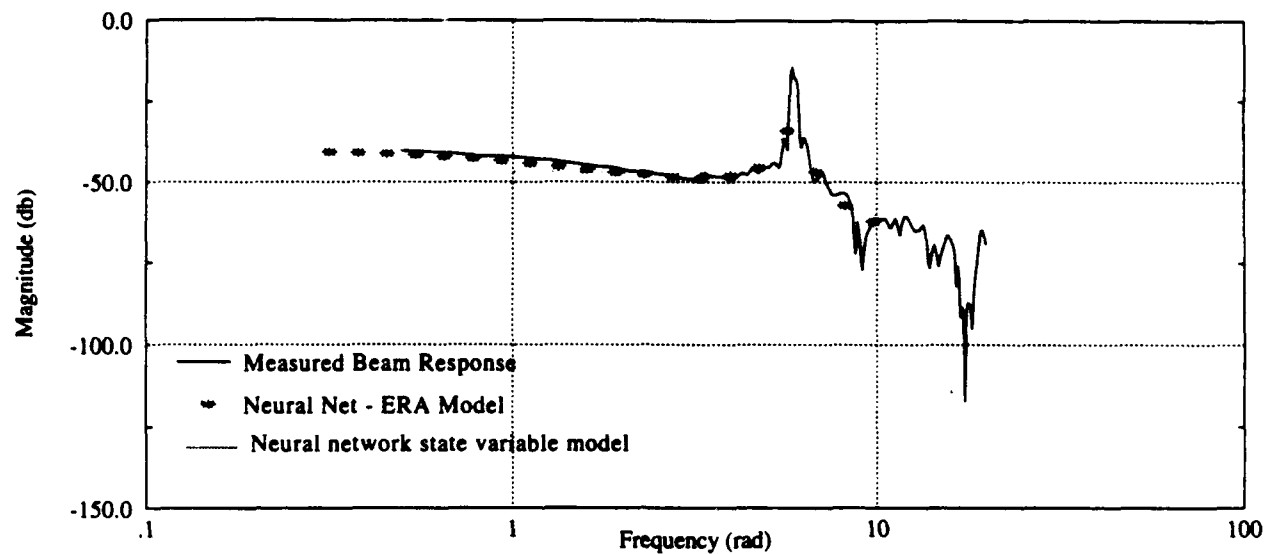


Figure 6.5. Comparison of the frequency responses

Figure 6.5 shows that there is an acceptable match between the frequency of the first mode of the two models and the measured frequency response of the beam.

6.5. Neural network Based Robust Controller

As a first step towards using a neural network as a controller with real-time adaptation capabilities, the LQG/LTR controller with the modified structure was copied by a multilayered feedforward type neural network. The two controllers were then compared for the closed loop performance and robustness properties against plant uncertainties.

The network setup to copy the LQG/LTR controller is as shown in Fig. 6.6.

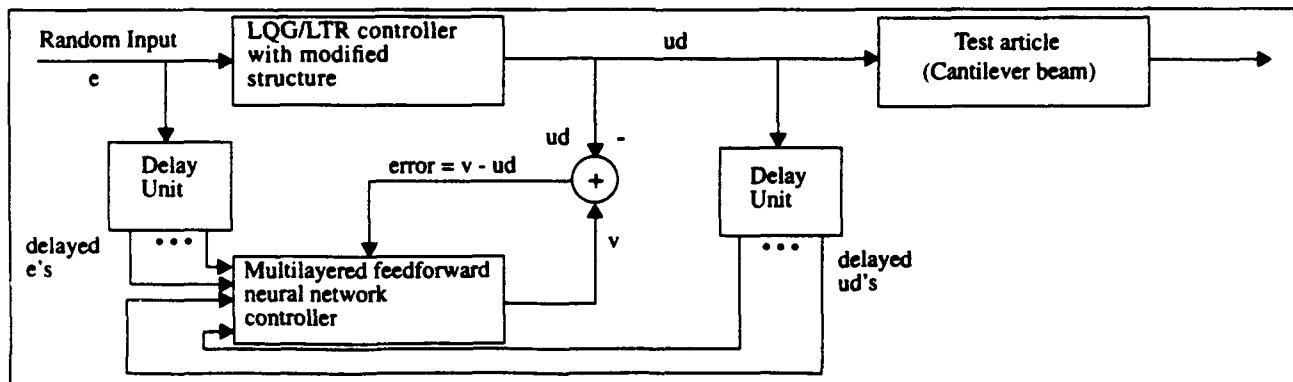


Figure 6.6. Neural network training scheme to copy the LQG/LTR controller

The architecture of the neural network used to replace the LQG/LTR controller is shown in Fig. 6.7. This architecture follows the structure suggested by Narendra and Kannan [112] when the dynamics of the system to be copied is completely unknown.

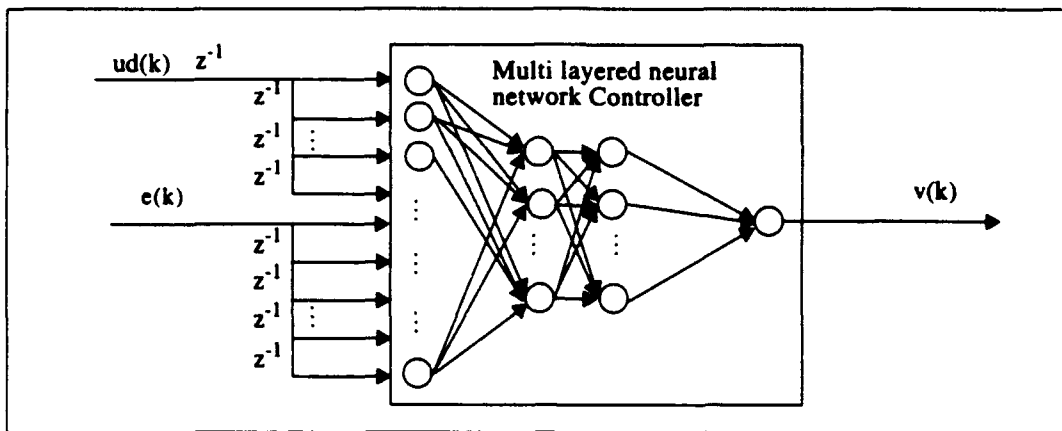


Figure 6.7. General network architecture used to copy the LQG/LTR controller

In this particular application, since the neural network will replace the LQG/LTR control, which is known apriori to be linear. Hence linear activation functions were chosen for each of the neurons in the network. Since linear activation functions do not have a saturation limit, care must be taken to select small initial weights depending upon the size of the network chosen. One way to circumvent this problem is to chose linear activation function with hard limits such as

$$\begin{aligned}\Gamma(x) &= 1 && \text{if } (x \geq 1) \\ \Gamma(x) &= x && \text{if } (1 > x > -1) \\ \Gamma(x) &= -1 && \text{if } (x \leq -1)\end{aligned}\quad (42)$$

Following Eq. (3) through Eq. (9), the output of the network in Fig. 6.7 with two hidden layers can be written as

$$y(k) = [w_3 \times w_2 \times w_1] \times Z^{-1} \begin{bmatrix} u(k) \\ y(k) \end{bmatrix}_{N \times 1} \quad (43)$$

The network is trained using the standard backpropagation algorithm with the accelerated adaptive learning rate algorithm to reduce the learning time. Once the network satisfactorily learns the LQG/LTR controller, it is placed in the control loop and the performance of the closed loop system is investigated.

A feedforward network of size $20 \times 20 \times 10 \times 1$ was chosen to copy the controller. The input to the network consisted of the past 11 inputs and the past 9 outputs of the controller. All the activation functions were linear and the initial values of the weights were set between ± 0.2 . The training set consisted of 300 input-output pairs of the response of the LQG/LTR controller to a uniformly distributed random input between

± 1 volt. The weighting matrices of the trained network were then used to implement the controller according to Eq. (43).

6.6. Examination of robustness properties

The closed loop performance of the cantilever beam with the modified LQG/LTR controller and the neural network controller for nominal and increased tip mass is compared in Fig. 6.8 and 6.9. The criterion used to compare the closed loop performance of the system was the time taken by the oscillations of the closed loop system to go below 0.2 volts. Below 0.2 volts the actuators are in their dead band and hence there is no control force applied on the beam to suppress the vibrations.

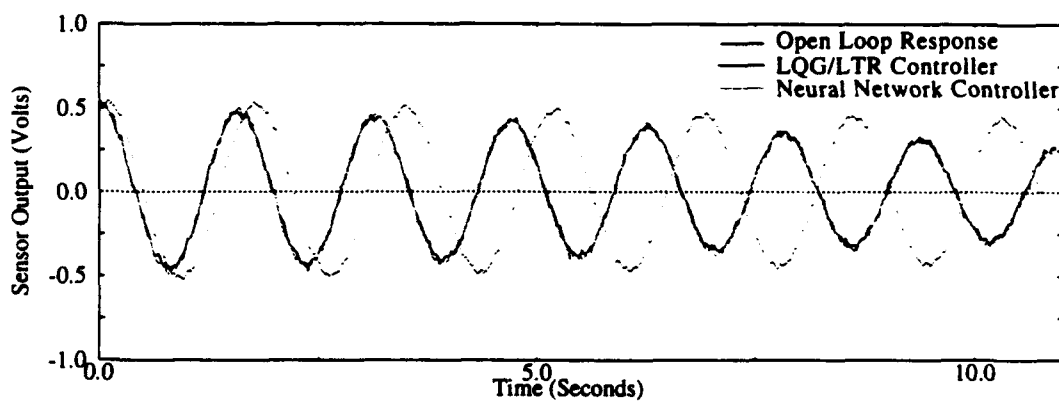


Figure 6.8. Closed loop performance of the controllers for nominal tip mass

With a nominal tip mass, the vibrations of the closed loop system damped down below 0.2 volts in about 10 seconds as compared to the 70 seconds for the open loop system. From Fig. 6.8 it can be seen that natural frequency of the closed loop system is slightly higher than that of the open loop system. This is due to the stiffness added to the system when the NiTiNOL wires contract and exert force on the cantilever beam. The skew in the initial condition of the open loop and closed loop plots seen in Fig. 6.8 is due to the human error involved in deflecting the beam to about 6 inches before releasing it.

To examine the robustness of the controllers against variations in mechanical configuration, the tip mass was increased by 38%. The performance of the two controllers for increased tip mass is shown in Fig. 6.9.

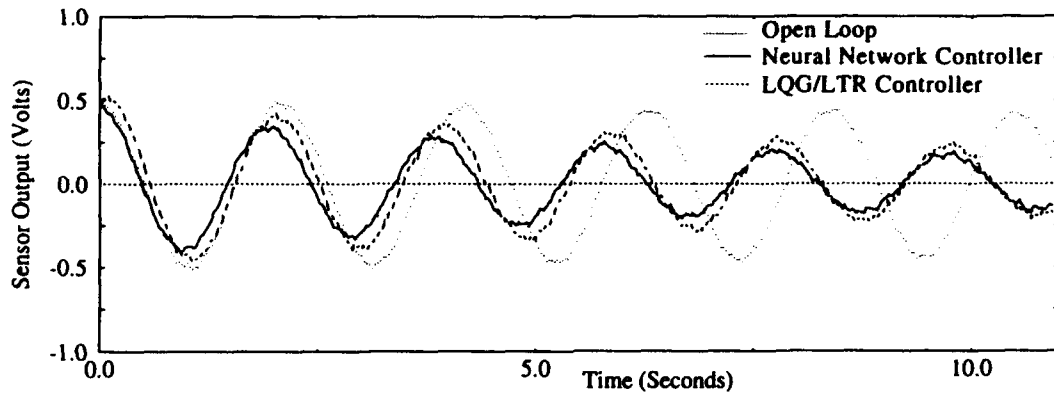


Figure 6.9. Closed loop performance of the controllers for increased tip mass

Figures 6.8 and 6.9 show that the closed loop performance of the modified LQG/LTR controller and the neural network controller did not degrade significantly due to increased tip mass. In addition to the tip mass uncertainty, a robustness study was also conducted for an uncertainty in the sampling rate of the controller. The closed loop response of the beam for an increased sampling time is shown in Fig. 6.10.

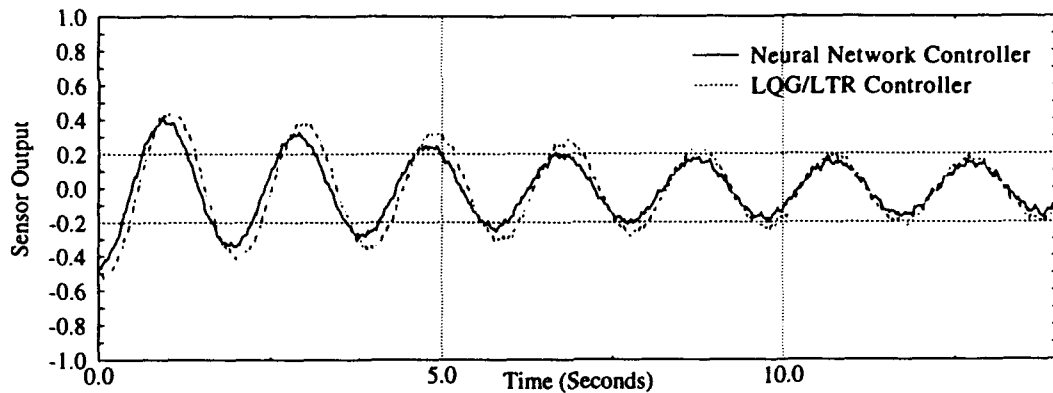


Figure 6.10. Closed loop performance with sampling time increased from 0.02 sec to 0.1 sec

Figure 6.10 shows that the LQG/LTR controller took longer to dampen the vibrations of the beam to below 0.2 volts than the neural network controller when the sampling time was increased.

7. Summary

This report has been an overview of a fairly extensive study on applying different control techniques to smart structures using shape memory alloys. The salient results are summarized below.

1. Development of new shape memory alloys

Indium-thallium alloys in the range 15-38 at%Tl were electrodeposited from a sulfate electrolyte using pulsed current. The relationship between composition and phase structure of the alloys deposited was investigated with regard to the shape memory effect. To date there have been no reported experimental studies describing the electrodeposition of In-Tl alloys capable of undergoing such transformations. Not only did the deposited alloys exhibit the shape memory effect, but the composition-phase relationship was shown to deviate from that reported for alloys in an equilibrium condition. The results show that the temperature and the temperature interval for the transformation of the electrodeposited alloys are substantially different from those of the thermally prepared alloys. The shape recovery for the electrodeposited alloys was also confirmed.

Cu-Zn, Au-Cd, In-Tl and In-Cd alloy films were produced using electrolytic techniques and their shape memory properties were evaluated. Cyanide solutions were used for the Cu-Zn and Au-Cd deposits, but sulfate solutions were preferred for the indium alloys. The use of pulsed current was beneficial in giving dense and uniform deposits. The Cu-Zn and Au-Cd alloys did exhibit a degree of brittle behavior in the as-deposited condition. Simple bending tests were conducted and shape memory effects were confirmed on the Cu-Zn and indium alloys. The phases present were determined at different temperatures using X-ray diffraction. A low temperature unit was used for Cu-Zn and Au-Cd while an elevated temperature furnace attachment was necessary for the indium alloys. The phases identified at ambient temperature for Cu-Zn and Au-Cd deposits were identified as ones normally found at elevated temperature for alloys in an equilibrium condition. The phase transformation behavior of the electrodeposited shape memory alloys, in general, was different from those exhibited by equilibrium alloys prepared using conventional thermal preparation techniques. The results show that electrolysis appears to be a feasible means of producing certain shape memory thin films with potentially interesting properties. However, more extensive studies are needed to optimize the performance of the electrodeposited alloy films.

2. Design and fabrication of smart structures test articles

We have acquired a great deal of knowledge in the hardware design and fabrication of smart structure test articles. All the signal processing, interfacing, and data acquisition circuits are developed in our laboratory by graduate students. We have developed a state-of-the-art laboratory facility in the smart structures area.

3. Identification and robust control of smart structures

In this research effort, we wanted to use shape memory alloy actuators to dampen vibrations of a flexible structure. First, a mathematical model was developed using the ERA technique. This technique allowed us to generate an accurate model of the flexible structure even in the presence of sensor noise. The presence of substantial amounts of noise in the output measurements required a proper selection of an extra set of real observer poles close to the origin in the asymptotically stable observer formulation. This considerably helped averaging out the effects of noise in calculation of the Markov parameters of the system while minimizing the calculation time. The presence of noise also drove the need to use a larger window size and larger number of observer poles. Once the ERA model was obtained, we implemented a standard LQG/LTR controller with no restriction on controller effort. This controller saturated the actuators to an unacceptable degree. Next, we reduced the amount of loop transfer recovery until the controller no longer saturated the actuators. However, this controller was sensitive to system uncertainties. Finally, we implemented a modified LQG/LTR controller. This modified structure quickened the loop transfer recovery process allowing us to design a controller that was both insensitive to system uncertainties and did not saturate the actuators. We successfully implemented this modified LQG/LTR controller on the flexible structure and demonstrated its insensitivity to uncertainties. This experiment showed that the modified LQG/LTR controller was robust to tip mass uncertainty.

4. Adaptive control using neural networks

The adaptive control algorithms have been utilized for designing active controllers for smart structure test articles. Adaptive control schemes require only a limited a priori knowledge about the system to be controlled. The availability of limited control force and inherent deadband and saturation effects of shape memory alloy actuators are incorporated in the selection of a reference model. The vibration suppression properties of smart structures were successfully demonstrated by implementing the conventional model reference adaptive controllers on test articles. The

controller parameters were converged to steady state values within 8 seconds for both direct and indirect model reference adaptive controllers (MRAC).

Various neural network based adaptive control techniques were discussed in this paper. We have successfully demonstrated the utilization of neural networks for system identification using off-line experimental data. A major problem in implementing neural network based MRAC is the translation of output error between the plant and the reference model to train the neural controller. A technique called iterative inversion to invert the neural identification model of the forward dynamics of the plant for calculating neural controller gains has been used. Due to real-time computer hardware limitation, the performance of neural network based adaptive control systems is verified using simulation studies. These results show that the neural network based MRACs can be designed and implemented on smart structures.

List of All Publications and Technical Reports

- (1) C.H.Sonu, T.J. O'Keefe, S.V. Rao, and L.R. Koval, " Investigation of Shape Memory Properties of Electrodeposited Indium-Thallium Alloys," Proceedings of the ADPA/ AIAA/ ASME/ SPIE Conference on Active Materials and Adaptive Structures, November 1991, Alexandria, VA, pp 411-414.
- (2) R. Lashlee, R. Damle, V. Rao, and F. Kern, " Identification and Robust Control of Flexible Structures Using Shape Memory Actuators," Proceedings of Smart Structures and Materials 1993, Albuquerque, NM, SPIE Vol.1919, pp 271-282
- (3) C. Tebbe, T. Schroeder, R. Butler, V.Rao, L. Koval, and F. Kern, " Modeling and Robust Control of Smart Structures," Proceedings of Smart Structures and Materials 1993, Albuquerque, NM, SPIE Vol.1919, pp 283-297
- (4) J. Frimpong, C.H. Sonu, T.R. Hymer, and T.J. O'Keefe, Electrochemical Synthesis of Shape Memory Alloys," Proceedings of Smart Structures and Materials 1993, Albuquerque, NM, SPIE Vol.1916, pp 362- 372
- (5) S.W. Rhee and L.R. Koval, " A Comparison of Classical Control with Robust Control for SMA Smart Structures," Proceedings of Smart Structures and Materials 1993, Albuquerque, NM, SPIE Vol.1917.
Accepted for publication in the Journal of Smart Materials and Structures.
- (6) C. H. Sonu and T.J. O'Keefe, " Characterization of Phase Transformation Behavior in Electrolytically Produced Indium-Thallium Shape Memory Alloy Films," Accepted for publication in " Material Characterization" , an International Journal on Materials Structure and Behavior.
- (7) R. Lashlee, R. Butler, V. Rao and F. Kern, " Robust Control of Flexible Structures Using Multiple Shape Memory Alloy Actuators," Proceedings of The First IEEE Regional Conference on Aerospace Control Systems, Westlake Village, CA, May 1993, pp 798-804.
- (8) V. Rao and R. Butler, " Optimal Control of Infinite Order Composite Structural Systems Using Distributed PVDF Sensors, " Army Research Office Workshop on Dynamic Response of Composite Structures, New Orleans, LA, August 1993.

- (9) R. Damle, R. Lashlee, V. Rao, and F. Kern, " Identification and Robust Control of Smart structures Using Artificial Neural Networks," Accepted for publication in the Journal of Smart Materials and Structures.
- (10) V. Rao, R. Damle, C. Tebbe, and F. Kern, " Adaptive Control of Smart Structures Using Artificial Neural Networks, " Army Research Office Workshop on Smart Structures, Arlington, TX, September 1993.
- (11) C.H. Sonu, T.R. Hymer, M. Fang, and T.J. O'Keefe, " Electrodeposition Processing of Shape Memory Alloys,"Army Research Office Workshop on Smart Structures, Arlington, TX, September 1993.

Technical Reports

- (1) C.H. Sonu, " The Electrodeposition of Metals and Alloys Using Pulsed Current," Ph.D. Thesis, University of Missouri-Rolla
- (2) S.W. Rhee, " Robust Control of Smart Structures," Ph.D. Thesis, University of Missouri-Rolla.
- (3) Chris Tebbe, " Adaptive Control of Smart Structures Using Neural Networks," M.S. Thesis, University of Missouri-Rolla
- (4) Rajendra Damle," Identification and Robust Control of Smart Structures Using Neural Networks,"M.S. Thesis, University of Missouri-Rolla

List of All Participating Scientific Personnel

- (1) Dr. Vittal S. Rao
Professor of Electrical Engineering
- (2) Dr. Thomas J. O'Keefe
Curators' Distinguished Professor of Metallurgical Engineering
- (3) Dr. Leslie R. Koval
Professor of Mechanical Engineering
- (4) C. H. Sonu
Advanced Degree earned: Ph.D. in Metallurgical Eng
- (5) S.W. Rhee
Advanced Degree earned: Ph.D. in Mechanical Eng
- (6) R. Damle
Advanced Degree earned: M.S. in Electrical Eng
- (7) Chris Teebe
Advanced Degree earned: M.S. in Electrical Eng
- (8) Tim Hymer
Ph.D. Student in Metallurgical Engineering

REFERENCES

1. Y. Motohashi, K. Ohsawa, T. Hoshiya, Y. Okamoto and M. Ohmori, "Grain refinement of a Ti-Ni shape memory alloy and its influence on phase transformation characteristics," *J. Jpn. Inst. Met.*, Vol.55, pp.132-140, February 1991.
2. T. W. Duerig, J. Albrecht and G. H. Gassinger, "A shape-memory alloy for high-temperature applications," *J. Met.*, Vol.34, pp. 14-20, December 1982.
3. R. D. Jean, T. Y. Wu and S. S. Leu, "The effect of powder metallurgy on Cu-Al-Ni shape memory alloys," *Scrip. Met.*, Vol.25, pp.883-888, April 1991.
4. T. Minemura, "Shape memory effect and microstructures of sputter-deposited Cu-Al-Ni films," *J. Mat. Sci. Lett.*, Vol.4, pp.793-796, 1985.
5. J. Perkins, J. J. Rayment, B. Cantor and R. W. Cahn, "Grain boundary structures in rapidly solidified Cu-Zn-Al alloys," *Scrip. Met.*, Vol.15, pp. 771-776, 1981.
6. J. Perkins, "Rapid solidification effects in martensitic Cu-Zn-Al alloys," *Met. Trans.*, Vol.13A, pp. 1367-1372, August 1982.
7. M. Igharo and J. V. Wood, "Effect of rapid solidification processing on shape memory characteristics of equiatomic TiNi," *Proceed. Phase Transformations'87*, The Institute of Metals, pp.71-73, 1988.
8. A. Brenner, *Electrodeposition of alloys*, Vol.I, Academic Press, N.Y. and London, 1963.
9. L. Delaey, R. V. Krishnan and H. Tas, "Thermoelasticity, pseudoelasticity and the memory effects associated with martensitic transformation part1," *J. Mat. Sci.*, Vol.9, pp. 1521-1535, 1974.
10. B. Nishiyama, *Martensitic Transformation*, Academic Press, N.Y., 1978.
11. N. Ibl, J. Cl. Pupipe and H. Angerer, "Electrocryallization in pulse electrolysis," *Surf. Tech.*, Vol.6, pp.287-300, 1978.

12. W. F. Fluehmann, F. H. Reid, P. A. Mausli and S. G. Steinemann, "Effect of Pulsed current plating on structure and properties of gold-cobalt electrodeposits," *Plat. and Surf. Fin.*, Vol.67, pp.62-65, June 1980.
13. T. A. Eckier, B. A. Manty and P. L. McDaniel, "Pulse plating of chromium-molybdenum coating," *Plat. and Surf. Fin.*, Vol.67, pp.60-64. September 1980.
14. N. Ibl, "Some theoretical aspects of pulse electrolysis," *Surf. Tech.*, Vol.10, pp. 81-104, 1980.
15. S. Kujiwara and T. Kikuchi, "Dislocation structures produced by reverse martensitic transformation in a Cu-Zn alloy," *Acta Metall.*, Vol.30, pp.589-598, 1982.
16. H. M. Ledbetter and C. M. Wayman, "On β AuCd martensites," *Met. Trans.*, Vol.3, pp.2349-2356, September 1972.
17. N. Nakanishi, "Study of superelasticity associated with the thermoelastic martensitic transformation in Au-Cd alloys," *Phil. Mag.*, Vol.28, pp.277-292, 1973.
18. V. M. Plovov and E. G. Ponyatovskii, "On the thermodynamics of face-centered tetragonal \rightleftharpoons face-centered cubic transitions in indium alloys," *Sov. Phys. JETP*, Vol.37, pp.476-479, 1973.
19. T. B. Massalski, *Binary Alloy Phase Diagram*, 2nd ed., Vol.2, ASM International, 1990.
20. T. A. Schroeder and C. M. Wayman, "The formation of martensite and the mechanism of the shape memory effect in single crystals of Cu-Zn alloys," *Acta Metall.*, Vol. 25, pp. 1375-1391, 1977.
21. T. A. Schroeder and C. M. Wayman, "Martensite-to-martensite transformations in Cu-Zn alloys," *Acta Metall.*, Vol.26, pp. 1745-1757, 1978.
22. K. Otsuka and K. Shimizu, "Memory effect and thermoelastic martensitic transformation," *Scilp. Met.*, Vol.4, pp.469-472, 1970.
23. L. Crystal structure and transformations in indium-thallium solid solutions," *Trans. AIME*, Vol.188, pp.1472-1477, December 1950.

24. J. Petel and S. Ahmed, "Thermodynamic and X-ray studies of fcc to fct phase transformation in In-Tl system," *Met. Sci.*, pp. 147-150, March 1978.
25. O. Nittono and Y. Koyama, "Cubic-tetragonal transformation and shape memory behavior in indium-thallium and indium-cadmium alloys," *Trans. Jpn. Inst. Met.*, Vol.23, pp.285-295, June 1982 .
26. Bergamasco, M. et al., *Sensors and Actuators A21-A23* 253 (1990)
27. Guttman, L., *Trans. AIME* 188(12) 1472 (1950)
28. Hashimoto, M et al., *J. Robotic System*, 2 3 (1985)
29. Lipton, C. and Sheth, N.J., Statistical Design and Analysis of Engineering Experiments, McGraw-Hill Co. N.Y. (1973)
30. Neukomm, P. et al., *Sensors and Actuators A21-A23* 247 (1990)
31. Nittono, O. and Koyama, Y., *Trans. Inst. Met. Japan* 23(6) 28 (1982)
32. Murphy, T.D., *Chem. Eng.* June 168 (1977)
33. V.M. Polovov and E.G. Ponyatovsdii, On the Thermodynamics of Face-centered Tetragonal Cubic Transitions in Indium Alloys, Sov. Phys. JEPT, 37(3): 476-480 (1973)
34. L. Guttman, Crystal Structures and Transformations in Indium-Thallium Solid Solutions, *Trans. AIME*, 188(12):1472-1477 (1950)
35. J.S. Bowles, et al., Crystallography of the Cubic-Tetragonal Transformation in the Indium-Thallium System, *Trans. AIME*, 188(12): 1478-1485 (1950)
36. Z.S. Basinski and J. W. Christian, Experiments on the Martensitic Transformation in Single Crystals of Indium-Thallium Alloys, *Acta Met.* 2(1): 148-166 (1954)

37. Z.S. Basinski and J.W. Christian, Crystallography of Deformation by Twin Boundary Movement in Indium-Thallium Alloys, *Acta Met.*, 2(1): 101-106 (1954)
38. A. Moore, et al., An X-ray Examination of Crystallographic Transformations in Indium-Rich Solid Solutions with Thallium, Lithium and Lead, *Acta Met.*, 3: 579-589 (1955)
39. J. Petel and S. Ahmed, Thermodynamic and X-ray Studies of fcc to fct Phase Transformation in In-Tl System, *Met. Sci.*, 147-150 (1978)
40. J.T.A. Pollock and H.W. King, Low Temperature Martensitic Transformation in In/Tl Alloys, *J. Mat. Sci.*, 3: 372-379 (1968)
41. M.W. Burkart and T.A. Read, Diffusionless Phase Change in the Indium-Thallium System, *Trans. AIME*, 191(11): 1516-1524 (1953)
42. S. Miura, et al., Pseudo Elastic Behavior and Aging Effect in Thermoelastic In-Tl Martensite, *Mem. Fac. Eng. Kyoto Univ.*, 43(2): 287-303 (1981)
43. A. Nagasawa, Memory Effect in In-Tl Alloy, *J. Phys. Soc. Japan*, 30: 1200 (1971)
44. O. Nittono, and Y. Koyama, Cubic-Tetragonal Transformation and Shape Memory Behavior in Indium-Thallium and Indium-Cadmium Alloys, *Trans. Inst. Met. Japan*, 23(6): 28-32 (1982)
45. A. Ölander, An Electrochemical Investigation of Solid Cadmium-Gold Alloys, *J. Am. Chem. Soc.*, 54: 3819-3833 (1932)
46. F.E. Wang, et al., Crystal Structure and A Unique Martensitic Transformation of TiNi, *J. Appl. Phys.*, 36: 3232-3239 (1965)
47. C.W. Chen, Some Characteristics of the Martensite Transformation, *Journal of Metals*, 1202-1203 (Oct. 1957)
48. C.M. Wayman, On Memory Effects Related to Martensitic Transformations and Observations in Beta Brass and Fe₃Pt, *Scrip. Metall.*, 5: 489-492 (1971)

49. K. Otsuka and K. Shimizu, Memory Effect and Thermoelastic Martensitic Transformation in Cu-Al-Ni Alloy, *Scrip. Metall.*, 4: 469-472 (1970)
50. H. Pops, Stress-Induced Pseudoelasticity in Ternary Cu-Zn Based Beta Prime Phase Alloys, *Met. Trans.*, 1: 251-258 (1970)
51. C.M. Wayman, Deformation Mechanisms and Other Characteristics of SMA: Shape Memory Effects in Alloys, Plenum Press (1975)
52. C.M. Wayman, and K. Shimizu, The Shape Memory Effects in Alloys, *Met. Sci. J.*, 6: 175-183 (1972)
53. L. Schetky, "Shape Memory Alloys", *Scientific American*, 74-82 (Nov. 1974)
54. C.M. Wayman and J. Harrison, The Origin of the Shape Memory Effect, *J. Met.*, 26-28 (Sept. 1989)
55. K. Melton and T. Deurig, Industrial Applications of Shape Memory Alloys, *Met.* 52(8): 318 (1985)
56. R. Banks, Nitinol Heat Engines: Shape Memory Effects in Alloys, Plenum Press (1975)
57. L. Nuldawer and R. Feder, Temperature Responsive Cadmium-Silver-Gold Alloys, U.S Patents 3012882, Dec. 12 (1961)
58. R. Ikegami, et al., Active Vibration Control Using Nitinol and Piezoelectric Ceramics, *J. Intell. Mat. Sys. and Str.*, 1: 189-206 (1990)
59. P.A. Neukomm, et al., Characteristics of Thin-Wire Shape Memory Actuators, *Sens. and Act.*, A21-A23: 247-252 (1990)
60. M. Bergamasco, et al., Shape Memory Alloy Microactuators, *Sens. and Act.*, A21-A23: 253-257 (1990)
61. T. Minemura, et al., Reversible Color Change in Sputter-Deposited Cu-Al-Ni Film, *J. Mat. Sci- Lett.*, 6(11): 1267-1269 (1987)

62. T. Minemura, et al., Shape Memory Effect and Microstructures of Sputter-deposited Cu-Al-Ni Films, *J. Mat. Sci. Lett.*, 4(6): 793-796 (1985)
63. M. Igharo and J.V. Wood, Effect of Rapid Solidification Processing on Shape Memory Characteristics of Equiautomic TiNi: Phase Transformation, *The Institute of Metals*, (1988)
64. J. Perkins, et al., Grain Boundary Structures in Rapidly Solidified Cu-Zn-Al Alloys, *Scrip. Met.*, 15: 771-776 (1981)
65. C.H. Sonu, T.J. O'Keefe, S.V. Rao, and L.R. Koval, Investigation of Shape Memory Properties of Electrodeposited Indium-Thallium Alloys, *Am. Def. Prep. Ass.*, An International Symposium & Exhibition on Active Materials & Adaptive Structures, Alexandria, VA Nov. 4-8 (1991)
66. F.A. Lowenheim, *Electroplating*, McGraw-Hill Book Co. (1978)
67. K.M. Gordobunova and Yu. Polukarov, *Electrodeposition of Metals and Alloys*, Israel Program for Scientific Translation (1969)
68. T.B. Massalski, *Binary Alloy Phase Diagrams*, Am. Soc. Met. Metal Park, OH, vol 2: 1410 (1986)
69. I. Dvorak and E.B. Hawbolt, Transformational Elasticity in a Polycrystalline Cu-Zn-Sn Alloy, *Met. Trans. A*, 6A: 95-99 (1975)
70. J. Perkins, Rapid Solidification Effects in Martensite Cu-Zn-Al Alloys, *Met. Trans. A*, 13A: 1367-1372 (1982)
71. J. Muntasell and J. Tamarit, Influence of Grain Growth on the Martensitic Transformation in Cu-Al-Zn Memory Alloys, *Mat. Res. Bull.*, 24: 445-452 (1989)
72. C. A. Rogers and H. H. Robertshaw, "Shape Memory Alloy Reinforced Composites," *Engineering Science Preprints 25*, ESP25.88027, Society of Engineering Sciences, June 20-22, 1988.

73. D. Barker, "Active Dynamic Response Tuning of Adaptive Composites Utilizing Embedded Nitinol Actuators," M.S. Thesis, Department of Mechanical Engineering, Virginia Polytechnic Institute and State University, 1989.
74. A. Baz and L. Tampe, "Active Control of Buckling of Flexible Beams," *Failure Prevention and Reliability - 1989*, ASME, DE-Vol. 16, pp. 211-218, 1989.
75. C. R. Fuller, C. A. Rogers, and H. H. Robertshaw, "Active Structural Acoustic Control with Smart Structures," SPIE Conference 1170 on Fiber Optic Smart Structures and Skins II, 1989.
76. C. A. Rogers, C. Liang, and J. Jia, "Behavior of Shape Memory Alloy Reinforced Composite Plates, Part 1: Model Formulation and Control Concepts," *Proceedings of the 30th Structures, Structural Dynamics and Materials Conference*, AIAA Paper 89-1389, 1989.
77. C. Liang, J. Jia, and C. A. Rogers, "Behavior of Shape Memory Alloy Reinforced Composite Plates, Part 2: Results," *Proceedings of the 30th Structures, Structural Dynamics and Materials Conference*, AIAA Paper 89-1331, 1989.
78. C. A. Rogers, "Dynamic and Structural Control Utilizing Smart Materials and Structures," *Proceedings of the International Workshop on Intelligent Materials*, The Society of Non-Traditional Technology, pp. 109-121, 1989.
79. C. A. Rogers and D. K. Barker, "Experimental Studies of Active Strain Energy Tuning of Adaptive Composites," *Proceedings of the 31st Structures, Structural Dynamics and Materials Conference*, AIAA-90-1086, 1990.
80. W. R. Saunders, H. H. Robertshaw, and C. A. Rogers, "Experimental Studies of Structural Acoustic Control for a Shape Memory Alloy Composite Beam," *Proceedings of the 31st Structures, Structural Dynamics and Materials Conference*, AIAA-90-1090, 1990.
81. R. Ikegami, D. G. Wilson, J. R. Anderson, and G. Julien, "Active Vibration Control using Nitinol and Piezoelectric Ceramics," *J. of Intelligent Mater. Syst. and Struct.*, 1, pp. 189-205, April 1990.

82. A. Baz, K. Iman, and J. McCoy, "Active Vibration Control of Flexible Beams using Shape Memory Actuators," *J. of Sound and Vibration*, 140(3), pp. 437-456, 1990.
83. B. J. Maclean, G. J. Patterson, and M. S. Misra, "Modeling of a Shape Memory Integrated Actuator for Vibration Control of Large Space Structures," *J. of Intelligent Mater. Syst. and Struct.*, 2, pp. 72-94, 1991.
84. K. Kuribayashi, "A New Actuator of a Joint Mechanism using TINI Alloy Wire," *Int. J. Robotics Research*, 4, pp. 47-58, 1986.
85. D. G. Wilson, J. R. Anderon, R. D. Rempt, and R. Ikegami, "Shape Memory Alloys and Fiber Optics for Flexible Structure Control," *SPIE Fiber Optic Smart Structures and Skins III*, 1370, pp. 286-295, 1990.
86. C. A. Rogers and D. Barker, "Experimental Studies of Active Strain Energy Tuning of Adaptive Composites," *31st AIAA/ASME/ASCE/AHS/ASC Structures, Structural Dynamics and Materials Conference*, AIAA-90-1086, Long Beach, CA, April 2-4, 1990.
87. A. Baz, K. Iman, and J. McCoy, "The Dynamic and Thermal Characteristics of Shape Memory Actuators," *SPIE Fiber Optic Smart Structures and Skins II*, 1170, pp. 271-293, 1989.
88. C. A. Rogers, C. Liang, and D. K. Barker, "Dynamic Control Concepts Using Shape Memory Alloy Reinforced Plates," *Smart Materials, Structures and Mathematical Issues*, C. A. Rogers, Ed., Technomic Publishing Co., 1989.
89. C. Liang, C. A. Rogers, and C. R. Fuller, "Acoustic Transmission/Radiation Analysis of Shape Memory Alloy Reinforced Laminated Plates," *Journal of Sound and Vibration*, 145 (1), pp. 23-41, February 1991.
90. C. Liang, and C. A. Rogers, "Design of Shape Memory Alloy Coils and Their Applications in Vibration Control," *Recent Advances in Active Vibration Control of Sound and Vibration*, edited by C. A. Rogers and C. R. Fuller, April 1991.
91. C. A. Rogers, "Active Vibration of Structural Acoustic Control of Shape Memory Alloy Hybrid Composites: Experimental Results," *Journal of Acoustical Society of America*, pp. 2803-2811, December 1990.

92. Juang, J. N. and Pappa, R. S., "An Eigensystem Realization Algorithm for Modal Parameter Identification and Model Reduction", *Journal of Guidance, Control and Dynamics*, Vol. 8, September - October 1985, PP 620-627.
93. Minh, P., Lucas, G. H., Juang J. N. and Longman R. W., "Linear System Identification via an Asymptotically Stable Observer", *Proceedings of the AIAA Guidance, Navigation and Control Conference*, 1991, PP 1180-1194.
94. Moonen, M., DeMoor, B., Vandenberghe, L. and Vandewalle, J., "On- and Off- Line Identification of Linear State Space Models", *International Journal of Control*, 1989, pp 219-232.
95. Larimore, W. E., "System Identification, Reduced Order Filtering and Modelling via Canonical Variate Analysis", *Proc. of Automatic Control Conf. San Fransisco*, 1983.
96. Söderström, T., and Stoica, P., System Identification, pp 37-42, Prentice-Hall, Inc. 1987.
97. Ljung, L., System Identification: Theory for the User, pp 143-146, Prentice-Hall, Inc. 1987.
98. Moore, B. C., "On the Flexibility offered by State Feedback in Multivariable Systems beyond Closed-Loop Eigenvalue Assignment", *IEEE Transactions on Automatic Control*, Volume AC-21, pp 689-692, 1976.
99. Kailath, Thomas, Linear Systems, Prentice-Hall, Inc. 1980.
100. Chen, Chi-Tsong, Linear System Theory and Design, Holt, Rinehart and Winston. 1984.
101. Prakash, Rajiva, Target Feedback Loop/Loop Transfer Recovery Robust Control System Designs, Dissertation, Department of Electrical Engineering, University of Missouri-Rolla, 1990.
102. Moore, B. C., "On the Flexibility offered by State Feedback in Multivariable Systems beyond Closed-Loop Eigenvalue Assignment", *IEEE Transactions on Automatic Control*, Volume AC-21, pp 689-692, 1976.
103. Kautsky, J., Nichols, N. K., and Van Dooren, P., "Robust Pole Assignment in Linear State Feedback", *International Journal on Control*, Volume 41, pp 1129-1155, 1985.
104. Grace, A., Lamb, A. J., Little, J.N., Thompson, C., "Control Systems Toolbox for use with MATLAB", The Mathworks, Inc., October 1990.
105. Maciejowski, J.M., Multivariable feedback design, Addison-Wesley Publishing Co., 1989.
106. Doyle, J.C. and Stein, G., "Multivariable Feedback Design: Concepts for a Classical/Modern Synthesis", *IEEE Transactions on Automatic Control*, Volume. AC-24, Feb 1981, pp 607-611.
107. Narendra, K., A. Annaswamy, "Stable Adaptive Control," Prentice Hall, Englewood Cliffs, NJ, 1989, pp 21-28,182-232, 318-345.
108. Åström, K., B. Wittenmark, Adaptive Control, Addison-Wesley, Reading, MA, 1989, pp 105-156.
109. Maciejowski, J.M., Multivariable feedback design, Addison-Wesley Publishing Co., 1989.
110. Ridgely, D. and Banda, S., "Introduction to Robust Multivariable Control," AFWAL-TR-85-3102, United States Air Force, February 1986

111. Prakash, Rajiva, Target Feedback Loop/Loop Transfer Recovery Robust Control System Designs, Dissertation, Department of Electrical Engineering, University of Missouri-Rolla, 1990.
112. Narendra, K. S. and Kannan, P., "Identification and Control of Dynamical Systems Using Neural Networks", *IEEE Transactions on Neural Networks*, Mar. 1990, Vol. 1, no. 1, pp 491-513.
113. Chu, R. and Tenorio, M., "Neural Networks for System Identification", *Proceedings of the 1989 American Control Conference*, Vol. 1, 1989, pp 916-920.
114. Stubberud, A., Wabgaonker, H., and Stubberud S., "A Neural Network Based System Identification Technique", *Proceedings of the 30th Conf. on Decision and Control*, 1991, pp 869-871.
115. Mathew, C. Y., "A Neural Network for Computing the Pseudo-inverse of a Matrix and Applications to Kalman Filtering", Technical Report, California Institute of Technology, JPL, Pasadena, Calif. 91109.
116. Bialasiewicz, J. T. and Soloway, D., "Neural Network Modeling of Dynamical Systems", *Proceedings of International Symposium on Intelligent Control*, 1990, pp 500-505.
117. Baz, A., "A Neural Observer for Dynamic Systems", *Journal of sound and vibration* Vol. 1, August 1991, pp 151-160
118. Chow, T. W. S. and Yam, Y. F., "Discrete Time Domain Pole Zero Identification Using Backpropagation Neural Networks", *6th International Conf. on Digital Processing of Signals in Communications*, Sep 1991, pp 215-218.